IN SITU STUDIES OF PROMOTED CATALYTIC SURFACES AND REDOX ACTIVE MINERAL SURFACES

A Dissertation
Submitted to the
Temple University Graduate Board

In Partial Fulfillment
of the Requirements for the Degree
DOCTOR OF PHILOSOPHY

By
Alexander D. Gordon
August, 2011

Committee Members
Daniel R. Strongin, Advisor
Francis C. Spano, Committee Member
Michael J. Zdilla, Committee Member
Martin A.A. Schoonen, External Committee Member

ABSTRACT

In this dissertation the *in situ* technique, attenuated total reflection-Fourier transform infrared spectroscopy, will be utilized to probe reaction chemistry on two sets of surfaces; the first, a silicon-copper alloy surface where copper acts as a catalyst in the synthesis of methylchlorosilanes, and the second, a redox active iron-sulfur surface. Spectroscopic information obtained *in situ* will be combined with kinetic batch reaction results to elucidate details of the reaction mechanism that gives information regarding product formation in real time under real experimental conditions, without the need for modifying the experimental conditions to fit the analysis as is the case in traditional surface science techniques.

ACKNOWLEDGEMENTS

It is nearly impossible to thank all the people that have stood by me throughout my graduate school experience. Without the unwavering support of those around me, I would not have been able to accomplish this thesis work at Temple University. First, I would like to express my thanks to my research advisor, Dr. Daniel Strongin. His invaluable guidance, patience, and scientific insight helped me to improve not only as a chemist, but also as a person and a professional. I would also like to thank Drs. Frank Spano and Mike Zdilla, who always were there to answer questions, no matter how trivial. Finally, I would like to thank my external committee member Dr. Martin Schoonen of SUNY-Stony Brook, who was an invaluable resource for the geological aspects of my work, as well as my career.

I owe a great deal of gratitude to Dr. Schoonen's postdoctoral fellow and laboratory manager, Dr. Alexander Smirnov. Over the final 2-3 years of my research, Dr. Smirnov has been a guiding voice in my development as a scientist as well as a trusted colleague, coauthor and friend.

I also want to thank the Strongin Group members, both past and present. I hope that you learned from me as much as I learned from you not only about research but about life as well. I owe a huge debt of gratitude to ABRC team members from Montana State University, specifically, Drs. John Peters, Timothy Minton, Robert Szilagyi and Chris Fleming. An additional thank you is extended to Dr. Szilagyi and his group for allowing me to participate in synchrotron work at Stanford University. I also owe a great big thank you to Dr. Eric Borguet and his group members past and present for many thoughtful conversations as well as outside activities. I also would like to thank Dr.

Robert Levis and his group members. The Levis Group members were very generous with their time and support and I cannot thank them enough. I am indebted greatly to Dr. Kurt Kistler, Dr. Beth Judge, Erin McCole, Shalaka Dewan and Paul Finn for allowing me to take part in organizing the Chemistry After Dark seminar series. I learned a tremendous amount from each of you whether you know it or not, and I valued my experiences with you guys tremendously.

Thanks also must be given the rest of the Temple University faculty for their support throughout my time here. Additionally, I thank Regina Shapiro, the business office staff, Ed Kaczanowicz and Matt McCormick. I also extend thanks to two individuals who passed away during my time here, George McCurdy and Warren Muir. These two individuals were always there to listen and offer a kind word, no matter what the circumstance.

Additionally, I owe thanks to the following individuals: Matthew Fulmer, Brian Novitsky, Gordon Gronkowski, David Michael Luber, and Riley Didion. Your friendship means more to me than I can ever explain in words. Thanks for being there for me all these years and for the occasional motivational speech.

I will always be greatly indebted to the Mohan and the Novitsky families. The unwavering support I received from both families' has been a godsend in my life and I cannot thank either enough. A big part of my work belongs to each of these families and I cannot express what their love and support has meant to me over the years.

Many thanks are owed to Colleen Mohan. Thank you for being my rock and for being there for me through the good and bad times.

I must finally thank my own family and in particular, my parents, Drs. Laura and Gerald Gordon. I could not have asked for two parents that could have prepared me for life, research, and the pursuit of happiness in any better manner. Your guidance and insight has been invaluable.

To my parents, Gerald and Laura,
for the 28 years of love and support
you have provided.

TABLE OF CONTENTS

APPENDICES

LIST OF FIGURES

LIST OF TABLES

CHAPTER 1

INTRODUCTION

In recent years, *in situ* techniques have become widely used as a tool for monitoring surface chemical reactions as they proceed under real reaction working conditions. In the context of surface facilitated reactions (the focus of this dissertation), such studies typically require analytical techniques that can discriminate between molecules adsorbed on a solid surface from reactant and/or product molecules in the contacting gas or liquid phase. Such a study allows one to shed light on the chemistry occurring on the active working solid surface, a goal of the surface chemist. The in situ methodology is in contrast to ex situ analyses where samples of interest are removed from reaction conditions (i.e., from the contacting gas or liquid phase) prior to their study. While ex situ studies often reveal chemical and structural changes of the surface of interest they, however, preclude the identification of adsorbed species (e.g., reaction intermediates) that only populate the surface in the presence of the contacting gas or liquid phase.

This dissertation describes novel investigations of two surface based reactions: 1) the production of silanes on a copper - silicon surface and 2) the production of ammonia from the reactions of solution phase nitrogen oxides and solvated dinitrogen on iron-sulfur surfaces. The former reaction has direct relevance to the silicone industry and the latter to prebiotic chemistry that has been postulated to occur in submarine hydrothermal vents. While the chemistry associated with each of the surface facilitated reactions is different, there is a common unifying thread running through them: each of the reactions occurs at temperature and / or pressure conditions that has previously hindered their study

with traditional surface sensitive spectroscopic probes. In short, this thesis details novel in situ studies that investigate both of these important heterogeneous reactions at realistic reaction conditions with the intent of elucidating mechanistic details that control the chemistry of each reaction. It is useful now to briefly introduce the importance of the chemistry that will be investigated in this dissertation.

1.1 INTRODUCTION TO THE DIRECT SYNTHESIS OF METHYLCHLOROSILANES

Due to the increasing demand for silicone polymer based materials for use as sealants, adhesives, lubricants, medical applications and insulation, the demand for methylchlorosilane monomers has grown substantially in recent years. However, in 1945, the industry experienced its most rapid growth in large part to the discovery of the direct synthetic route to methylchlorosilane monomer, which made silane and thus, silicone production much more efficient and cost effective [1]. This new route, called the Direct Synthesis (DS), produces methylchlorosilane monomers from the reaction of methyl chloride (CH_3Cl) with elemental silicon in the presence of a copper based catalyst at 300 ^{o}C.

1.1.1 REACTION CONDITIONS IN THE MODERN DIRECT SYNTHESIS

In addition to the copper catalytic component, small (parts per million, ppm) amounts of zinc (Zn), tin (Sn), and phosphorous (P) additives, termed promoters, are also commonly added to increase (i.e., promote) both the rate of monomer production as well as the selectivity for certain silane products. The exact concentration of each component is in many cases considered proprietary information and is not readily available in the literature. Promoter mixtures are added when it is desirable, for instance, to produce

dimethyldichlorosilane (DMDCS) at high rates with high selectivity. Without these promoters, the DS is relatively unselective for the DMDCS product and produces a relatively low yield of the product. The DS reaction can be represented by the following reaction:

$$CH_3Cl_{(g)} + Si_{(s)} \xrightarrow{\text{Cu catalyst, Promoters (300° C)}} Me_xSiH_yCl_z$$

where $x + y + z = 4$

Due to the importance of the DS, attempts at studying the mechanistic details that contribute to product formation have been studied for decades but there is still little agreement in the literature as to the mechanism of promoter action [2-7]. The lack of understanding of the mechanistic details concerning promoter action is likely due to the extremely low concentrations that exist in the reaction mixture (known as the contact mass).

Generally speaking, conditions that the DS requires (i.e. 300 ^{o}C, 1 atm of CH_3Cl) make the implementation of in situ spectroscopic techniques somewhat difficult. ATR-FTIR, however, provides a robust solution for in situ sampling, since there is no sample preparation required for analysis and diamond based single bounce units can reliably stand up to the reaction conditions required by the DS. Though it is theoretically possible to implement other infrared sampling techniques such as transmission FTIR, ATR-FTIR will be relatively insensitive to signals originating from gas phase species, making it more attractive for observing surface adsorbates in situ.

1.1.2 PRIOR DIRECT SYNTHESIS INVESTIGATIONS

Previous studies have largely investigated promoter action in the DS in terms of copper-silicon interaction (i.e. eta phase formation) [8]. In general, little effort has been made in addressing the effect of the promoters on the dissociative chemisorption of CH_3Cl and the resulting generation of methyl and chlorine surface groups. Furthermore, these prior studies, largely consisting of ex situ methodology, have investigated the composition of the DS contact mass after reaction, or under reaction conditions that are unrealistic (i.e. pressure gap). Hence, chemical information that is concerned with the composition of the active contact mass surface of the working DS contact mass is largely unavailable. The results presented in this thesis will help alleviate this deficiency in an understanding of the working catalytic surface.

1.2 INTRODUCTION TO ORIGIN OF LIFE INVESTIGATIONS

Despite years of thought dedicated to understanding the Origin of Life, there has been little consensus reached scientifically on its origins. In 1953, the now famous Miller-Urey experiment sparked the development of Origin of Life science, in which scientific experiments could now be conducted to test various theories. This experiment simulated early Earth's atmosphere by mixing various partial pressures of CO, H_2, CH_4, H_2O and NH_3 in a spark discharge tube that was heated and circulated [9]. Analysis of the subsequent mixture yielded various amino acids, glycine being the most abundant. Perhaps the most important aspect of this study was that this single experiment jump started an entire field of scientific study.

Thirty years after this famous experiment the now thriving Origin of Life community is divided into two main groups, generically referred to the "RNA World"

group and the "Metabolism First" group (or "Iron-Sulfur World") group. The "RNA World" group refers to those that believe that the ability of cells to reproduce came first and those that believe that cellular metabolism evolved first are known as the "Metabolism First" group. These two groups differ only on whether a cell's ability to reproduce itself evolved first, or whether the cell's machinery (i.e. enzymes) evolved first. At this point, neither group has offered definitive evidence to disprove the others' theory.

Among the first supporters of the "Metabolism First" hypothesis was a patent attorney named Gunther Wächtershäuser, who proposed his "Iron-Sulfur World" theory in which the raw materials needed for life (i.e. amino acids) evolved on iron-sulfide surfaces over millions of years [10-13]. Wächtershäuser's arguments were based largely on the premise that the iron-sulfur clusters found in active sites within enzymes (i.e. nitrogenase) evolved via the modification of iron-sulfur surfaces in the prebiotic environment. Wächtershäuser specifically focused much of his attention on the reduction of dinitrogen: the reasoning being that the breaking of the strong N-N triple bond would likely require a catalyst to lower the activation barrier associated with its reduction. Iron-sulfur surfaces, which have been postulated to exist on the Hadean Earth, would seem like a reasonable candidate for such a catalytic surface considering that the present day enzyme nitrogenase, which contains the Fe-S cubane structure, efficiently converts dinitrogen to ammonium in specific biochemical systems. Additional support for the "Iron-sulfur World" theory exists in the numerous iron sulfide based minerals (i.e. pyrite, pyrrhotite, greigite, troilite) found in the Earths' crust today.

1.2.1 CONDITIONS ON THE HADEAN EARTH

Although a range of conditions have been proposed to have been present on the Hadean Earth, it is generally thought that the atmosphere likely consisted of very mildly reducing chemical constituents, such as N_2, H_2O vapor, H_2S and CO_2. Although other models have also considered the likelihood that early Earth may have also had a slightly oxidizing atmosphere [14-17] and most agree that the Hadean ocean was much warmer than the ocean of today, likely due to higher heat fluxes experienced by the earth at that time [18]. Modeling of the pH conditions of the Hadean ocean have largely shown that the pH was probably mildly acidic, likely due to the increased partial pressure of CO_2 present in the Hadean atmosphere relative to today's atmosphere [19]. It is important to note that it is not currently known if land was present during the Hadean. The present day analogue of conditions thought to exist on earth during the Hadean Eon are the hydrothermal vents found on the oceanic floor. Studies of different vents show these vents vary widely in pH (3-10) and temperature (~100 ^{o}C to 400 ^{o}C). Some photographic examples of these vents are shown in Figure 1.1 [20].

1.2.2 AMMONIA FORMATION IN SIMULATED HADEAN EARTH ENVIRONMENTS

The myriad of reactions that were likely needed to produce life giving molecules (i.e. amino acids) were almost certainly occurring simultaneously. The reduction of dinitrogen to ammonia was likely one of the more energetically costly reactions considering that for dinitrogen reduction to proceed, a series of activation barriers must be overcome: the N-N triple bond, the greatest being 225 kcal / mol (N_2 bond) followed by 100 kcal / mol, and 39 kcal / mol upon subsequent step-wise protonation reactions [21,

22]. Prior work by Schoonen and Xu concluded that FeS facilitated the reduction of solvated nitrogen to ammonia in solution, but it occurred to a limited extent and it was unlikely that the ammonia required for amino acid formation in a prebiotic environment during the Hadean [23] formed solely by this reaction pathway. Schoonen and Xu went on to state that ammonia emitted from subaerial volcanic structures [25, 26], ammonia produced via reduction of dinitrogen by metallic iron and wüstite [27] and ammonia produced by reduction of nitrite by dissolved ferrous iron [24] are all possible sources of ammonia during the Hadean period. It has been suggested that rather than dinitrogen being directly converted to ammonia, it might be that on early Earth aqueous nitrite and nitrate may have been intermediates in the reduction of dinitrogen to ammonia. Models by various groups have shown that terrestrial lightning, coronal discharge, large body (bolide) impacts, and electromagnetic radiation may have played a role in nitric oxide (NO) formation from the following reaction [28, 29]:

$$2CO_2 + N_2 \rightarrow 2NO + 2CO \qquad (1.1)$$

Nitric oxide reacts with atmospheric water to form nitric and nitrous acids (by means of HNO) which eventually precipitated into the oceans [30]. Once in the aqueous environment, the reduction of nitrite and nitrate is proposed to have occurred by reduction by Fe^{2+} [24].

1.2.3 ROLE OF IRON-SULFUR SURFACES IN AMMONIA FORMATION

The FeS_x surface is an integral part of the mineral based origin of life theory [31]. The evolution of amino acids directly from activated prebiotic organics on these surfaces provides a direct link of aqueous geochemistry with biochemistry. Although prior work has hypothesized the catalytic nature of the FeS_x surface toward dinitrogen reduction,

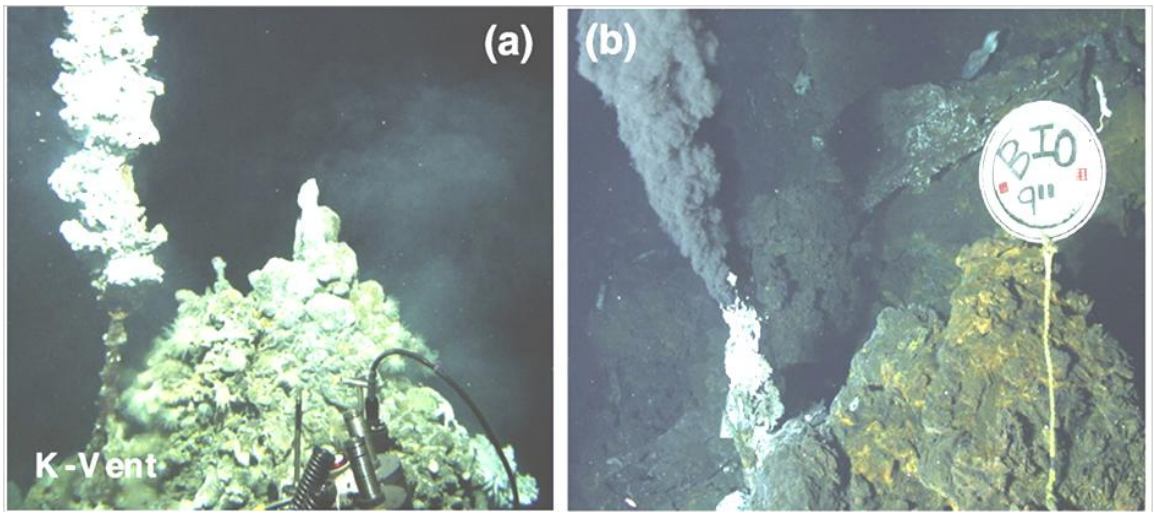

Figure 1.1: Two examples of active seafloor chimneys (K-vent and Bio9") [20]

additional work has suggested that the surface is in fact also redox active toward ammonia formation from nitrite and nitrate [23, 32]. In either case, it is well established in the literature that FeS_x provides an electron rich surface that can act as an electron donor for reactions such as the reduction of nitrite [24].

1.2.4 PRIOR INVESTIGATION OF AMMONIA FORMATION ON IRON-SULFUR SURFACES

This purpose of this investigation is to understand ammonia formation on iron-sulfur surfaces. Prior research has been conducted that examined the role of iron-sulfur minerals in nitrite and nitrate reduction [27, 32, 33]. Of these investigations, the Brandes and Summers studies provided the first batch reaction data associated with ammonia formation from nitrite and nitrate reduction, though little mechanistic details were elucidated in either study [27, 33]. Alternatively, the Singireddy study was able to probe the kinetics associated with nitrite and nitrate reduction in greater detail as well as observe the relevant surface adsorbate chemistry associated with the reduction of nitrite on pyrite.

The investigations presented in this dissertation serve to expand the body of knowledge available in the literature on nitrite and nitrate reduction. Specifically, the reduction of nitrite and nitrate in alkaline conditions will be investigated, as will the effect of the surface modification of pyrite and the effect of these modifications on nitrite and nitrate reduction reaction. ATR-FTIR and geochemical batch reactions will probe both surface intermediates and ammonia formation kinetics, respectively, which will yield mechanistic details associated with reactions examined in both experiments.

1.3 OVERVIEW OF IN SITU ATR-FTIR SAMPLING

In situ sampling indicates that analysis is accomplished in real time under real reaction conditions. In recent years, in situ attenuated total reflection Fourier transform infrared (ATR-FTIR) spectroscopy has become a popular method for monitoring reactions relevant to the polymer, pharmaceutical, fine chemical, and coatings industries in addition to environmentally relevant chemistry that occurs on mineral surfaces in aqueous systems [34-37]. The infrared technique is currently an attractive alternative to the more widely used transmission geometry which has been used for years in reaction monitoring. However, heterogeneous reactions that consist of a solid surface in contact with a strongly adsorbing liquid phase (i.e. water), for example, make implementation of the transmission geometry extremely difficult when one is interested in the structure and composition of the adsorbed layer on the solid [36]. This issue develops because the absorbance by the liquid phase, for example, is orders of magnitude stronger than the surface adsorbed layer, making the isolation and identification of the latter absorbances from the strong liquid absorbances exceedingly difficult.

To circumvent the problems associated with the transmission geometry, ATR-FTIR is used in the work detailed in this thesis to understand the adsorbed monolayer at the hidden interface between a solid substrate and either a high pressure gaseous or liquid phase. How ATR-FTIR is able to better probe this hidden interface is detailed in the next chapter. The versatility of ATR-FTIR is also exemplified by the range of pressures in which it can be utilized. Because ATR-FTIR spectroscopy avoids sample preparation necessary with other analytical methods, reactions can be monitored as they occur (i.e. in situ), which is advantageous when monitoring reactions at temperatures as high as 300 ^{o}C

and 3000 psi. Modern reaction cell designs have allowed for more versatility of sampling using a variety of ATR element materials, o-rings, and top plate designs, all of which can be easily tailored to suit the experimental requirements which allows for unparalleled experimental versatility.

Monitoring solid surfaces interacting with gas phase or aqueous based adsorbates in situ is of particular interest to the surface science community due to the so-called pressure gap that exists within the analysis techniques widely utilized by the surface science community. The pressure gap refers to the gap in pressure between real reaction conditions and the conditions required by the instrument (10^{-6} to 10^{-10} torr). The development of in situ spectroscopic (i.e. ATR-FTIR) techniques bridges the pressure gap that exists. ATR-FTIR can also be used to identify surface intermediates of surface based reactions in real time. Mechanistic details associated with the reactive surface can be elucidated from these intermediates and by employing various surface sensitive techniques such as x-ray photoelectron spectroscopy to provide complimentary information on the surface composition (i.e. oxidation state).

1.4 SUMMARY OF WORK TO BE PRESENTED

This dissertation is focused on the understanding of the surface chemistry associated with the copper-silicon contact masses and iron sulfide chemistry at high temperatures. The thesis is organized in the following way. Chapter 3 will present Direct Synthesis work that was published in the *Journal of Catalysis* in 2009 (Gordon et al. Effects of Individual Promoters on the Direct Synthesis of Methylchlorosilanes, *Journal of Catalysis* (2009) 266, 291-298) [38]. This work describes the reactions monitored spectroscopically using in situ ATR-FTIR spectroscopic techniques to understand the role

of parts-per-million amounts of promoters added to a catalytic system which is used to produce organohalosilanes, a precursor to silicones. In particular, the effect of these promoters will be described in terms of rates of product formation and the selectivity of products. Chapters 5 and 6 describe chemistry associated with reactions on Iron Sulfur mineral surfaces that were thought to be integral for jumpstarting life on Earth. Specifically, ammonia formation from nitrite and nitrate reduction reactions on iron sulfur surfaces will be monitored using ATR-FTIR spectroscopy which will yield information about the surface bound intermediates of these reactions, thus establishing mechanistic details of these surface mediated reactions. Each chapter will now be described in greater detail.

Chapter 4 will present work published in a second publication related to the Direct Reaction in *Catalysis Letters* in 2009 (Gordon et al., Effects of Multiple Promotion of the Direct Synthesis Contact Mass with P, Zn, and Sn on the Synthesis of Methylchlorosilanes, *Catalysis Letters* (2009) 133, 14-22) [39]. This work builds from Chapter 3 using a similar methodology to understand the role of parts-per-million amounts of materials (termed promoters) added to a catalytic system two-at-a-time (double promoters) or in three-at-a-time (triply promoted). In particular, the synergistic effects of these promoters will be described in terms of rates of product formation, the selectivity of products and some general trends observed on the surface bound intermediates will be presented.

Chapter 5 of this dissertation will be composed of reactions using 5 mM nitrite and nitrate in the presence of a redox active mineral surface, freshly precipitated nano-iron sulfide (FeS) mineral phase in alkaline conditions. The production of ammonia from

nitrite and nitrate as a function of temperature (22 ^{o}C, 70 ^{o}C and 120 ^{o}C) will be explored as will the various surface intermediates observed on the FeS surface as the reaction proceeds. This work demonstrates the functional utility of FeS as a reducing system using nitrite and nitrate and will utilize in situ ATR-FTIR to demonstrate observable surface intermediates as a function of temperature. The results from the ATR-FTIR experiments will be correlated to ammonia production kinetics obtained from geochemical batch reaction data in order to elucidate the surface based mechanism of ammonia formation on FeS.

Chapter 6 investigates the reactivity of pyrite toward nitrite and nitrate reduction and also demonstrates the effect of tetrathiomolybdate treatment of acid washed pyrite surfaces on the reduction of the nitrogen oxides. Results indicate that the rate of ammonia formation is enhanced by the tetrathiomolybdate treatment and that different mechanism(s) are responsible for the enhanced rate of ammonia formation than those observed on acid washed pyrite in prior investigations [32]. Within this chapter, in situ ATR-FTIR results and batch reactor measurements will be shown demonstrating the correlation of surface intermediates with ammonia formation. Additional ex situ techniques will be utilized to track the concentration and oxidation state of the surface Mo as a function of reaction time and temperature. The results will be interpreted in view of prior work on clean acid washed pyrite surfaces, which will demonstrate an enhancement of the rate of ammonia formation with the presence of tetrathiomolybdate sorbed acid washed pyrite.

Additional results from ammonia synthesis experiments will be presented in Appendix A.1. These experiments were conducted as part of a follow-up study to

previous batch kinetic studies conducted by Schoonen and Xu [23] in which FeS is added to pH 6.5 water (10 mM in sulfide) and pressurized with dinitrogen in order to simulate ammonia synthesis that was thought to occur in hydrothermal vent-like conditions.

References

[1] Rochow, E.G., *Journal of the American Chemical Society*, 67 (1945) 963-965.

[2] Lewis, K.M., Kanner, B., *Catalyzed Direct Reactions of Silicon*, El Sevier, Amsterdam, 1993.

[3] Floquet, N., Yilmaz, S., Falconer, J.L., *Journal of Catalysis*, 148 (1994) 348-368.

[4] Ehrich, H., Born, D., Richter, K., Richter-Mendau, J., Lieske, H., *Applied Organometallic Chemistry*, 11 (1997) 237-247.

[5] Ehrich, H., Born, D., Richter-Mendau, J., Lieske, H., *Applied Organometallic Chemistry*, 12 (1998) 257-264.

[6] Lieske, H., Fichtner, H., Grohmann, I., Selenina, M., Walkow, W., Zimmermann, R., Characterization of Rochow Contact Masses by Catalytic Results, XRD, Chemisorption and XPS, in: *Silicon for the Chemical Industry, [Int. Conf.]*, 1992

[7] Lieske, H., Kretzschmar, U., Zimmermann, R., Action of promoters in Rochow contact masses, *Silicon for the Chemical Industry, [Int. Conf.]*, 1994

[8] Lewis, L.N., Ward, W.J., *Industrial & Engineering Chemistry Research*, 41 (2002) 397-402.

[9] Miller, S.L., *Science*, 117 (1953) 528-529.

[10] Wächtershäuser, G., *Progress in Biophysics and Molecular Biology*, 58 (1992) 85-201.

[11] Wächtershäuser, G., *Systematic and Applied Microbiology*, 52 (1988) 452-484.

[12] Wächtershäuser, G., *Systematic and Applied Microbiology*, 10 (1988) 207-210.

[13] Wächtershäuser, G., *Proceedings of the National Academy of Sciences* USA, 87 (1990) 200-204.

[14] Kasting, J.F., *Precambrian Research*, 34 (1987) 205-229.

[15] Walker, J.C.G., Brimblecombe, P., *Precambrian Research*, 28 (1985) 205-222.

[16] Mattioli, G.S., Wood, B.J., *Nature*, 322 (1986) 626-628.

[17] Gregor, C.B., Garrels, R.M., McKenzie, F.T., Maynard, J.B., *Chemical Cycles in the Evolution of the Earth*, Wiley, New York, 1988.

[18] Russell, M.J., Hall, A.J., Cairns-Smith, A.G., Braterman, P.S., *Nature*, 336 (1988) 117.

[19] Grotzinger, J.P., Kasting, J.F., *Catalysis Letters*, 101 (1993) 235-243.

[20] Rouxel, O., Shanks, W.C., Bach, W., Edwards, K.J., *Chemical Geology*, 252 (2008) 214-227.

[21] Howard, J.B., Rees, D.C., *Chemical Reviews*, 96 (1996) 2965-2982.

[22] Cottrell, T.L., *The Strengths of Chemical Bonds*, Butterworths, London, 1958.

[23] Schoonen, M.A.A., Xu, Y., *Astrobiology*, 1 (2001) 133-140.

[24] Summers, D.P., Chang, S., *Nature*, 365 (1993) 630-632.

[25] Giggenbach, W.F., *Geochimica Cosmochimica Acta*, 44 (1980) 2021-2032.

[26] Giggenbach, W.F., The Origin and Evolution of Fluids in Magmatic-Hydrothermal Systems, in: Barnes, H.L. (Ed.) *Geochemistry of Hydrothermal Ore Deposits*, John Wiley & Sons, Inc., New York, 1997, pp. 737-795.

[27] Brandes, J.A., Boctor, N.Z., Cody, G.D., Cooper, B.A., Hazen, R.M., Yoder, H.S., Jr., *Nature*, 395 (1998) 365-367.

[28] Stribling, R., Miller, S.L., *Origins of Life and Evolution of the Biosphere*, 17 (1987) 261-273.

[29] Schopf, J.W. ed., *Earth's Earliest Biosphere*, Princeton University Press, 1983.

[30] Mancinelli, R.L., McKay, C.P., *Origins of Life and Evolution of the Biosphere*, 18 (1988) 311-325.

[31] Wächtershäuser, G., *Origins of Life and the Evolution of the Biosphere*, 20 (1990) 173-176.

[32] Singireddy, S., Gordon, A.D., Smirnov, A., Vance, M.A., Szilagyi, R.K., Schoonen, M.A., Strongin, D.R., *Astrobiology*, (Submitted).

[33] Summers, D., *Origins of Life and Evolution of the Biosphere*, 35 (2005) 299-312.

[34] Leventis, H.C., King, S.P., Sudlow, A., Hill, M.S., Molloy, K.C., Haque, S.A., *Nano Letters*, 10 1253-1258.

[35] Kip, B.J., Berghmans, T., Palmen, P., van der Pol, A., Huys, M., Hartwig, H., Scheepers, M., Wienke, D., *Vibrational Spectroscopy*, 24 (2000) 75-92.

[36] Févotte, G., *International Journal of Pharmaceutics*, 241 (2002) 263-278.

[37] Ingo, A., Steinhoff, B., Lellinger, D., *Measurement Science and Technology*, 21 (2010) 062001.

[38] Gordon, A.D., Hinch, B.J., Strongin, D.R., *Journal of Catalysis*, 266 (2009) 291-298.

[39] Gordon, A.D., Hinch, B.J., Strongin, D.R., *Catalysis Letters*, 133 (2009) 14-22.

CHAPTER 2

EXPERIMENTAL METHODOLOGY

2.1 OVERVIEW

In general, surface chemistry plays a central role in reactions occurring between two phases. Two such reactions in which surface chemistry is extremely important are heterogeneous catalysis of methyl chloride and silicon to produce silanes and the iron-sulfur mineral based stoichiometric reaction of nitrite / nitrate to produce ammonia which are solid-gas and solid-aqueous phase interactions, respectively. Probing these solid-gas interactions and solid-aqueous interactions have become routine thanks to the advent of techniques such as attenuated total reflection-Fourier transform infrared (ATR-FTIR) spectroscopy. The versatility of this technique is easily understood by the lack of sample preparation steps involved with analysis of real systems. ATR-FTIR is especially useful in the analysis of reactions that require elevated temperatures and pressures. Additionally, ATR-FTIR can easily couple directly to other traditional analytical techniques, which requires little to no system modifications.

This chapter will be divided into two sections. The first section will describe sample preparation of copper-silicon contact masses and iron-sulfur mineral phase. The second section will describe the analytical techniques utilized in the investigations presented in this dissertation. ATR-FTIR theory and application will be given a more thorough treatment due to its common usage in the investigations presented in this dissertation.

2.2 SAMPLE PREPARATION PROCEDURES

2.2.1 PROMOTED COPPER-SILICON CONTACT MASS PREPARATION

Eight separate samples were prepared for the experiments presented in chapters three and four which are listed (in weight percent) in Table 2.1. Each of these samples is referred to as a "contact mass." Eight different contact masses were generated in 80 to 100 gram quantities, and were stored in amber bottles in a dessicator. No extra precautions were taken to keep oxygen out of the sample.

2.2.2 NANO-FeS_m PREPARATION

Nanometer-sized iron sulfide (FeS) was prepared by aqueous reaction of ferrous iron (Fe^{2+}) with sulfide (S^{2-}) [1, 2]. In brief, 1 M solutions of $FeSO_4$ and $Na_2S.9H_2O$ (ACS reagent grade, used without further purification), was prepared at room temperature with freshly drawn, Ar-sparged, O_2-free deionized water (18.2 MΩ) inside an anaerobic glovebox (95% N_2 / 5% H_2). The Fe^{2+} containing solution was then injected into the sulfide solution which triggered a rapid FeS precipitation. The resulting black precipitate was centrifuged down, supernatant discarded, and replaced with 1 mM $Na_2S.9H_2O$ solution. This "washing" process was repeated three times and was aimed at removing leftover SO_4^{2-}, Na^+ and unreacted Fe^{2+}. The particle loading was determined using a Pyrex® Guy-Lussac bottle and confirmed by desiccating an aliquot of known volume / weight of the slurry under anaerobic conditions. The FeS slurry was stored in the glovebox with constant O_2 monitoring (Coy Laboratory Products) and used as necessary in batch experiments.

For the ATR-FTIR experiments, FeS was freshly synthesized prior to every experiment using the aforementioned procedure. Appropriate volumes of the FeS slurry

Table 2.1: Contact mass compositions used in direct synthesis experiments

Mixture	**Zn**	**P**	**Sn**	**Cu**
Zn-P promoted	0.060%	0.020%	-	10.000%
unpromoted	-	-	-	10.000%
P promoted	-	0.020%	-	10.000%
Sn-P promoted	-	0.020%	0.004%	10.000%
Sn-Zn promoted	0.060%	-	0.004%	10.000%
Zn promoted	0.060%	-	-	10.000%
Sn promoted	-	-	0.004%	10.000%
Sn-Zn-P promoted	0.060%	0.020%	0.004%	10.000%

*all data listed in wt. %

was then transferred to ~4 mL of 5 mM nitrite or nitrate solution, yielding the same FeS loadings and nitrite / nitrate concentrations as the batch experiments.

Stock nitrite and nitrate solutions were prepared by dissolving reagent-grade $NaNO_2$ and KNO_3 in Ar-purged, O_2-free DI water (18.2 MΩ). Deionized (DI) water (18.0MΩ) used for making solutions was obtained from a nanopure water treatment system and sparged with high purity argon gas for 2 hours to remove any dissolved gases. All samples were prepared under anaerobic conditions in a glove box in an atmosphere of 95% argon / 5% H_2. The glove bag was also equipped with an O_2 sensor. During the sample preparation the oxygen level in the glove box was maintained at 0.00 ppm. Nitrite and nitrate solutions were prepared from reagent grade potassium nitrite and potassium nitrate taken from a stock solution. Each was sparged with argon > 1 hour prior to addition to the FeS.

2.2.3 Mo-S-PYRITE PREPARATION

Natural pyrite from Huanzala, Peru (Ward's Natural Science) was optically examined for impurities, ground in an agate ball mill to a size fraction below 60 µm and acid-washed in dilute O_2-free HCl solution. After drying, the samples were stored in a humidity controlled glovebox with N_2 / H_2 atmosphere. The surface area, determined by N_2-BET was 0.613 $m^2.g^{-1}$. For detailed procedure, consult reference [3]. Mo-S-pyrite was produced by adapting the procedure of Helz and coworkers (2003) [4]. In brief, dry, acid-washed pyrite was exposed repeatedly to a 100 µM solution of diammonium tetrathiomolybdate ($(NH_4)_2MoS_4$), acidified to pH 4 with dilute HCl until the surface reached saturation with respect to tetrathiomolybdate. The sorption was rapid and marked by the disappearance of characteristic red color. The saturation point was first determined

visually when no further color change was observed, and subsequently confirmed with UV-Vis spectroscopy of pre- and post- sorption solution. After the sorption, the tetrathiomolybdate exposed pyrite was washed multiple times with O_2-free deionized water to remove residual ammonium from the solution. Every 3-5 washing cycles, the ammonium content of the effluent was checked with UV-Vis spectroscopy (HACH Salicylate Method, #10023) until stable readings of less than 4 μM were achieved. After drying, Mo-S-pyrite was used in experiments without further modification. The presence of Mo was determined from the presence of Mo $K\alpha_1$ peak in the XRF spectrum. N_2-BET determined surface area of Mo-S-pyrite was 0.508 $m^2.g^{-1}$ (17.13% reduction in specific surface area, due to particle removal during the washing process)

2.3 EXPERIMENTAL SETUP

2.3.1 DIRECT SYNTHESIS EXPERIMENTAL SETUP

In order to deposit the contact mass on the ATR lens and reactor, 3-4 grams of the contact mass was added to hexane (~5 mL) and the resulting slurry was placed on the ATR lens. The ATR "dome" was then placed over the top and fastened against a graphite gasket (see Figure 2.1). The contact mass slurry was also added to a larger reactor (see Figure 2.2) and held in by glass wool. The placement of the cell and reactor within the experimental setup is shown in Figure 2.3. Ultra high purity (UHP) argon was flowed through the reactor setup for 2-3 hours to dry the hexane, after which the reactor was removed, the mass recorded, and placed back into the setup. Finally, the reactor was wrapped in a flexible heating coil (Omega Engineering) and covered in aluminum foil (see Figure 2.2). The UHP argon flow was resumed until the following morning. The following morning the reactor and ATR cell were heated in tandem to 300 ^oC and the

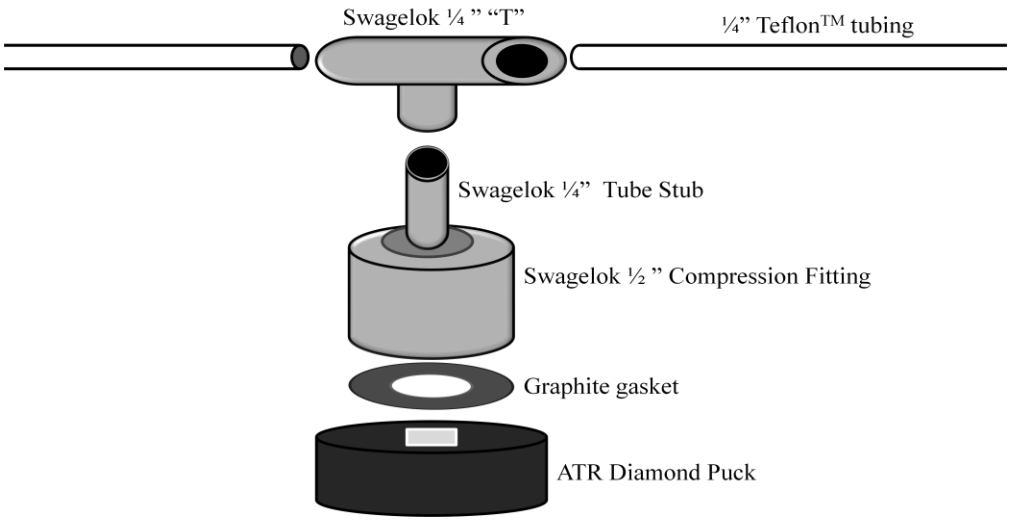

Figure 2.1: Schematic of the ATR-FTIR flow cell utilized in Direct Synthesis studies.

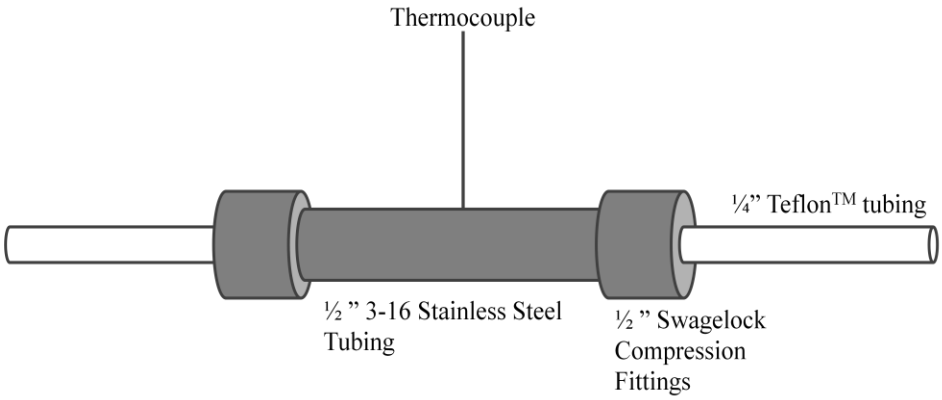

Figure 2.2: Schematic of the lab scale reactor cell utilized in Direct Synthesis investigations.

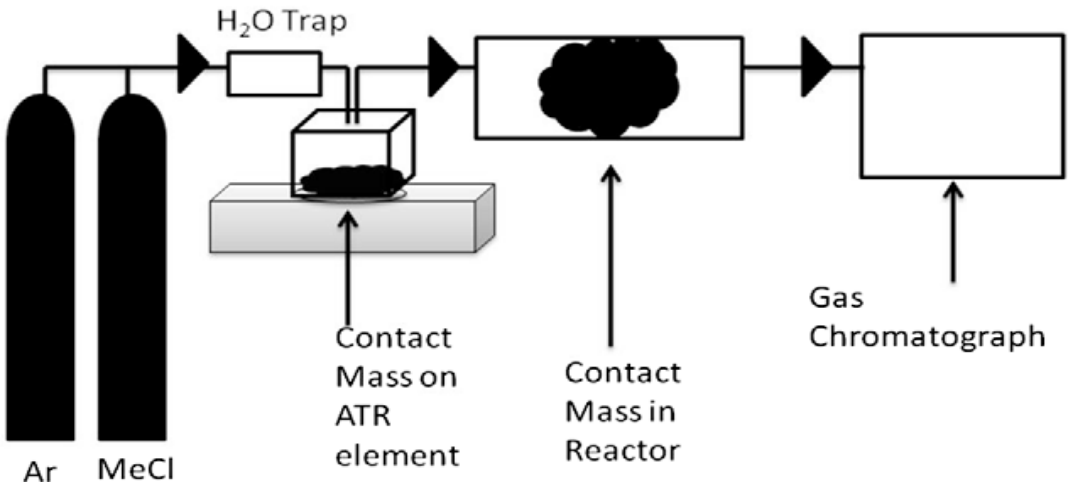

Figure 2.3: Schematic of in situ ATR-FTIR cell coupled with lab scale reactor setup.

ATR-FTIR and GC analyses commenced under argon until the $SiCl_4$ was no longer observed.

2.3.2 AMMONIA FORMATION ON NANO-FeS_m AND Mo-S-PYRITE

EXPERIMENTAL SETUP

For the ATR-FTIR experiments, either Mo-S-pyrite or nano-FeS_m was loaded within a glove bag or glove box environment equipped with an O_2 monitor in which an atmosphere below 0.1 ppm O_2 was maintained. The Mo-S-pyrite, nano-FeS_m / nitrite or nitrate slurry was generated and injected into the multibounce ATR cell through ¼" Tygon® tubing, or in the case of the single bounce unit, added directly onto the diamond puck immediately prior to the start of the experimental run. In both cases, the ATR reactor is sealed while rigorously maintaining oxygen free conditions within the glove box environment.

2.4 IN SITU ATTENUATED TOTAL REFLECTION-FOURIER TRANSFORM INFRARED SPECTRSCOPY

Much of the analytical methodology employed in prior on nitrite and nitrate reduction investigations in the literature centers around the use of techniques such as UV-VIS spectroscopy, fluorescence spectroscopy and ion chromatography to attain information on ammonia formation [5-10]. While these techniques are particularly useful for quantifying the amount of ammonia produced for an experimental system, there is little detail gained as to the relevant surface intermediates that are present during the experiment.

In recent years, ATR-FTIR has been a useful technique to study the reactions that are concentrated on or near the surface of minerals in aqueous media. Although the

method is not considered surface sensitive within the context of the surface science community, the geometry of the technique does concentrate the relevant chemistry close (< 4 um) to the analysis surface. This geometry eliminates saturating absorbances by water related vibrations which can drown out weaker vibrations of surface adsorbates, a problem that exists in traditional transmission infrared spectroscopy.

2.4.1 DEPTH OF PENETRATION EQUATION

ATR-FTIR is a popular choice for the analysis of aqueous systems over the traditional transmission FTIR geometry. The rationale lies in the relative "effective" path lengths of the transmission and ATR-FTIR techniques. In the former, the path length is set by the cell and is typically a fixed value. In the ATR-FTIR technique, the effective path length, or depth of penetration, is defined as the distance required for the electric field amplitude to fall to e^{-1} of its value at the surface. The depth of penetration is described by equation 2.1 [11]:

$$d_p = \frac{\lambda}{2\pi\left(\sqrt{\sin^2\theta - \left(\frac{n_2}{n_1}\right)^2}\right)} \qquad (2.1)$$

where:

- d_p penetration depth
- λ wavelength
- n_1 ATR element refractive index
- n_2 sample refractive index
- θ angle of light propagation relative to the surface normal

As a qualitative comparison, typical small path length transmission cells are ~5-10 microns in path length, while ATR-FTIR depth of penetration into the sample is usually on the order of nanometers.

2.4.2 ATR PHENOMENON: CRITICAL ANGLE

In order for light propagating through a medium of refractive index n_1 and approaching a sample of refractive index n_2 at angle θ (angle with respect to surface normal) to undergo attenuated total reflection, certain conditions must be satisfied. Perhaps most important is the angle of incidence of the propagating light with respect to the surface normal, θ, which must be greater than the critical angle, θ_c , of the system for attenuated total reflection to occur. An illustration of attenuated total reflection of light within an ATR crystal of refractive index n_1 in contact with a sample with refractive index n_2 is shown in Figure 2.4 for $\theta > \theta_c$ and $\theta < \theta_c$.

2.4.3 IN SITU ATR FLOW CELL UTILIZED IN DIRECT SYNTHESIS INVESTIGATIONS

Experiments conducted in chapters three and four utilized the same ATR-FTIR setup, the Supercritical Golden Gate™ (Specac), which was capable of being heated to 300 ^{o}C. The ATR dome was constructed from 3-16 stainless steel Swagelok components; graphite sheeting was cut into circles for use as gasket material which was required to form a pressure tight seal between the diamond puck and dome. Teflon tubing connected the source gas to the ATR cell and the reactor cell to the sampling valve. The contact mass would ordinarily be placed on top of the ATR diamond puck and the whole apparatus would be sealed by a screw mechanism from above (not shown) which compresses the graphite, forming an airtight seal.

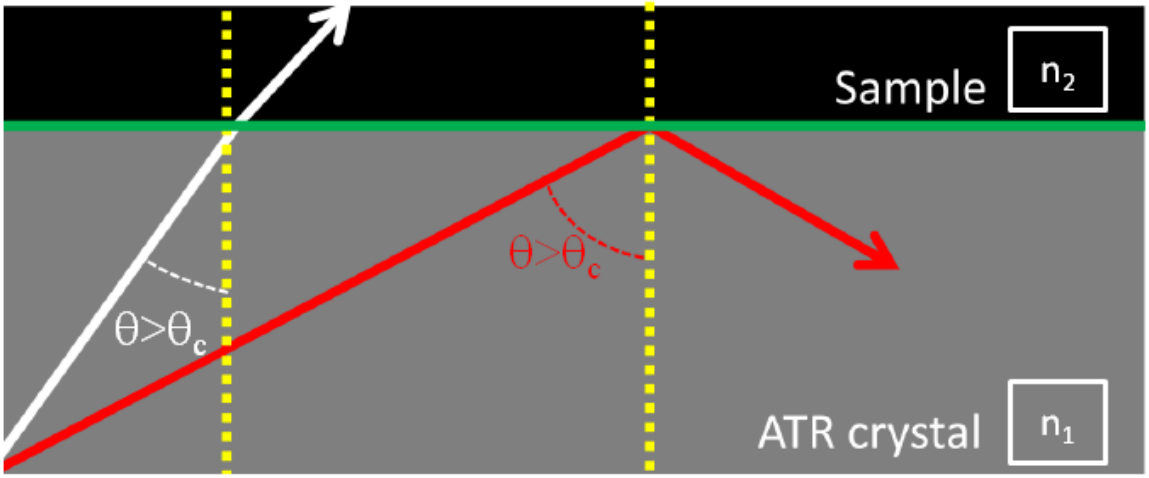

Where: $$\boldsymbol{\theta_c = \sin^{-1}\left(\frac{n_2}{n_1}\right)}$$

Figure 2.4: Illustration of the physical phenomenon of attenuated total reflection of infrared light within an ATR crystal of refractive index n_1 in contact with a sample with refractive index n_2. The relationship between the angle of light propagation (θ) and the critical angle (θ_c) is demonstrated. The white arrow indicates transmission and refraction, and the red arrow indicates attenuated total reflection. The colors in this schematic are for illustrative purposes only and are not meant to demonstrate different frequency light.

A schematic of the reactor utilized in the investigations presented in chapters three and four is shown in Figure 2.1[12, 13]. The position of the reactor relative to the ATR cell is detailed in Figure 2.3, surrounding the area denoted "contact mass in reactor". Not pictured is the flexible heating tape (Omega Engineering) used to wrap the reactor and aluminum foil that is placed over the heating coils surrounding the reactor to prevent heat loss.

2.4.4 IN SITU ATR CELL UTILIZED IN AMMONIA FORMATION ON IRON-SULFUR SURFACES INVESIGATIONS

Two different ATR accessories were utilized depending on the desired experimental temperature. The 22 ^{o}C and 70 ^{o}C experiments were conducted in a Germanium (Ge) multibounce ATR accessory (Pike Technologies), whereas the 120 ^{o}C experiments utilized a diamond single bounce ATR accessory (Specac) which was pressurized with 50 bar of UHP argon to elevate the boiling point of H_2O. Schematics of both cells are shown in Figure 2.5. Conducting in situ ATR-FTIR measurements involving liquid / solid interactions using aqueous solutions at 120 ^{o}C requires an overpressure that is significant enough to raise the boiling point of the solution above the desired reaction temperature. In the investigation presented in chapter five, an overpressure of ~50 bar UHP argon was used. It is imperative that the gas does not participate in the reaction chemistry. It is also useful to heat the ATR cell "dome" (the top of the reactor cell) to a temperature slightly above that of the diamond puck so as to prevent any migration of the aqueous phase toward the coolest areas of the cell. This is especially true for reactions that last for several days.

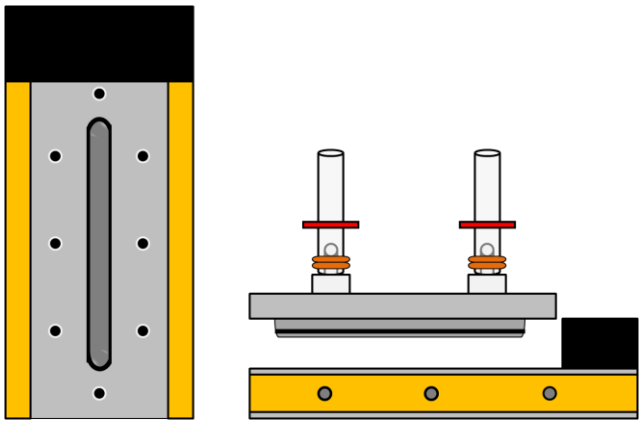

(a)

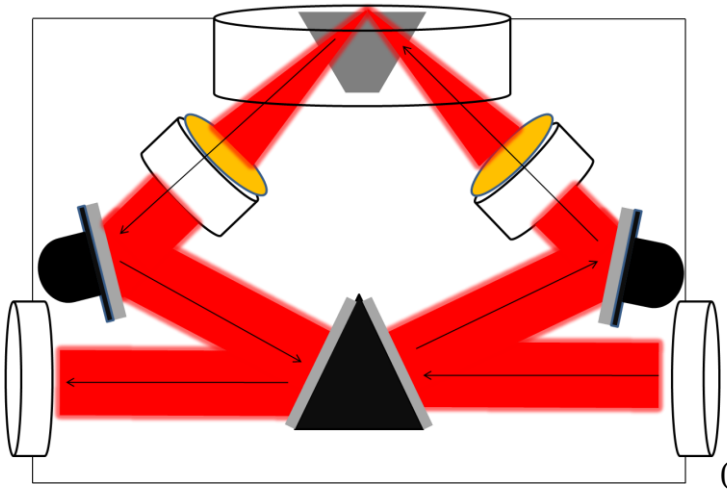

(b)

Figure 2.5: Schematics of the (a) multibounce ATR cell and (b) single bounce ATR cell with optics box.

2.5 ANALYTICAL METHODOLOGY

2.5.1 GAS CHROMATOGRAPHY

Gas chromatography is arguably one of the oldest and most utilized analytical techniques available to chemists today, *and is exclusively utilized for* the gas phase separation and quantification of chemical mixtures. First and foremost, this technique requires that samples are in the gas phase at room temperature or can be volatilized into the gas phase upon injection into the inlet (by means of a syringe / septum or sampling valve). Upon entering the inlet, the gas phase sample mixes with the carrier gas (i.e. helium) and is transferred to the column by the carrier gas. As the carrier gas continuously passes through the column, the individual chemical species interact with the stationary phase. The degree of interaction is based on the chemical and physical properties of the sample, column, and carrier gas. Depending on the degree of interaction with the column, the chemical species will be more or less strongly retained on the column thus separating the mixture [14]. An exciting aspect showcasing the versatile sampling ability of gas chromatography is the ease at which the sampling valve can be coupled to ATR-FTIR reactor cells for comparison of chemistry at the solid surface with gas phase kinetic data. An example of this coupling is shown in Figure 2.2. We have taken advantage of this versatility in two separate investigations which are discussed in chapters three and four [12, 13].

2.5.2 ION CHROMATOGRAPHY

Ion chromatography (IC) is the second form of chromatography used in the work presented in this dissertation which is used to quantify various ions in solution [14]. In many cases, samples can be injected using a Luer-Lok^{tm} syringe port or equivalent, or

sampled using a sampling valve in the case of a continuous flow type setup. Once injected the sample mixture is then further mixed with the eluent (buffer solution) which serves a similar function to the carrier gas in gas chromatograph, and this mixture is carried through the column. The retention of ions on the column is inversely related to the ionic strength of the eluent. After separation of the ions, they are detected using a conductivity cell near the outlet of the column. The conductivity is measured and is plotted as a function of time, producing a chromatogram. The peak areas associated with each set of ions is quantified by standardizing the peak areas versus a standardized mixture of ions.

Ion chromatography was routinely used to analyze nitrite, nitrate and ammonia in the investigations presented in chapters five and six. The instrument used is a Dionex DX500 ion chromatograph with a 4 mm IonPac® AS4A-SC anion column and a 1.7 / 1.8 mM $NaHCO_3$ / Na_2CO_3 eluent. The concentrations were calculated from a linear 4-point calibration curve with R^2 values > 0.99.

2.5.3 X-RAY FLUORESCENCE SPECTROSCOPY

X-ray fluorescence spectroscopy (XRF) is a technique that is used for elemental analysis of solids. Both benchtop and handheld field instruments are heavily used in fields of study requiring quantitative information of solids. The technique involves exciting a solid sample with an x-ray source or other high energy beam and detecting the emitted light.

Mechanistically, fluorescence occurs when energy is absorbed by an electron in the ground state, elevating it into an excited state, leaving a “hole” behind [15]. This hole can then be filled by electrons that reside in more energetic states. In order for an electron

of higher energy to fill the hole left behind from the excited electron, it must release energy in the form of a photon. The energy of the emitted photon is equal to the energy difference between the excited and ground state.

2.5.4 X-RAY PHOTOELECRON SPECTROSCOPY

X-ray photoelectron spectroscopy (XPS), like XRF, is also used for elemental analysis of solids, but differs slightly in that the kinetic energies of the ejected photoelectrons are detected. More specifically, photoelectrons are generated, segregated by energy, detected and recorded. These energies are typically expressed as binding energies which are calculated by equation 2.3 [16-23].

$$E_b = h\nu - E_k - \phi \qquad (2.3)$$

where:

E_k	kinetic energy of ejected electron
$h\nu$	x-ray photon energy of source
E_b	binding energy of photoelectron
ϕ	work function of the analyzer

Quantitative chemical information regarding oxidation state of the first few atomic layers of a solid can be elucidated from XPS spectra. Since x-ray energies excite core electrons, the ejected electrons, called photoelectrons, can act as fingerprints of an element since these core electrons are somewhat less sensitive to adsorbates and changes in local environment than valence electrons. In general, the signals obtained in XPS yield information on electronic structure of electrons within the atom which is sensitive to

changes in the local environment around the atom. A schematic representation of electron phenomenon behind XPS and XRF techniques are compared at the electronic level in Figure 2.6.

Table 2.2: Gas chromatograph analytical parameters.

Parameter	Value
Injection Temperature	200 ^{o}C
Detector Temperature (TCD)	270 ^{o}C
Helium Carrier Gas	20 PSI (inlet pressure)
Flow Rate	10.5 cm / s

Table 2.3: Temperature ramp program from GC investigations in chapters three and four.

Parameter	Duration
40 ^{o}C (initial temperature)	5 minutes
15 ^{o}C per minute to 250 ^{o}C (Ramp rate)	14 minutes
250 ^{o}C (final temperature)	3 minutes

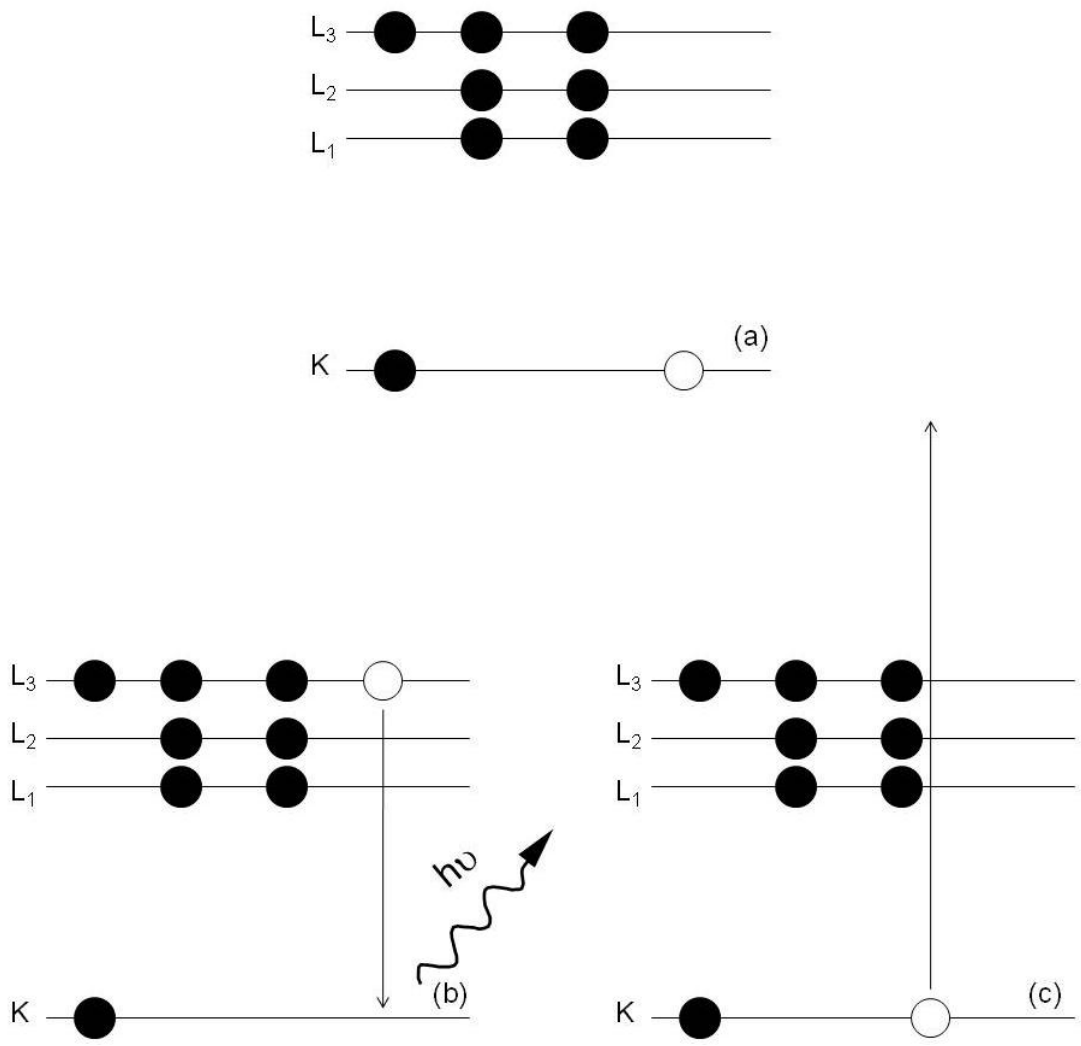

Figure 2.6: Schematic representation of core shell processes generating x-ray fluorescence (a,b) and x-ray photoelectrons (a,c) [23]. Electron arrangement prior to irradiation is shown (a). Upon irradiation, the excited electron represented by (○) can (b) be promoted to higher energy shell and subsequently undergo a relaxation mechanism, resulting in the release of a photon. Alternatively, irradiation can also result in (c) the direct release of a photoelectron.

References

[1] Rickard, D., *Stockholm Cont. Geology*, 20 (1969) 67-95.

[2] Michel, F.M., Antao, S.M., Chupas, P.J., Lee, P.L., Parise, J.B., Schoonen, M.A.A., *Chemistry of Materials*, accepted (2005).

[3] Singireddy, S., Gordon, A.D., Smirnov, A., Vance, M.A., Szilagyi, R.K., Schoonen, M.A., Strongin, D.R., *Astrobiology*, (Submitted).

[4] Bostick, B.C., Fendorf, S., and Helz, G. R., *Environmental Science & Technology*, 2003, 37, 285-291

[5] Brandes, J.A., Boctor, N.Z., Cody, G.D., Cooper, B.A., Hazen, R.M., Yoder, H.S., Jr., *Nature*, 395 (1998) 365-367.

[6] Smirnov, A., Hausner, D., Laffers, R., Strongin, D., Schoonen, M., *Geochemical Transactions*, 9 (2008) 5.

[7] Smirnov, A., Schoonen, M.A.A., Tosca, N.J., Chidambaram, D., Halada, G., Luptak, B., Abiotic formation and fate of ammonium in the Hadean Ocean, in: *NAI General Meeting*, Boulder, CO, 2005

[8] Summers, D.P., Chang, S., *Nature*, 365 (1993) 630-632.

[9] Summers, D.P., *Origins of Life and Evolution of the Biosphere*, 35 (2005) 299-312.

[10] Schoonen, M.A.A., Xu, Y., *Astrobiology*, 1 (2001) 133-140.

[11] Harrick, N.J., *Internal Reflection Spectroscopy, 2nd ed.*, John Wiley and Sons, New York, 1979.

[12] Gordon, A.D., Hinch, B.J., Strongin, D.R., *Catalysis Letters*, 133 (2009) 14-22.

[13] Gordon, A.D., Hinch, B.J., Strongin, D.R., *Journal of Catalysis*, 266 (2009) 291-298.

[14] Harris, D.C., *Quantitative Chemical Analysis, 6th ed.*, W.H. Freeman and Company, New York, 1982.

[15] Beckhoff, B., Kanngießer, B., Langhoff, N., Wedell, R., Wolff, H.E., *Handbook of Practical X-Ray Fluorescence Analysis, 1st ed.*, 2006.

[16] Somorjai, G.A., Li, Y., *Introduction to Surface Chemistry and Catalysis*, John Wiley & Sons.

[17] Moulder, J.F., Stickle, W.F., Sobol, P.E., *Handbook of X-Ray Photoelectron Spectroscopy*, Perkin Elmer, Eden Prairie, Mn, 1992.

[18] O'Connor, D.J., Sexton, B.A., Smart, R.S.C., *Surface Analysis Methods in Materials Science*, D.J. O'Connor, B.A. Sexton, R.S.C. Smart (eds.), Springer, Berlin, London, 2003.

[19] Prutton, M., *Surface Physics*, Oxford University Press, New York, 1975.

[20] Wagner, C.D., Riggs, W.M., Davis, L.E., Moulder, J.F., Mullenberg, G.E., *Handbook of X-ray Photoelectron Spectroscopy*, Perkin Elmer, Eden Prairie, Mn, 1979.

[21] Ghosh, P.K., *Introduction to Photoelectron Spectroscopy*, John Wiley & Sons, New York, 1979.

[22] Briggs, D., Seah, M.P., *Practical Surface Analysis by Auger and X-ray Photoelectron Spectroscopy*, John Wiley & Sons, Ltd., New York, 1983.

[23] Christmann, K., Top*ics in Physical Chemistry: Introduction to Surface Physical Chemistry*, Springer-Verlag, New York, 1991.

CHAPTER 3

EFFECTS OF INDIVIDUAL PROMOTERS ON THE DIRECT SYNTHESIS OF METHYLCHLOROSILANES

3.1 OVERVIEW

The world's silicones are produced from silane precursors which are generated by a process known as the Direct Synthesis. This process has been empirically optimized through years of trial and error within the industrial context. The work presented in the following two chapters is directly related to the development of an in situ reaction monitoring systems that will predict drops in overall methylchlorosilane production as well as drops in selectivity based on surface chemistry that is observed.

The industrially relevant Direct Synthesis involves the reaction of methyl chloride with silicon in the presence of a copper catalyst (promoted with Zn, Sn, and P), termed the contact mass, to form methylchlorosilanes. In situ attenuated total reflection Fourier transform infrared spectroscopy (ATR-FTIR) coupled with flow reactor studies was used to help understand the relationship between the composition of the working catalytic surface and product selectivity during reaction (1 bar CH_3Cl at 300 ^oC). Promotion of copper-silicon contact masses with Sn and Zn increased the selectivity of the reaction for dimethyldichlorosilane compared to P-promoted and copper-silicon (unpromoted) contact masses. Results showed that the rate of Si conversion associated with the Sn-promoted contact mass was higher than the Si conversion rate associated with the Zn and unpromoted contact masses. ATR-FTIR results suggested that Sn promotion led to a stabilization and relatively high concentration of surface methyl species. In contrast to Sn

or Zn promotion, P promotion led to significant methyl fragmentation on the contact mass surface, consistent with its relatively low selectivity toward dimethyldichlorosilane.

3.2 INTRODUCTION

The Direct Synthesis (DS) of methylchlorosilanes from the reaction of methyl chloride (MeCl), CH_3Cl, with silicon, also known as the Rochow Synthesis, was developed by Eugene Rochow for the efficient production of methylchlorosilane monomers for the silicone industry [1]. The most desirable of these monomers to date has been dimethyldichlorosilane (DMDCS), but it is possible that future applications may require different monomeric precursors. The contact mass associated with the DS is comprised of silicon with 1–10% (by weight) copper that constitutes the catalytic component.

The unpromoted contact mass, however, is relatively unselective for the synthesis of DMDCS until parts-per-million amounts of promoters, such as Sn, Zn, and P are added to the unpromoted contact mass. These additives are termed promoters, since they increase the reactivity and selectivity of the unpromoted contact mass toward the desired methylchlorosilanes. The DS reaction can be represented by the following reaction:

$$MeCl_{(g)} + Si_{(s)} \xrightarrow{\text{Cu catalyst, Promoters (300° C)}} Me_xSiH_yCl_z$$

Where x+y+z=4

Due to the importance of the DS, the mechanistic details that contribute to product formation have been studied for decades. Excellent reviews have summarized much of the understanding that has resulted from prior studies [2–5]. While the mechanistic detail

by which the promoters act is still lacking, there are general statements that can be made concerning the effects of promoters, such as Zn, Sn, and P, on the reactivity and selectivity of the unpromoted contact mass. Prior research, for example, has shown that a copper-silicon contact mass promoted with only Zn leads to an increased selectivity for DMDCS although it typically does not have a significant effect on the rate [6,7]. In contrast, contact masses promoted with only Sn exhibit an enhanced rate compared to Zn and a higher selectivity toward DMDCS. It has been postulated in prior studies that zinc increases silicon diffusion to sites above a threefold copper site [8]. Phosphorus (typically added as copper phosphide) was introduced as a promoter for the DS in 1990 by the Dow Corning Corporation. The addition of copper phosphide to the contact mass (with Zn and or Sn) increases the selectivity for DMDCS [9]. It has been postulated that copper phosphide promotes active phase formation. No published studies exist, however, which have investigated the effect of phosphorus when it is the only promoter present in a contact mass. Prior studies that have investigated the action of promoters [3] on the DS have utilized a range of experimental techniques that have included temperature programmed desorption [10], scanning electron microscopy [8,11], scanning Auger electron microscopy [12,13], X-ray diffraction [12], and X-ray photoelectron spectroscopy [12]. These previous studies have largely studied the influence of promoters on silicon diffusion processes and have not generally addressed the effect of the promoters on the dissociative chemisorption of MeCl and the resulting generation of methyl and chlorine surface groups. Furthermore, these prior studies have largely consisted of ex situ studies that have investigated the composition of the DS contact mass after reaction. Hence, information that is concerned with the composition of the surface

monolayer associated with the working DS contact mass is not yet available. In contrast to prior studies, research presented in Chapters 3 and 4 of this dissertation investigates the chemical structure of the working catalytic surface in situ under real conditions. Attenuated total reflection Fourier transform infrared spectroscopy (ATR-FTIR) was used to investigate the structure of the working contact masses as a function of promoter and reaction time. This information on the structure of the surface monolayer was combined with studies of the temporal behavior of the product selectivity as a function of promoter. Relationships between the structure of the surface monolayer under working conditions and product selectivity were developed that help to elucidate the promoter action. To the best of our knowledge, this is the first study to investigate the DS in situ with an emphasis on understanding the effect of promoters on the surface concentration and reactions of surface intermediates.

3.3 MATERIALS AND METHODS

Silicon, copper, tin, and zinc used to make the various contact masses in this study were purchased from commercial suppliers. Silicon (98.5%), zinc (≥99%, powder), and tin (≥99%) were obtained from Aldrich and copper (in the form of CuCl, ≥99%) was obtained from Sigma–Aldrich. CuP (99.999%) was obtained from American Elements. The percentage weight compositions of the Cu and promoters associated with the contact masses used in this study were typical of those described in the literature [3,4] and consisted of the following: (1) unpromoted, 10% Cu; (2) zinc promoted, 10% Cu and 0.06% Zn; (3) phosphide promoted, 10% Cu and 0.02% P (added as CuP); (4) tin promoted, 10% Cu and 0.004% Sn. Each contact mass formulation was stored as a slurry in hexane.

Individual contact masses with and without promoter (~50 mg) were added as a slurry on to a diamond ATR lens that was integrated into an ATR-FTIR reaction cell (Specac Supercritical Golden- Gate ATRTM and Thermo Electron Magna 560). This cell was in line with a fixed bed stainless steel reactor that contained 1.5 g of the same contact mass that was present in the ATR reaction cell. The ATR-FTIR cell and reactor were individually resistively heated to 300 ^{o}C. The cell and reactor were set up in series using Teflon (DuPont^{TM}) tubing. A schematic of the experimental setup is shown in Figure 3.1. Control experiments were performed to verify that the small amount of product that presumably formed in the gas stream from the 50 mg of contact mass in the ATR reactor had no observable influence on the product distribution, silicon conversion, and MeCl conversion derived from the effluent of the fixed reactor bed. A sampling valve (Valco) was present at the exit of the flow reactor and aliquots of the effluent were bypassed into a gas chromatograph (GC) at specified times for product analysis. The GC (HP 5890) was equipped with a 15 m silica column and a thermal conductivity detector. The sensitivity of the thermal conductivity detector for the different products analyzed in Chapters 3 and 4 was determined by passing known amounts of pure samples through the GC and measuring the detector response.

A typical experimental run consisted of flowing argon (99.997%, Air Products) at a rate of 0.1 standard cubic feet / h continuously over the contact mass mixture until both the reactor and cell were at 300 ^{o}C. A moisture trap (Vici Moisture Trap, model T100-2) was placed inline to minimize contaminant in the gas stream. No oxygen scrubber was used in this setup. The Ar was kept flowing for an additional period of 1 h at 300 ^{o}C. $SiCl_4$ product was detected after the contact mass reached 300 ^{o}C, but this product

decreased in yield over time and by 2–3 h it was no longer detectable. We suspect that this product was the result of chlorine release during the alloying process between the Si and Cu (initially present as CuCl). At this point an infrared spectrum was obtained and then the Ar was replaced by MeCl (99.99%, Matheson Tri Gas). The infrared spectrum taken in the Ar flow served as the reference for subsequent data taken in the presence of MeCl. GC analysis of the effluent from the reactor and infrared data were acquired every 15 min during the DS reaction. Experimental runs reported in this chapter lasted for times up to 6 h. MeCl conversions (in %) quoted in this chapter were calculated on the basis of Eq. (1) while selectivity and -Δmass / h (referred to as Si conversion) quantities were calculated on the basis of Eqs. (2) and (3), respectively. GC peak areas were determined using Peak Simple software (SRI Instruments):

$$MeCl\ conversion\ (\%) = \frac{moles\ silane}{moles\ silane + moles\ MeCl}\ x\ 100 \qquad (3.1)$$

$$Selectivity\ (\%) = \frac{moles\ silane_x}{\sum moles\ silane}\ x\ 100 \qquad (3.2)$$

$$-\frac{\Delta mass}{h} = \frac{moles\ Si_{final} - moles\ Si_{initial}}{moles\ Si_{initial}\ \mathrm{x}\ reaction\ time} \qquad (3.3)$$

3.4 RESULTS AND DISCUSSION

Figure 3.2 displays the selectivity for DMDCS, dichloromethylsilane (DCMS), and trichloromethylsilane (TCMS) as a function of exposure time to MeCl at 300 ^{o}C for the unpromoted, P-promoted, Zn-promoted, and Sn-promoted contact masses. Other products observed included dimethylchlorosilane and trimethylchlorosilane but the data for these products are not presented.

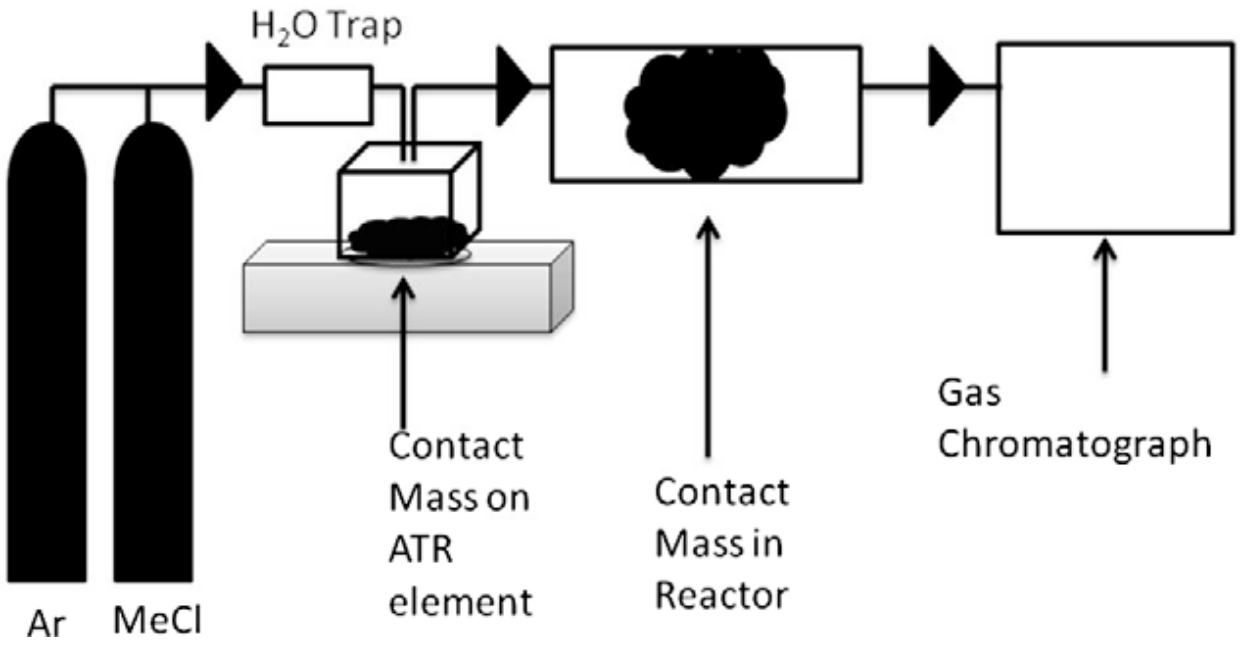

Figure 3.1: Schematic of the experimental setup used in studies presented in chapters 3 and 4. MeCl was first flowed over 25 mg of contact mass on a diamond ATR element. The MeCl reactant was then passed through a flow reactor containing 1.5 g of contact mass. The production of methylchlorosilanes was determined by passing samples of the effluent through a gas chromatograph.

The contact mass with the highest selectivity toward DMDCS (Figure. 3.2, top) contained Sn promoter (72%). The maximum selectivity for this specific product associated with the Zn-promoted, P-promoted, and unpromoted contact masses was 53%, 17%, and 31%, respectively. Experimental runs were limited to 6 h.

While the selectivity of the P-promoted contact mass was exceedingly low toward DMDCS, it exhibited the highest selectivity (65%) of the four different contact masses toward DCMS (Figure 3.2, middle). Interestingly, the initial selectivity of the unpromoted catalyst for this product was ~0% after 0.5 h, but it rose to a value of 28% after 5 h. The other three contact masses showed less significant changes in their selectivity toward this product over the 6 h time period. Finally, Figure 3.2 (bottom) displays TCMS selectivity for the different contact masses. For this product, the unpromoted contact mass showed the highest selectivity, while the P- and Sn promoted contact masses exhibited the lowest selectivities (~13%). Figure 3.2 displays MeCl conversion as a function of reaction time for the different contact masses. Initially, the Sn- and P-promoted catalysts each showed a MeCl conversion of ~5%. However, the Sn promoted system exhibited a significant increase in MeCl conversion as the DS reaction proceeded over the 5 h reaction time. At 5 h, the Sn-promoted catalyst reached a MeCl conversion of 30%, which was a factor of 7 higher than any of the other catalyst formulations. Both the P-promoted and Zn-promoted formulations exhibited MeCl conversions that never rose above 5% within the first 2 h. After this time, both of these systems exhibited a small drop in the amount of MeCl conversion; albeit the decrease was only 2–3%. The unpromoted catalyst showed the poorest MeCl conversion, never exceeding 2–3%. Figure 3.4 exhibits the -Δmass / h that is based on the weight difference

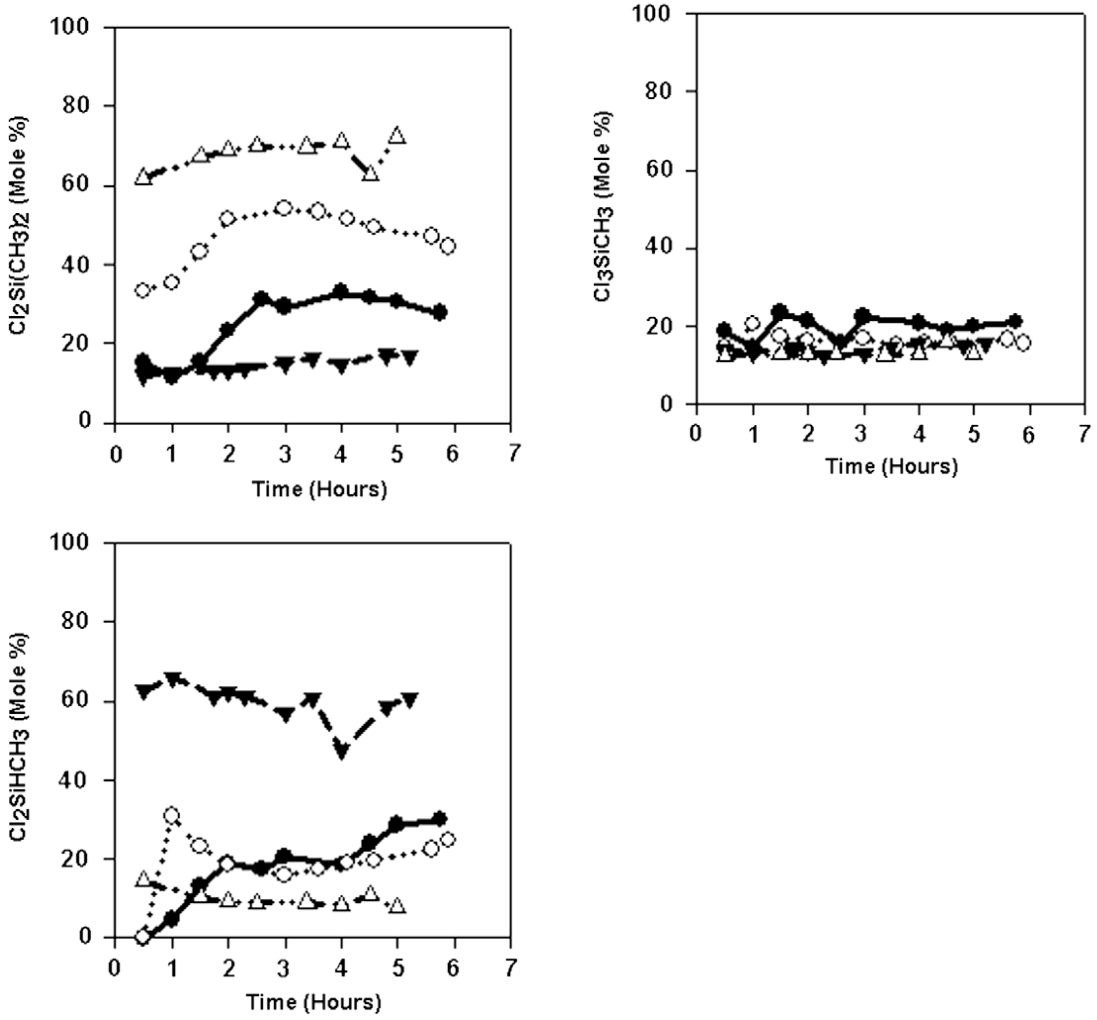

Figure 3.2: The selectivities for DMDCS [$Cl_2Si(CH_3)_2$], DCMS [Cl_2SiHCH_3], and TCMS [Cl_3SiCH_3] plotted as a function of time for the unpromoted (●), P-promoted (▼), Sn-promoted (Δ), and Zn-promoted (O) contact masses.

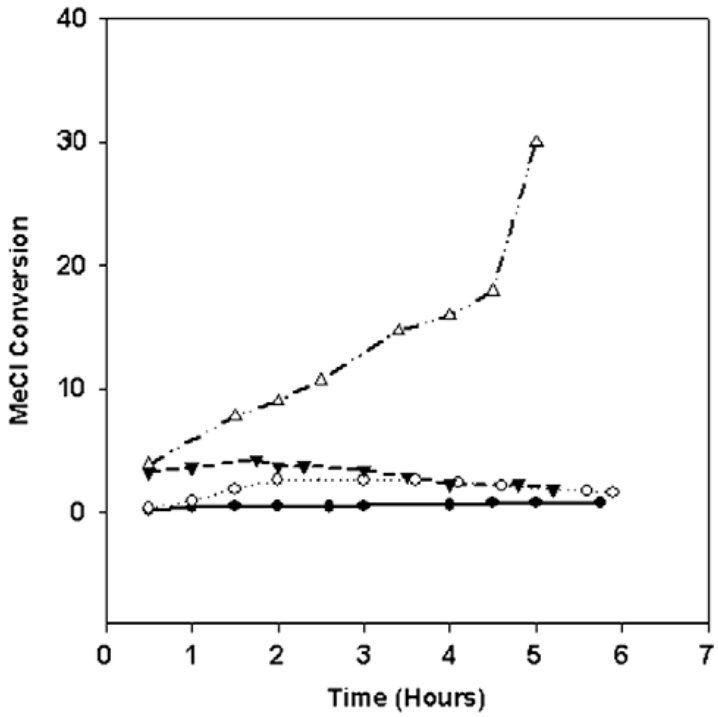

Figure 3.3: MeCl conversion plotted as a function of time for unpromoted (•), P-promoted (▼), Zn-promoted (Δ), and Sn-promoted (O) contact masses. The unpromoted contact mass demonstrates very low MeCl conversion throughout the run. The P-promoted contact mass has high MeCl conversion earlier in the run, but decreases after two h. The Zn-promoted contact mass shows a longer induction period than the other promoted contact masses, requiring 3 h to reach maximum MeCl conversion. The Sn-promoted contact mass shows greater MeCl conversion than the other contact masses.

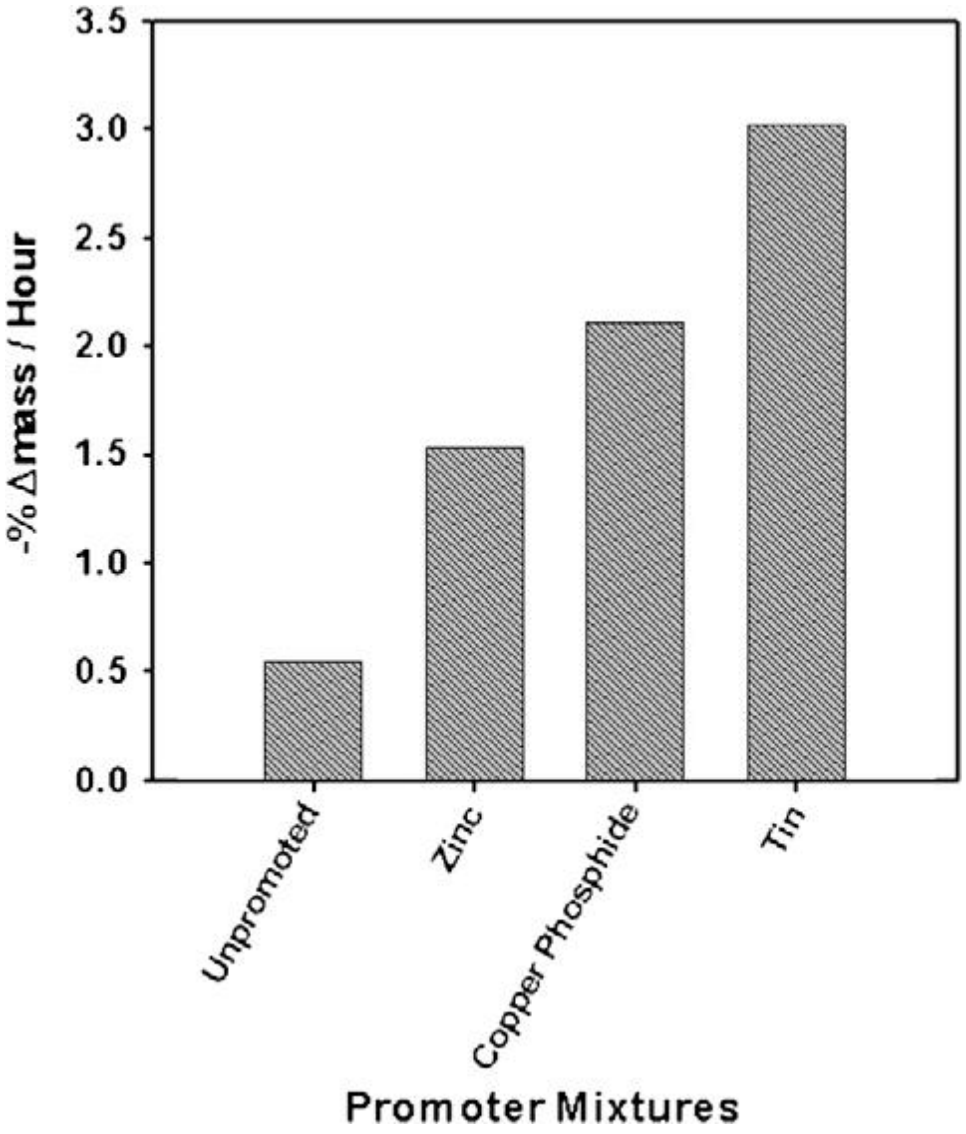

Figure 3.4: The relative percentage change in mass per hour for the unpromoted, Zn-promoted, P-promoted, and Sn-promoted contact masses. Note that since overall mass is lost due to product formation during a run, the Δmass is a negative value. We assume that this weight loss to largely due to the conversion of Si to gaseous product and hence associate -Δmass / h with the Si conversion rate.

of the different contact masses before and after a 6 h exposure to MeCl. It is assumed that this measure is primarily due to the rate of Si conversion to gaseous product, but the addition of carbon and chlorine species that are inactive on the surface likely has an effect on the mass change of the contact mass. Examination of these data shows that the rate of Si conversion (i.e., -Δmass / h) is 50% higher for the Sn-promoted sample than for the P- promoted sample. The MeCl conversion data, however, presented above show a value about 7 times higher for the Sn-promoted sample. We suspect that Cl deposition of the Sn-promoted contact mass is leading to a smaller difference in weight of the contact mass before and after MeCl exposure. We do not believe CH_3 groups (or fragments thereof) are responsible for the slight mass discrepancy in this case, since infrared data shown next suggest that coking or CH_3 fragmentation on the Sn-promoted contact mass is not occurring to a significant extent.

However, even if the data in Figure 3.4 are treated on a qualitative level, the observation that the Si conversion rate increases in the order of unpromoted < Zn-promoted < P-promoted < Sn-promoted agrees well with prior research [5].

It is useful to further compare our reaction results to those of prior studies of the action of promoters on the DS. The majority of prior research has been focused on the synergistic effects of multiply promoted contact masses [14]. Less research has investigated the reactivity and selectivity of singly promoted catalysts [11,15].

Prior research by Ward et al. showed that a Zn-promoted contact mass exhibited a higher TCMS / DMDCS ratio than a Sn-promoted contact mass (0.09 vs 0.12) [16]. The rate of product formation in the Sn-circumstance was over a factor of 2 greater than the Zn-promoted contact mass. Another prior study conducted by Rethwisch et al. showed a

TCMS / DMDCS ratio of 0.34 for the Zn-promoted contact mass and a ratio of 0.58 for the Sn-promoted active mass [6]. On a qualitative level our results agree with these prior results.

We find that Sn promotion results in the highest selectivity toward DMDCS, but it is only marginally higher than the selectivity exhibited for the Zn-promoted catalyst. Furthermore, we find that Sn promotion results in the highest MeCl and Si conversion rate. These experimental observations are consistent with the prior studies that show that Sn promotion increased the rate of methylchlorosilane production exceeding that of Zn promotion. We now present in situ infrared studies that help to develop a microscopic understanding of the origin of the different promoter actions.

3.4.1 IN SITU IDENTIFICATION OF SURFACE INTERMEDIATES ON THE DS CONTACT MASS

Figure 3.5 displays in situ ATR-FTIR data associated with the CH stretching region that was obtained after the unpromoted, P-promoted, Zn-promoted, and Sn-promoted contact masses were exposed to argon for 3 h and then to MeCl for 0.5, 2, and 4 h at a temperature of 300 ^{o}C. Table 3.1 summarizes our mode assignments associated with the various surface species observed on the copper-silicon contact masses. All the spectra associated with MeCl exposure exhibit modes that are attributed to the C–H stretches of adsorbed CH_3 and fragment(s) of this group (i.e., CH_x (x=1,2)). No evidence of gaseous MeCl modes was observed in any of the ATR-FTIR spectra. We mention that all the plots include a spectrum labeled ‘‘under argon.” This spectrum is representative of the respective contact mass after being exposed to a flow of Ar-gas for 3 h at 300 ^{o}C

Table 3.1: Summary of assignments based on ATR-FTIR data (all data in cm^{-1}).

Surface Species	**Cu / Si**	**Zn / Cu / Si**	**P / Cu / Si**	**Sn / Cu / Si**
$\nu_{as}(CH_3)$	3000	2995	2977	2988
$\nu_{s}(CH_3)$	2954	2950	2939	2940
$\nu_{as}(CH_2)$	-	-	2880	-
ν_{as}(Si-O-Si)	1193	1195	1190	1201
ν_{s}(Si-O-Si)	1051	1040	1030	1047
$\rho(CH_3)$	1276	1276	1276	1276
$\delta(CH_3)$[a]	~1205	~1205	~1205	~1205
ν_{as}(Si-O)	1120	1139	1122	1145
ν(C-O)[b]	-	-	-	1100
$\tau(CH_2)$	-	-	1010	-
ν_{s}(Si-O)	1004	990	980	990
$\delta(O_3Si-H)$	~900	~900	~900	~900
ν(Si-O)[b]	-	-	-	925
δ(Si-H)	~820	~820	~820	~820

[a] obscured by ν_{as}(Si-O-Si) and is not labeled in figures.
[b] resulting from methoxy absorbances

prior to the introduction of MeCl. All these control spectra show minimal absorbance in the C–H region, emphasizing that absorbances that build up in this spectral region are due to the dissociative adsorption of MeCl on the contact mass surfaces. Infrared modes that we attribute to adsorbed CH_3 are in good agreement with prior research that has investigated the thermal chemistry of CH_3 on pure single crystalline silicon surfaces. Kong et al. investigated the thermal chemistry of CH_3 groups on Si(111) using infrared spectroscopy and assigned the asymmetric and symmetric methyl stretches to 2955 cm^{-1} and 2890 cm^{-1} absorption features, respectively [17]. In an earlier work, Colaianni et al. assigned the C–H stretches of CH_3 on silicon to absorbances at 2990 cm^{-1} and 2930 cm^{-1} [18]. Upon heating to 575 K they induced the fragmentation of the CH_3 group to an sp^3-hybridized CH_2 mode and assigned modes for this species at 2920 cm^{-1}, which is slightly higher than our assignment at 2880 cm^{-1} (most apparent on the P-promoted contact mass). The presence of promoter and / or copper on the surface of the contact mass provides likely explanations for the differences in C–H positions between this research and prior studies.

It is useful to bring forward some general observations that can be made concerning differences in the mode positions and relative mode intensities between the different contact mass formulations. After equivalent exposure times to MeCl at 300 ^oC, mode intensities attributable to CH_3 are higher by a factor of 10 (notice the absorbance scales) on the Sn-promoted and P-promoted contact masses than on the unpromoted and Zn-promoted contact masses.

Associated with the P-promoted system, however, is an increase in mode intensity attributable to CH_2 that is greater than any other contact mass formulation. Figure 3.6

displays integrated peak areas of the $\upsilon_{as}(CH_3)$ mode for the P- and Sn-promoted contact masses over 5 h of reaction time. Note that integrated peak areas as a function of reaction time shown in Figure 3.6 were derived from additional infrared data we obtained over what is displayed in Figure 3.5. Our analysis was restricted to the Sn- and P-promoted surfaces due to the increased CH_3 stretching intensity that allowed for more accurate peak fitting.

Analyses of these data show that both surfaces exhibit a significant increase in CH_3 concentration over 5 h of reaction. After 2 h of reaction the surface CH_3 concentration associated with the P-promoted surface exceeds that of the Sn-promoted surface by a factor of ~2. While the P-promoted surface exhibits a relatively high CH_3 surface concentration, it does not exhibit a high MeCl conversion compared to the Sn-promoted contact mass. We infer from these experimental observations that the surface concentration of CH_3 alone is not a particularly good indicator of contact mass selectivity or reactivity. The low MeCl conversion associated with the P-promoted contact mass suggests that the CH_3 and surface hydrogen (from CH_x (x=1,2)) that build up on this surface are not being converted to methylchlorosilane product as efficiently as on the Sn-promoted contact mass. In the Sn-promoted case, the MeCl conversion is as much as 7 times greater than that of the P-promoted surface. Based on this comparison, we speculate that the lower steady state CH_3 concentration on the Sn-promoted surface results from a more substantial fraction of the CH_3 resulting from MeCl dissociative chemisorption being converted to methylchlorosilane product than on the P-promoted surface. The increased fragmentation of the CH_3 group on the P-promoted surface is consistent with its selectivity toward DCMS, but this fragmentation may also be resulting

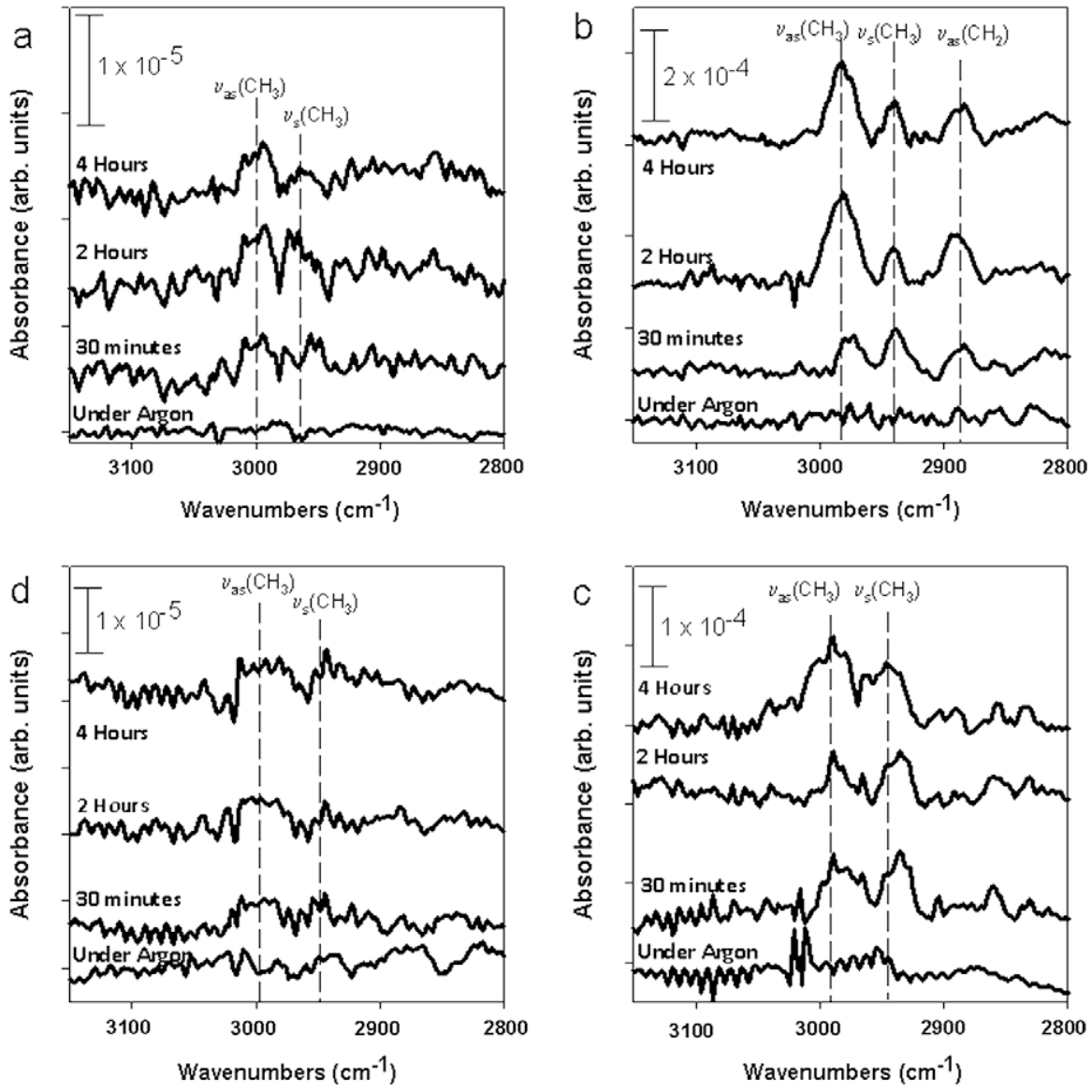

Figure 3.5: ATR-FTIR of the CH stretching region for the (clockwise from top left) unpromoted (a), P-promoted (b), Sn-promoted (c), and Zn-promoted (d) contact masses as a function of reaction time at 1 bar MeCl at 300 ^{o}C. All spectra were obtained in situ.

in species (C, CH_x (x=1,2) and / or surface hydrogen) that bind to and block active Si sites that ultimately lead to the lower MeCl conversion. The slight decrease in MeCl conversion associated with the P-promoted surface (see Figure 3.3) after 2–3 h of reaction may result from this coking of the surface.

The reason for the increase in MeCl conversion with time associated with the Sn-promoted surface is uncertain, but the result does suggest that the Sn-promoted contact mass is undergoing structural and / or compositional changes at the reacting surface during the DS reaction which are increasing its ability to form methylchlorosilane product. The Sn-promoted surface shows little evidence for the presence of C–H species that can be associated with CH_3 fragmentation, suggesting that this contact mass does not suffer from the coking and blocking of active sites that presumably is associated with the P-promoted surface. Hence, Sn promotion stabilizes the CH_3 group on the working surface.

Figure 3.7 displays the 800–1300 cm^{-1} spectral range for the different contact masses for the same time sequence shown in Figure 3.5 during their exposure to MeCl at 300 ^{o}C. Interestingly, the spectra are dominated by absorbances that we attribute to silicon–oxygen vibrations. Specifically, modes at 1190–1201 cm^{-1} and 1030–1051 cm^{-1} as well as modes at 1120–1145 cm^{-1} and 980–1004 cm^{-1} are assigned to silicon oxides and / or Si–O–Si suboxide networks. It is emphasized that these mode assignments are in excellent agreement with the extensive prior research that has investigated the oxidation of silicon surfaces [19].

We are not entirely certain why at least some oxide modes appear to increase in intensity with MeCl exposure time. We have carried out control experiments that exposed

pure Si powder (no Cu or promoter) to Ar for 1 h and then to MeCl for 6 h. In this circumstance we see no change in the intensity of the silicon oxide modes associated with the silicon by infrared spectroscopy. Hence, we argue based on these experimental observations that the alloying reaction of Cu with Si at 300 ^{o}C is at the root of this phenomenon [20]. It seems likely that residual oxygen contamination in the gas stream oxidizes Si (in a copper silicide) during the reaction. It must be noted that copper silicide oxidizes extremely rapidly relative to silicon [21]. Interestingly, no prior in situ studies have probed the composition of the DS contact mass during the reaction.

Hence, whether some oxidation of Si in the active Cu silicide component occurred in prior research or even in the working industrial catalyst cannot be addressed. We emphasize, however, that our reactor results are in good agreement with those of prior studies, and this brings up the possibility that oxygen impurities may play a role in altering the active site concentration (Si in the copper silicide) on the working DS catalyst.

Modes not associated with silicon oxides also appear in the 800–1300 cm^{-1} spectral region. One in particular that we attribute to a Si–H deformation mode, δ(Si–H), appears at 820 cm^{-1}. We believe a revealing aspect of these spectra is the increased absorbance due to Si–H in the case of the P-promoted contact mass and the absence of this absorbance in the Sn-promoted circumstance. This experimental observation is consistent with the P-promoted contact mass having a relatively high proportion of its C–H stretching intensity due to CH_x (x=1,2). Also, the absence of Si–H modes in the spectrum associated with the Sn-promoted mass is consistent with the lack of any significant CH_x (x=1,2) contribution to the C–H stretching

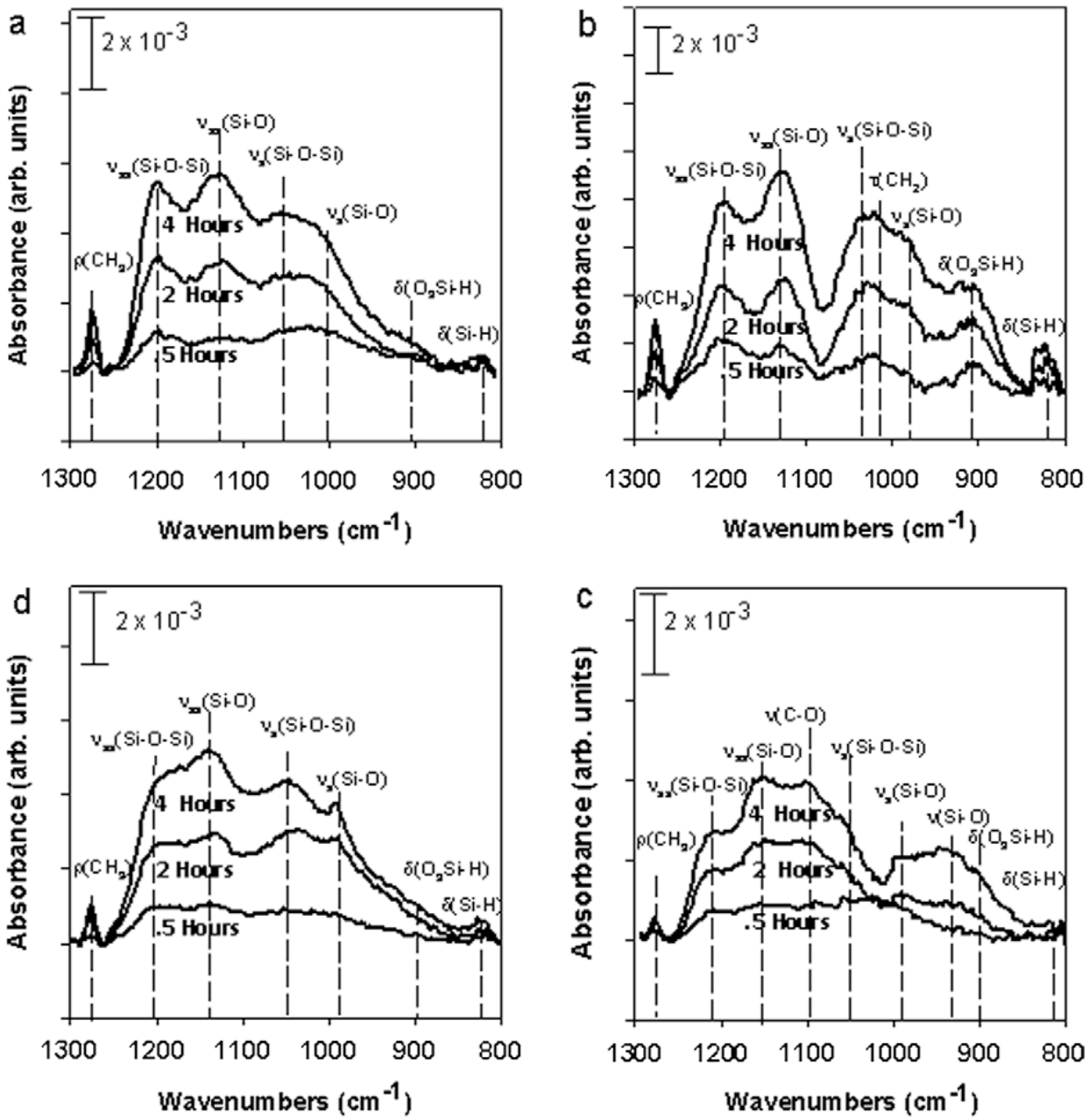

Figure 3.6: The 800–1300 cm^{-1} spectral region for the (clockwise from top left) unpromoted (a), P-promoted (b), Sn-promoted (c), and Zn-promoted (d) contact masses after 0.5, 2, and 4 h of reaction time under MeCl at 300 ^{o}C. Mode assignments are listed in Table 3.1.

region and is again consistent with the ability of Sn to stabilize CH_3 groups and prevent CH_3 decomposition on the contact mass surface.

Perhaps one of the more definitive peak assignments that can be made in the 800–1300 cm^{-1} spectral range is the $\rho(CH_3)$ mode at 1276 cm^{-1} that is due to CH_3 groups adsorbed on silicon [17,22]. We feel it is of note that the intensity of this peak does not vary dramatically between the different contact masses even though the Sn- and P-promoted contact masses exhibit C–H stretching spectral features at 2988 cm^{-1} and 2977 cm^{-1}, respectively that are a factor of 10 greater than the unpromoted and Zn-promoted contact masses. At least a fraction of the C–H stretching intensity associated with the Sn-promoted contact mass could be due to the presence of surface methoxy (i.e., Si–OCH3) group. This contention is bolstered by the appearance of a 1100-cm^{-1} mode that can be assigned to the υ(C–O) mode of methoxy in agreement with prior research of methoxy groups on Si single crystals [19]. The $\rho(CH_3)$ mode of methoxy typically appears near 1200 cm^{-1} [19], and this mode is presumably obscured by the relatively intense silicon oxide modes in this same region. A similar argument, however, cannot be made for the P-promoted contact mass (lacks an absorption feature at 1100 cm^{-1}), suggesting that the presence of methoxy cannot fully explain the lack of correspondence between the intensity of the $\upsilon(CH_3)$ and $\rho(CH_3)$ modes. It may be that the CH_3 coverage influences the $\upsilon(CH_3)$:$\rho(CH_3)$ ratio, but exploring this possibility will need to be addressed in further study.

While the presence of methoxy groups appears on the Sn-promoted contact mass surface, we cannot presume that these CH_3 groups leave the surface as methylchlorosilane product. We do suspect that this spillover of CH_3 groups to the silicon

oxide is a result of the ability of the Sn-promoted contact mass to facilitate MeCl dissociative adsorption. The P-promoted contact mass also exhibits a mode near 900 cm^{-1}, which, based on prior research, is assigned to the δ(O3Si–H) mode associated with hydrogen adsorbed on Si bound in a suboxide [19]. The presence of this mode is again consistent with the ability of the P-promoted contact mass to dissociate surface CH_3. The P-promoted contact mass also exhibits a mode at 1010 cm^{-1} that can be attributed to a twisting mode of adsorbed CH_2, consistent with CH_3 fragmentation. Interestingly, the Sn-promoted contact mass exhibits reduced spectral weight near 1060–1080 cm^{-1}, when compared to the unpromoted, P-promoted, and Zn-promoted contact masses at all the reaction times investigated with ATR-FTIR. Consistent with our contention above, we believe that the Si constituent of the Cu–Si alloy which forms in the contact mass undergoes a slow oxidation process with residual oxygen in the gaseous stream. We suggest that the presence of Sn inhibits Si oxide formation during or after the copper-silicon alloying reaction. This effect may be at least partly responsible for our experimental observation that the presence of Sn leads to a higher MeCl and Si conversion than the other contact masses.

While one of the promoter effects of Sn may be to stabilize the active copper silicide active site, another promoter action is to stabilize surface CH_3 and to prevent its dissociation to CH_x (x=1,2) species. Prior ultra-high vacuum-based research that investigated the effect of Sn on a single crystalline Si / Cu(100) surface supports this promoter effect of Sn [23]. In this prior study, the thermal chemistry of CH_3 on Si / Cu(100) led to the formation of trimethylsilane, but when Sn was present on the surface, tetramethylsilane was observed to desorb from the surface. This prior result again

suggests that Sn inhibits the decomposition of surface CH_3 consistent with the Sn-promoted contact mass showing higher selectivity toward DMDCS. This effect of Sn directly contrasts the promoter action exhibited by P in this study. In the P circumstance, the conversion rate of Si is relatively high, but a significant amount of CH_3 dissociation is observed to occur on this surface which is likely responsible for its decreased selectivity for DMDCS and increased selectivity for the less methylated product DCMS.

3.4.2 GENERAL COMMENTS AND SOME OUTSTANDING ISSUES

Finally, we offer some general comments about Sn and Zn promotion based on our experimental results. First, while the selectivity toward DMDCS is slightly higher in the case of Sn promotion, the amount of product based on the MeCl and Si conversion data is at least a factor of 2 higher than when Zn is present. Second, our results are consistent with Sn carrying a higher CH_3 surface concentration than the Zn-promoted surface. The difference in CH_3 concentration between the two surfaces may be due to a higher rate of MeCl dissociative chemisorption on the Sn-promoted surface, relative to a Zn-promoted surface. Prior research has suggested that because of the low melting point of Sn (232 ^{o}C), this promoter may increase the DS rate at 300 ^{o}C by fluidizing the surface through a Sn-induced decrease in the surface [5]. It may be that the ability of Sn to spread on the working surface enables this element to exhibit its promoter effect over a significant portion of the active surface area of the contact mass. Based on our results these promoter effects likely include the stabilization of surface CH_3 and the prevention of the oxidative destruction of Si at active sites via its reaction with residual oxygen. Based on our experimental observations, the promoter action of Zn is different from that of Sn. In contrast to Sn-promoted contact mass, the Zn-promoted contact mass exhibits a

surface CH_3 concentration during reaction that is closest to the unpromoted surface. The selectivity of the Zn-promoted surface toward DMDCS production and Si conversion rate, however, is significantly higher than the unpromoted contact mass even though the surface CH_3 concentration on both surfaces is similar. It may be that the promoter effect of Zn rests in its ability to increase the rate of active site formation (rather than affecting MeCl dissociative chemisorption), which has been suggested by prior research [8]. Such a possibility is presently being investigated in our laboratory by studying multiply promoted contact masses.

While we believe that the results of this study have given some insight into the effects of individual promoters on the DS, they have also brought up at least two issues that deserve further investigation. First, both the CH_3Cl conversion and CH_3 surface population increase over 6 h of the DS reaction under the experimental conditions used in the current study. Studies designed to investigate the changes on the contact mass during this period and to determine the point at which the CH_3 conversion achieves a constant value warrant attention in future studies. Second, the origin and effect of oxygen on the promoted DS contact masses also deserve further study. Our study suggests that Sn has an effect on Si–O bonds on the DS contact mass, but a more focused study on determining the effect of oxygen on the product selectivity also would appear to be a valid course of action in understanding the DS reaction.

3.5 SUMMARY

The DS has been investigated on Zn-promoted, Sn-promoted, P-promoted, and unpromoted copper-silicon contact masses at 1 bar MeCl at 300 ^{o}C. The Sn-promoted contact mass exhibits the highest reactivity as measured by its Si conversion rate and

selectivity toward DMDCS. In situ ATR-FTIR shows that this catalyst has a relatively high surface concentration of CH_3, but it is lower than that associated with the P-promoted catalyst. P-promotion increases the rate of Si conversion relative to both the Zn-promoted and unpromoted contact masses, but this promoter leads to the dissociation of surface CH_3 that goes on to form CH_x (x=1,2) surface species. Also, this contact mass formulation is most selective toward DCMS. At least a fraction of the methyl that is observable with ATR-FTIR on the Sn-promoted contact mass is thought to be due to methoxy groups that form on residual oxide associated with the Si component.The steady state concentration of CH_3 on the Zn-promoted catalyst was significantly less than either the Sn- or P-promoted contact masses, and was similar to the unpromoted sample. However, the Zn-promoted contact mass showed a high selectivity toward DMDCS.

References

[1] Rochow, E.G., *Journal of the American Chemical Society* 67 (1945) 963–965.

[2] Seyferth, D. *Organometallics* 20 (2001) 4978–4992.

[3] Lewis, K.M., Kanner, B., *Catalyzed Direct Reactions of Silicon*, Elsevier, Amsterdam, 1993.

[4] Lewis, L.N., *Chemistry of Organic Silicon Compounds 2* (1998) 1581–1597.

[5] Voorhoeve, R.J.H., *Organohalosilanes: Precursors of Silicones*, Elsevier, Amsterdam, 1967.

[6] Gasper-Galvin, L.D., Sevenich,D.M., Friedrich, H.B., Rethwisch, D.G., *Journal of Catalysis* 128 (1991) 468–478.

[7] Gasper-Galvin, L.D., Rethwisch, D.G. Sevenich, D.M. Friedrich, H.B., *Studies in Organic Chemistry*, Amsterdam, 49 (1993) 279–297.

[8] Floquet, N., Yilmaz, S.,Falconer, J.L., *Journal of Catalysis* 148 (1994) 348–368.

[9] Halm, R.L., Zapp, R.H., Streu, R.D., *Reduced formation of methyltrichlorosilane in the Rochow process in the presence of hydrogen*, US Patent Number 4,762,940, Dow Corning Corp., USA, 1990.

[10] Rethwisch, D.G., Olakangil, J.F., Wood, L.H., Miller, D.C., Wineland, J.D., in: *Silicon for the Chemical Industry VI*, Conference, Loen, Norway, June 17–21, 2002

[11] Ehrich, H., Born, D., Richter, K., Richter-Mendau, J., Lieske, H., *Applied Organometallic Chemistry* 11 (1997) 237–247.

[12] Lieske, H. Fichtner, H., Grohmann, I., Selenina, M., Walkow, W., Zimmermann, R., in: *Silicon for the Chemical Industry*, 1992

[13] Ehrich, H., Born, D., Richter-Mendau, J., Lieske, H., *Applied Organometallic*

*Chemistr*y 12 (1998) 257–264.

[14] Wessel, T.J., Rethwisch, D.G., Reaction *Kinetics and Catalysis Letters* 58 (1996) 7–12.

[15] Agarwala, J.P., Falconer, J.L., *International Journal of Chemical Kinetics* 19 (1987) 519–537.

[16] Ward, W.J., Ritzer, A., Carroll, K.M., Flock, J.W., *Journal of Catalysis* 100 (1986) 240–249.

[17] Kong, M.J., Lyubovitsky, J., Bent, S.F., *Chemical Physics Letters* 263 (1996) 1–7.

[18] Colaianni, M.L., Chen, P.J., Gutleben, H., Yates Jr., J.T., *Chemical Physics Letters* 191 (1992) 561–568.

[19] Michalak, D.J. Amy, S.R. Esteve, A., Chabal, Y.J. *Journal of Physical Chemistry C* 112 (2008) 11907–11919.

[20] Voorhoeve, R.J.H., Lips, J.A., Vlugter, J.C. *Journal of Catalysis* 3 (1964) 414–425.

[21] Corn, S.H., Falconer, J.L., Czanderna, A.W., *Journal of Vacuum Science and Technology* A 6 (1988) 1012–1016.

[22] Glass Jr., J.A., Wovchko, E.A., Yates Jr., J.T. *Surface Science* 338 (1995) 125–137.

[23] Zhang, X.V., Strongin, D.R., Goncharova, L.V. Ermakov, A.V., Hinch, B.J. *Journal of Physical Chemistry* B 108 (2004) 16213–16219.

CHAPTER 4

EFFECTS OF MULTIPLE PROMOTION OF THE DIRECT SYNTHESIS CONTACT MASS WITH P, Zn, AND Sn ON THE SYNTHESIS OF METHYLCHLOROSILANES

4.1 OVERVIEW

The Direct Synthesis, or Rochow Synthesis, involves the reaction of methyl chloride, CH_3Cl (MeCl), with Cu–Si contact masses (promoted with 1–2% of Zn, Sn, and P) to form methylchlorosilanes. Flow reactor studies (1 bar MeCl at 300 ^oC) showed that contact masses promoted with Zn, Sn, and P (triply promoted) demonstrated the highest Si and MeCl conversion at early reaction times. In situ infrared spectroscopy suggested that in contrast to the doubly promoted catalysts (where CH_3 groups were primarily bound to Si), surface CH_3 showed appreciable binding to the copper component of the triply promoted contact mass. This change in surface composition ultimately led to a drop in reactivity and selectivity of the triply promoted catalyst.

4.2 INTRODUCTION

The industrially relevant process by which methylchlorosilanes are formed via the reaction of methyl chloride, CH_3Cl (MeCl), with silicon is known as the Direct Synthesis (DS). The process is also known as the Rochow Synthesis due to its discovery by Eugene Rochow in the mid-twentieth century [1]. The DS allows for the cheaper and facile production of methylchlorosilane monomers for the silicone industry [1]. The reaction can be written as follows:

$$MeCl_{(g)} + Si_{(s)} \xrightarrow{\text{Cu catalyst, Promoters (300° C)}} Me_xSiH_yCl_z$$

Where x+y+z=4

The DS is catalyzed with copper, and over time it was found that the presence of parts-per-million amounts of Zn, Sn, and P (termed promoters) on the contact mass promoted or increased the rate of production and the selectivity for the most desirable product, dimethyldichlorosilane (DMDCS).

Because of the industrial importance of the DS for the production of silicones, there have been many prior studies that have mapped out the effects of promoters on the selectivity and reactivity of contact masses for the DS [2–10]. It is the general consensus from the literature that when specific combinations of promoters are added together, a synergism between the promoters is typically observed.

Prior research has also used a variety of surface analytical techniques to investigate the DS catalyst after reaction [11–17]. Missing from prior research, however, has been in situ studies that investigate the working surface of the DS contact mass under reaction conditions. Toward this end, recent research from our laboratory [3] has investigated the effects of individually Zn-, Sn-, and P- promoted contact masses in situ with attenuated total reflection Fourier transform infrared spectroscopy (ATR-FTIR) at working conditions (1 bar MeCl, 300 ^{o}C) and have coupled these results with flow reactor studies that determined the effects of the promoters on the reactivity and selectivity of the contact masses.

In this chapter, we build on the singly promoted contact mass results detailed in our prior work [3] and expand our studies investigating doubly and triply promoted

contact masses. Specifically, we present and interpret results below that were obtained from in situ ATR-FTIR and flow reactor studies of Zn–Sn-, Zn–P-, Sn–P-, and Zn–Sn–P-promoted contact masses. Results obtained in situ give a view of the adsorbed monolayer associated with the working catalyst as a function of promoter mixture and we utilize this information to help understand the selectivity and reactivity of the different promoted contact masses. We also interpret our results from the multiply promoted catalyst in view of our prior studies of singly promoted contact masses to help develop an understanding of the origin of the cooperative effects between DS promoters.

4.3 MATERIALS AND METHODS

The various components used to make the contact masses used in this study (i.e., Si, Cu, Zn, Sn, and P) were obtained from commercial suppliers. Silicon (98.5%), zinc (≥99%, powder), and tin (≥99%) were obtained from Aldrich, and copper (in the form of CuCl, ≥99%) was obtained from Sigma–Aldrich. Phosphorus was added as CuP (99.999%), and was purchased from American Elements. We based the % weight compositions of the Cu and promoters associated with the contact masses on prior studies detailed in the literature [5, 18]. Specifically, the composition of the different contact masses used in the current study were (1) unpromoted, 10% Cu; (2) Zn–Sn-promoted, 10% Cu, 0.06% Zn, and 0.004% Sn; (3) Zn–P-promoted, 10% Cu, 0.06% Zn, and 0.02% P; (4) Sn–P-promoted, 10% Cu, 0.004% Sn, and 0.02% P; (5) Zn–Sn–P-promoted, 10% Cu, 0.06% Zn, 0.004% Sn, and 0.02% P. All the contact masses were made by mechanically mixing the relevant components. After the mixing the contact masses were stored in hexane.

Similar to our prior study the experimental setup consisted of an ATR-FTIR cell in line with a flow reactor. A schematic of this configuration is presented in a prior publication [3]. Before each experiment about 50 mg of a particular contact mass of interest was placed on a diamond ATR-FTIR element that was enclosed by a stainless steel reaction cell with ports to flow a gas of interest across the contact mass. The diamond element was part of a Specac Supercritical GoldenGate^{TM} ATR FTIR accessory that was mounted in a Thermo Electron Magna 560 infrared spectrometer. The cell was placed in line with a fixed bed stainless steel reactor that contained 1.5 g of the same contact mass that was present in the ATR reaction cell. During an experiment the reactor and the ATR-FTIR cell were heated to 300 ^{o}C. The cell and reactor were connected by Teflon (DuPont^{TM}) tubing. The effluent of the flow reactor was analyzed by gas chromatography (HP 5890 with a silica column and thermal conductivity detector) as a function of reaction time. The sensitivity of the thermal conductivity detector for the different products was determined by passing known amounts of pure methylchlorosilanes through the gas chromatograph (GC). Peak Simple software (SRI Instruments) was used to integrate the different GC peak areas. The same experimental methodology used in our prior study [3] was used in the current study. Briefly, the contact mass of interest on the diamond element and in the flow reactor was heated in a 0.1 standard cubic feet per hour flow of ultra high purity argon (99.997%, Air Products) at a temperature of 300 ^{o}C. A moisture trap was placed inline to ensure a moisture free environment (Vici Moisture Trap, T100-2). Typically, the Ar flow lasted for 2–3 h. This extended heating in Ar led to a temperature equilibration of the infrared optics and contact mass and led to reproducible infrared spectra over this period of time. After this

thermal stability was achieved, a final infrared spectrum in Ar was obtained, the Ar flow was turned off and MeCl (Matheson Tri Gas) was flowed through the experimental system while maintaining 300 ^{o}C flow conditions. The last infrared spectrum taken in the Ar flow was used as the reference spectrum for the infrared data obtained in situ under the MeCl flow. Sampling of the effluent of the flow reactor by GC was carried out approximately every 15 min during the DS reaction.

The same equations used in our prior study to calculate MeCl conversion, product selectivity, and Si conversion were used in the current study [3]. They are as follows:

$$MeCl\ conversion\ (\%) = \frac{moles\ silane}{moles\ silane + moles\ MeCl} x\ 100 \quad (4.1)$$

$$Selectivity\ (\%) = \frac{moles\ silane_x}{\sum moles\ silane} x\ 100 \quad (4.2)$$

$$-\frac{\Delta mass}{h} = \frac{moles\ Si_{final} - moles\ Si_{initial}}{moles\ Si_{initial}\ \mathrm{x}\ reaction\ time} \quad (4.3)$$

4.4 RESULTS AND DISCUSSION

4.4.1 PROMOTER EFFECTS ON SELECTIVITY, MeCl CONVERSION AND Si CONVERSION

Figure 4.1 displays the selectivity of four multiply promoted contact masses along with an unpromoted contact mass for five methylchlorosilane products; DMDCS, dichloromethylsilane (DCMS), trichloromethylsilane (TCMS), chlorodimethylsilane (CDMS), and chlorotrimethylsilane (CTMS). It is useful to first analyze the selectivity of the unpromoted contact mass as a comparison to the promoted contact masses. Without Zn, Sn, or P promotion, the copper–silicon contact mass shows an induction period of

just over 2 h, after which time a maximum selectivity toward DMDCS of 33% is achieved. All three doubly promoted contact masses show a higher selectivity toward DMDCS after 4 h of reaction where the Zn–Sn-, Zn–P-, and Sn–P promoted contact masses exhibit selectivities of 65, 62, and 58%, respectively. Analysis of the DMDCS plot also suggests that the contact masses that contain P do not show a significant induction period between the time of MeCl introduction (0 h) and the time at which maximum selectivity for DMDCS is obtained. In contrast, the Zn–Sn and unpromoted catalysts take close to 3 h to reach their maximum selectivity for DMDCS. While speculative, the presence of multiply promoted contact masses containing P appears to facilitate the alloying reactions between Cu and Si that establish a stable working surface. This issue will be discussed more later. Interestingly a prior study in our laboratory showed that a contact mass singly promoted with P (i.e. without zinc and or tin present) had a maximum selectivity for DCMS (low selectivity toward DMDCS) during the course of a 6 h run [3]. An investigation of the composition of the working catalyst with in situ ATR-FTIR suggested that while this surface accommodated a high concentration of CH_3 surface groups the P promotion also increased the amount of surface CH_3 fragmentation on the working surface [3]. Hence, an inference that can be made in view of this prior work is that the presence of Zn- or Sn on a P-promoted surface appears to ‘‘push’’ the selectivity back toward DMDC.

We believe that one of the more dramatic experimental observations with regard to product selectivities is associated with the triply (Zn–Sn–P) promoted contact mass. The Zn–Sn–P-promoted contact mass shows an initial selectivity (no induction period) toward DMDCS of 65%, but this selectivity drops off continuously over the next 5.25 h

of reaction at which point the selectivity for this product is 29%. The loss of selectivity for DMDCS is mirrored by a continuous increase in the selectivity of the contact mass for DCMS and TCMS. After 5.75 h, this contact mass shows the highest selectivity for DCMS (38%) and TCMS (26%) of any of the contact masses. We will return to offer a reason for this change in selectivity later after in situ ATR-FTIR results are presented below. Figure 4.2 displays the MeCl conversion (i.e., mole fraction of silane in the effluent) as a function of time for the different promoted contact masses. First, all of the promoted contact masses show a higher mole fraction of silane in the effluent from the flow reactor than does the unpromoted contact mass. Second, the MeCl conversion associated with the Zn–Sn–P-promoted catalyst shows a decreasing conversion with time that parallels its loss in selectivity toward DMDCS mentioned above. Hence, not only is the Zn–Sn–P-promoted catalyst losing its selectivity toward DMDCS, it is also making less methylchlorosilane product over the 5.75 h run. However, even after the 5.75 h run, this catalyst package has a greater MeCl conversion than the Zn–P- and Sn–P- promoted or unpromoted contact masses at the end of their respective runs. The Zn–P promoted catalyst is second to the Zn–Sn–P- promoted catalyst in terms of total MeCl conversion, although we do not have data for this contact mass beyond 4.3 h. This promoted contact mass, shows an increasing MeCl conversion up to about 2 h of reaction where it achieves a MeCl conversion of 13%. Over 4 h of the DS reaction the MeCl conversion of this promoted contact mass is greater than with the Sn–P-promoted, Zn–Sn-promoted, or unpromoted contact masses.

The MeCl conversion data is consistent with the Si conversion data shown in Figure 4.3. In these experiments, the difference in the mass of the particular contact mass

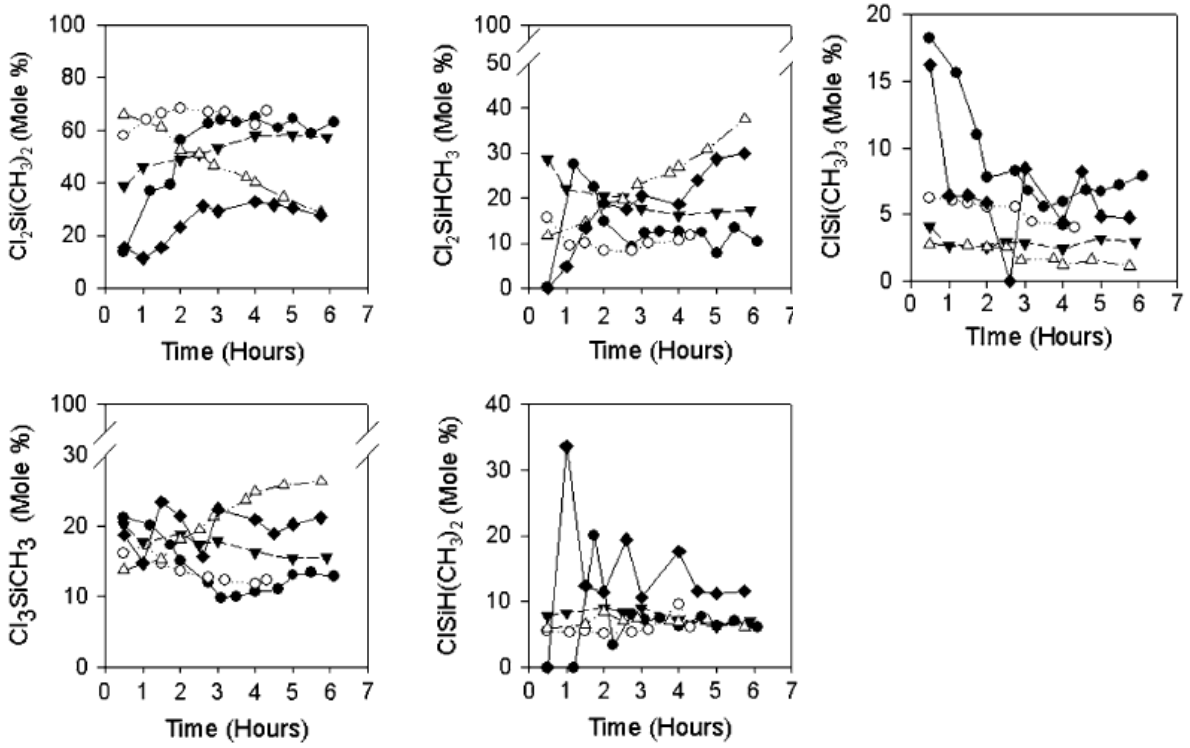

Figure 4.1: The selectivities for DMDCS [$Cl_2Si(CH_3)_2$], DCMS [Cl_2SiHCH_3], TCMS [Cl_3SiCH_3], CDMS [$ClSiH(CH_3)_2$], CTMS [$ClSi(CH_3)_3$] plotted as a function of time for Cu–Si contact masses promoted with Zn–Sn (filled circle), Zn–P(open circles), Sn–P (inverted triangle), and Zn–Sn–P (white triangle). Also shown are the product selectivities associated with an unpromoted (black diamond) contact masses.

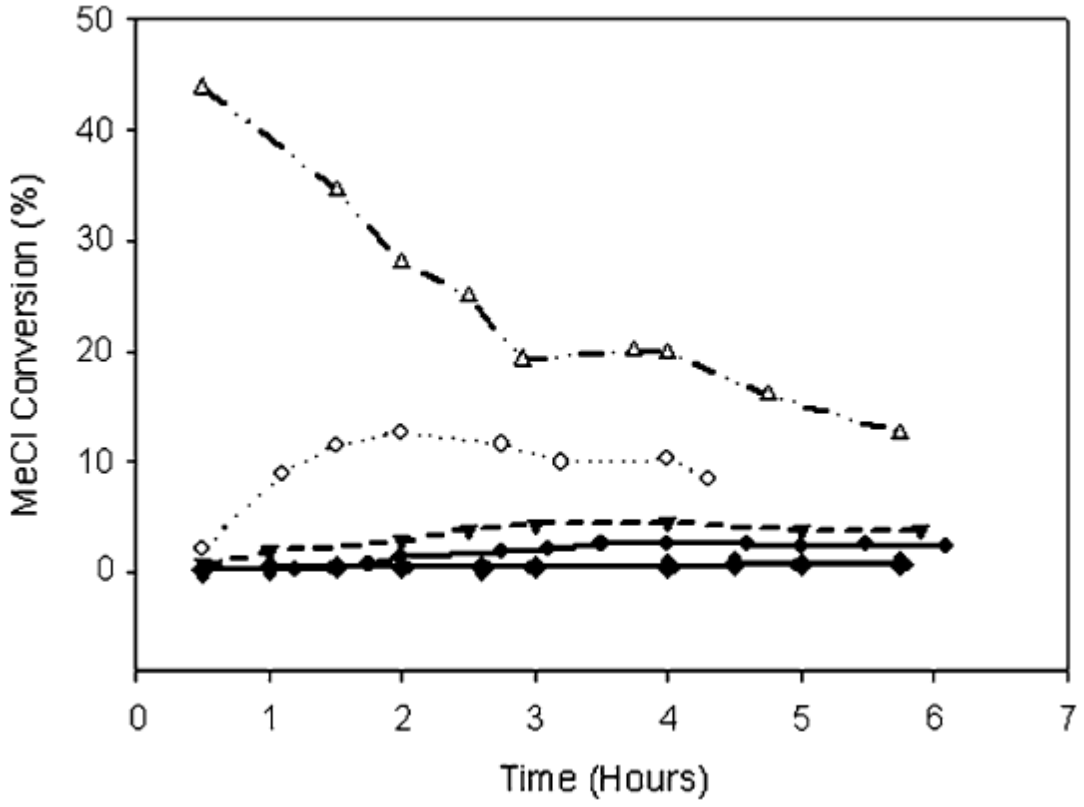

Figure 4.2: MeCl conversion as a function of time are shown for the Zn–Sn (filled circle), Zn–P (open circle), Sn–P (inverted triangle) and Zn–Sn–P (white triangle) promoted contact masses. Also shown is the MeCl conversion for an unpromoted Cu–Si (black diamond) contact masses.

over its entire reaction time divided by reaction time was used to estimate the rate of Si removal as gaseous product from the contact mass. The Si conversion rates vary from greatest to least in the order Zn–Sn–P-promoted <Zn–P-promoted <Sn–P- promoted <Zn–Sn- promoted <unpromoted contact mass. Consistent with the highest MeCl conversion of the Zn–Sn–P-promoted contact mass, the Si conversion rate associated with this contact mass is about a factor of two greater than the best performing doubly promoted contact mass (i.e., Zn–P-promoted).

4.4.2 IN SITU IDENTIFICATION OF SURFACE INTERMEDIATES ON THE DS CONTACT MASS

In an attempt to establish a more detailed understanding of the composition of the working surfaces of the different contact masses, in situ ATR-FTIR was employed to complement the reaction data above. Figure 4.4 exhibits data for the C–H stretching region associated with the different contact masses as a function of reaction time. All the promoted and unpromoted contact mass data sets (Figure 4.4, a–e) exhibit vibrational modes that have in prior work of the DS catalyst been assigned to surface CH_3 groups and / or CH_x (x=1,2) fragments [3]. Based on prior studies of surface CH_3 on silicon we assign the modes associated with the Zn–Sn-, Zn–P-, Sn–P- promoted, and unpromoted contact masses at 3000–2969 and 2954–2927 cm^{-1} to the $\upsilon_{as}(CH_3)$ and υ_s (CH_3) modes of surface CH_3 on Si, respectively [3, 19, 20]. Modes observed at lower wavenumbers than these modes are assigned to decomposition fragments of CH_3 (i.e., CH_x ; where x=1,2) (see Table 4.1) [3, 19]. In contrast to the doubly promoted and unpromoted systems, the triply promoted contact mass exhibits modes at 2937 and 2910 cm^{-1} that is not likely

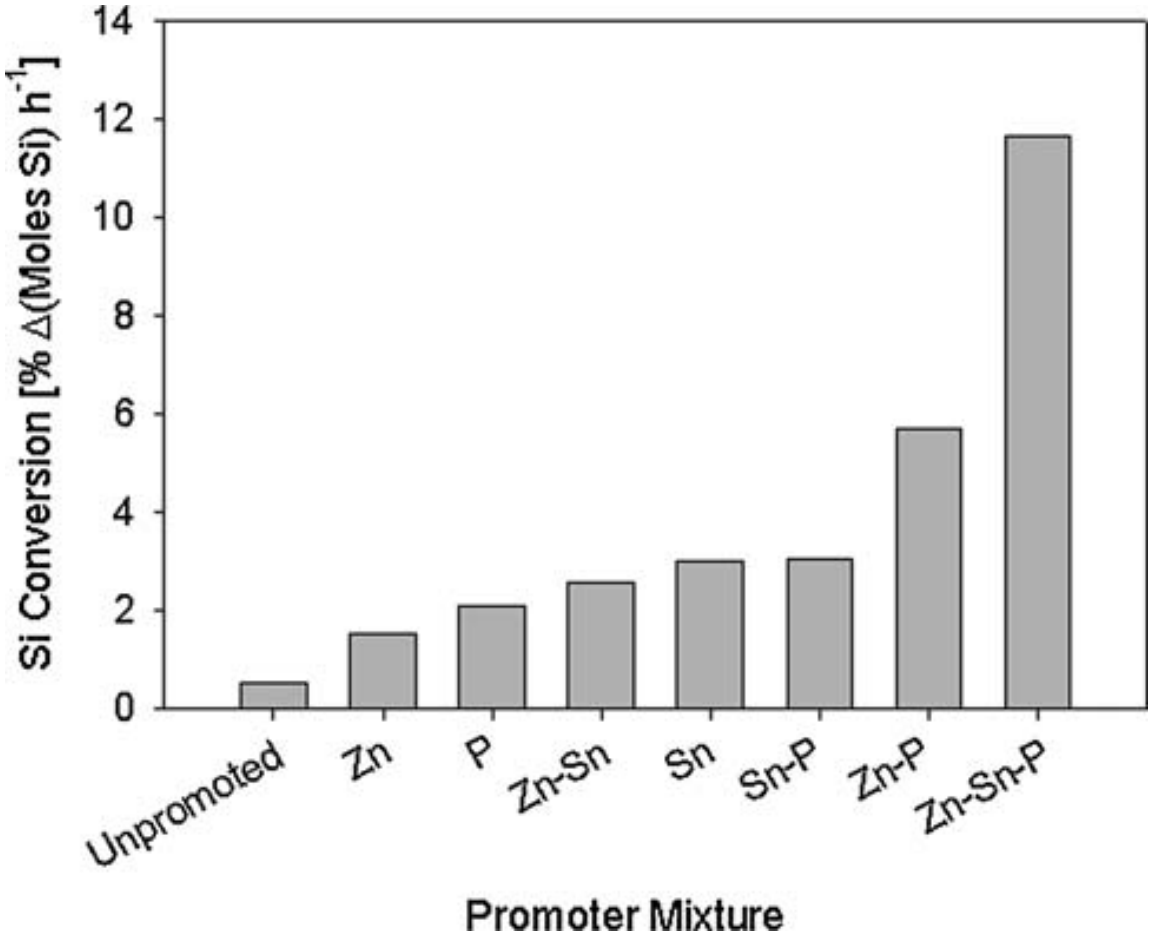

Figure 4.3: Silicon conversion data for the unpromoted, individually promoted contact masses (Zn, Sn, and P), doubly promoted contact masses (Zn–Sn, Zn–P, and Sn–P) and triply promoted contact mass (Zn–Sn–P). Additionally, individually promoted samples are also shown from previous investigations on singly promoted contact masses [3].

associated with the υ_{as} (CH_3) and υ_s (CH_3) modes of surface CH_3 on Si. A possible assignment for these modes will be discussed later. At least two aspects of the data in Figure 4.4 deserve further highlighting. First, all the promoted contact masses exhibit C–H stretch absorbances that are considerably higher (about a factor of 10) than the unpromoted contact mass after 4 h of reaction (note the absorbance scale). Hence, the promoted contact masses accommodate a higher concentration of surface CH_3 and fragments thereof under the DS conditions than can the surface of the unpromoted contact mass. We suspect that the rate of dissociative chemisorptions of MeCl is increased on the multiply promoted surfaces, considering that the Si conversion rates are much greater on the promoted contact masses and the surface concentration of surface CH_3 is relatively low on the unpromoted surface. Second, it is important to point out that an increasing concentration of surface CH_3 (and CH_3 decomposition fragments) does not necessarily correspond to an increase in MeCl conversion or Si conversion. Perhaps the most striking support for this contention is that the Zn–Sn–P promoted catalyst shows the lowest concentration of surface CH_3 after 0.5 h of reaction, even though its selectivity toward DMDCS is 65% and its MeCl and Si conversions are higher than any other contact mass formulation. We must conclude from this experimental observation that the turnover of surface CH_3 groups to methylchlorosilane product is occurring at a rate that is similar to the rate of MeCl dissociative chemisorption on the triply promoted surface. The Zn–Sn–P-promoted catalyst is then unique in that the Si active site is ‘‘primed’’ for reaction to form methylchlorosilanes. It is mentioned that the unpromoted catalyst also shows a low CH_3 surface concentration, although in this circumstance we believe that the relatively low rate of dissociative chemisorption of MeCl is the reason for the low

hydrocarbon fragment concentration. Also, of note from the data is that the continuous drop off in MeCl conversion for the Zn–Sn–P- promoted catalyst occurs concurrently with an increase in surface CH_3 and / or fragment thereof. It is not entirely obvious in this instance whether surface CH_3 or CH_x (x=1,2) is the species that grows over time (see Figure 4.4, d). If surface CH_3 bound to Si is increasing, then the frequencies of its vibrational modes are significantly red-shifted from the four other contact masses. We instead favor an alternative interpretation of the vibrational data. We suggest that the absorbances at 2937 and 2910 cm^{-1} that appear in the 2 and 4 h spectra for the Zn–Sn–P-promoted contact mass are associated with the υ_{as} (CH_3) and υ_s (CH_3) modes of surface CH_3 on the Cu component of the working catalytic surface. The positions of the modes are in excellent agreement with prior studies that have investigated the adsorption of CH_3 on Cu [21]. A weak mode is present as a shoulder near 2980 cm^{-1} that we suspect is due to surface CH_3 on the Si component [i.e., υ_{as} (CH_3)]. This interpretation leads to a possible scenario where the MeCl conversion for the Zn–Sn–P-promoted catalyst is initially greater due to the rapid removal of surface Si (consistent with the weak mode for surface methyl on Si) forming a copper rich contact mass surface. As the initial Si is depleted at the surface the reaction rate then becomes limited to some extent by the diffusion kinetics of Si to the copper rich contact mass surface. The formation of a more copper rich surface may also play a role in the change in selectivity of the Zn–Sn–P-promoted surface. The Zn–Sn–P-promoted data also exhibit the increase in modes over the DS reaction that are likely due to CH_x (x=1,2) and this is consistent with the change

Table 4.1: Summary of assignments based on ATR-FTIR data (units are cm^{-1}).

Surface Species	Unpromoted[c]	Zn-Sn	Sn-P	Zn-P	Zn-Sn-P
$\nu_{as}(CH_3)$	3000	2983	2969	2981	2937
$\nu_s(CH_3)$	2954	2944	2927	2945	2910
$\nu_{as}(CH_2)$	-	-	2861	2834	2845
ν_{as}(Si-O-Si)	1193	1200	1197	1209	1211
ν_s(Si-O-Si)	1051	1055	1048	1055	1047
$\rho(CH_3)$	1276	1273	1277	1277	1279
$\delta(CH_3)$[a]	~1205	~1205	~1205	~1205	~1205
ν_{as}(Si-O)	1120	1125	1142	1146	1130
ν(C-O)[b]	-	1084	-	-	-
$\tau(CH_2)$	-	-	1010	-	-
ν_s(Si-O)	1004	1018	996	1004	1012
$\delta(O_3Si-H)$	~900	-	904	915	910
ν(Si-O)[b]	-	937	-	-	-
δ(Si-H)	~820	817	836	830	830
ν_{as}(Si-O)	1120	1125	1142	1146	1130
ν(C-O)[b]	-	1084	-	-	-
$\tau(CH_2)$	-	-	1010	-	-

[a]Obscured by υ_{as}(Si-O-Si) and is not labeled in figures
[b]Resulting from methoxy absorbances
[c]Adapted from results of prior investigations [3].

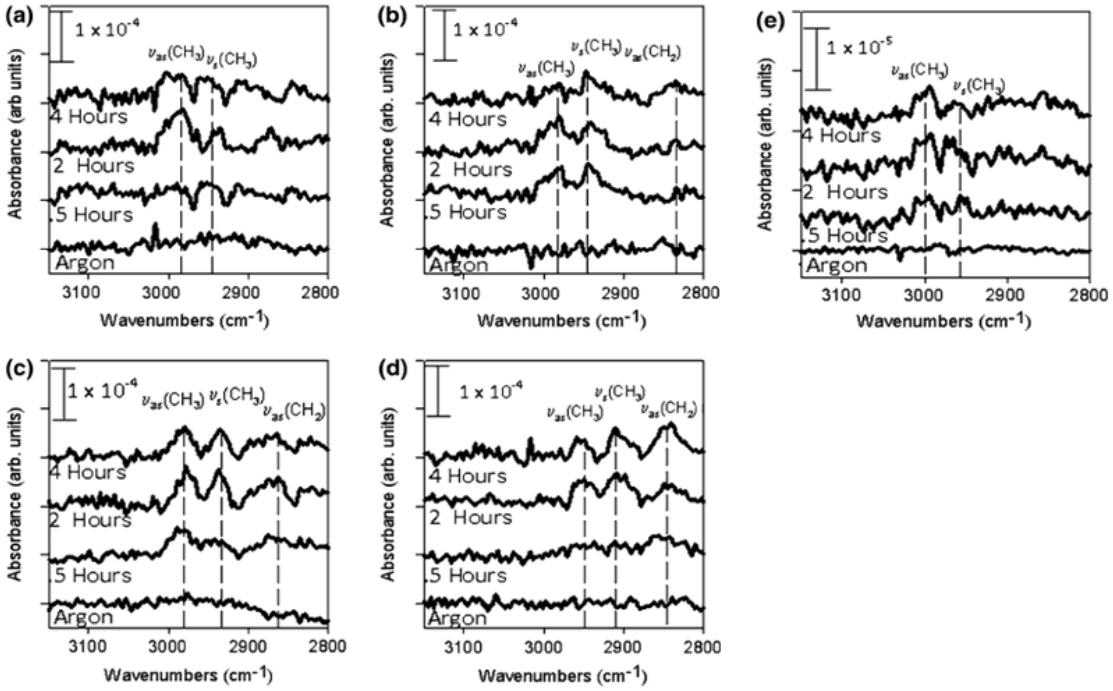

Figure 4.4: ATR–FTIR of the CH stretching region of (a) Zn–Sn-promoted, (b) Zn–P-promoted, (c) Sn–P-promoted, (d) Zn–Sn–P-promoted and (e) unpromoted contact masses. All the spectra were obtained in situ at 1 bar MeCl at 300 ^{o}C. The time the spectrum was obtained after MeCl introduction is indicated in the figure. The spectrum labeled ‘‘argon’’ was obtained just before flowing argon was replaced by MeCl.

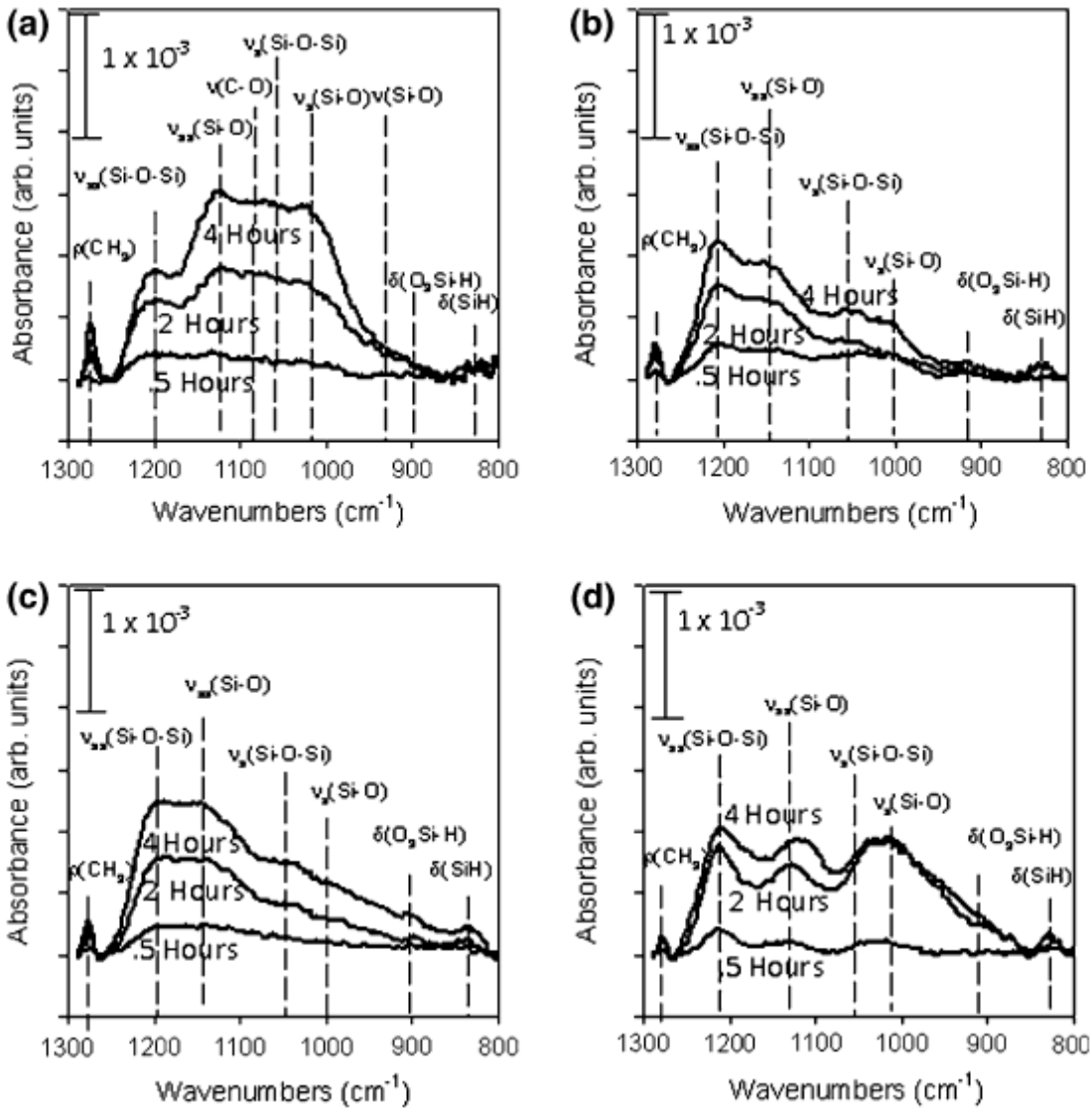

Figure 4.5: The 800–1300 cm^{-1} spectral region for (a) Zn–Sn-promoted, (b) Zn–P-promoted, (c) Sn–P-promoted, and (d) Zn–Sn–P-promoted contact masses. All spectra were obtained in situ at 1 bar MeCl at 300 ^{o}C. The time the spectrum was obtained after MeCl introduction is indicated in the figure.

in selectivity of this contact mass from DMDCS to the less methylated DCMS species. Figure 4.5 exhibits in situ infrared results for the 800–1300 cm^{-1} range taken at the same time as the respective spectra that are exhibited in Figure 4.4. Similar to our conclusion in prior work that investigated the individual promoters on the DS [3], this mid-IR region is dominated by features that are attributable to Si–O derived modes, in addition to modes that we attribute to CH_3 groups bound to Si (1276 cm^{-1}) and to Si–H bonds (836–817 cm^{-1}) [22]. We also suspect that surface methoxide (i.e., Si–O–CH_3) contributes to the spectra of certain catalyst packages. Specifically, we attribute the 1084 cm^{-1} mode exhibited in the Zn–Sn-promoted contact mass spectrum to this species. Prior work has suggested that tin may encourage CH_3 spillover onto Si–O sites, thereby forming a stable surface methoxide [3]. We mention, however, that this region is congested with vibrational modes and we cannot rule out significant Si–O mode contributions to this specific absorbance. Our explanation for the growth of the Si–O derived modes, similar to the one put forward in our earlier study, is that residual amounts of oxygen in the gas stream oxidize the Si that is part of the Si–Cu alloy at 300 ^{o}C. Control experiments carried out in our laboratory show no detectable growth of Si–O modes if pure Si powder is treated with MeCl at 300 ^{o}C. We do not find the reactivity of the Si–Cu toward residual oxygen surprising based on prior studies that show the Si in the Si–Cu alloy (e.g., Cu_3Si) is more susceptible to oxidation than is pure silicon [23]. We do not suspect that this residual oxidation affects our results considering that our selectivities and relative reaction rates derived from the reactor studies agree well with prior studies [5–9].

Consistent with the presence of decomposition fragments of surface CH_3 on the multiply promoted surfaces, are the modes attributable to the δ(SiH) mode of Si–H

surface species. These modes show growth over at least 4 h of reaction time. While the comparison of the intensity of modes between catalyst formulations is somewhat problematic, the 1276 cm^{-1} mode attributable to surface CH_3 on Si appears to be most attenuated on the triply promoted catalyst, consistent with the C–H stretching region that shows little evidence for surface CH_3 bound to Si. Instead the C–H stretching region shows that surface CH_3 is predominately bound to the Cu component. Both of these possibilities would result in the attenuated intensity of the $\rho(CH_3)$ mode at 1276 cm^{-1}. Based on prior work of CH_3 on copper the $\delta(CH_3)$ mode for surface CH_3 on copper would appear at 927 cm^{-1} [21]. The triply promoted catalyst does show significant spectral weight in this region, but any specific assignment to the $\upsilon(CH_3)$ mode of CH_3 on copper in this region would be dubious due to the strong contribution from Si–O modes. We feel that the C–H stretching region offers more direct evidence of CH_3 on copper due to our ability to resolve the relevant modes.

4.4.3 COMPARISON OF INDIVIDUALLY PROMOTED TO MULTIPLE PROMOTED CONTACT MASSES FOR THE DS

It is useful at this point to discuss our results of the multiply promoted DS contact masses in view of our prior studies of the individually promoted contact masses [3]. A relevant experimental observation made in our prior study of individually promoted contact masses for the DS was that the individual promotion of copper–silicon contact mass with either P or Sn led to an increase in the concentration of surface CH_3 compared to Zn-promoted and unpromoted contact masses. In the P-promoted circumstance, however, a significant amount of fragmentation of the surface CH_3 was observed whereas in the Sn case, only surface CH_3 was experimentally observed. Another important

difference between the individual P and Sn promotion was that the latter promoter led to a high selectivity for DMDCS (as did Zn promoter) while the former had a high selectivity for DCMS, consistent with CH_3 fragmentation. Our current results show that if both Sn and P are present, there is still CH_3 fragmentation, but the selectivity of the Sn–P-promoted contact mass shows a high selectivity for DMDCS, and the rate of Si conversion is close to the value obtained for contact mass that had been promoted with only Sn. The MeCl conversion, which is essentially a measure of the mole fraction of silane in the effluent, however, is significantly lower than if Sn is present alone. We suspect that this comparison suggests that the presence of P leads to significant fragmentation of surface CH_3 on the Sn–P promoted surface that inhibits methylchlorosilane product formation, presumably by blocking active sites. Of the doubly promoted contact masses, the Zn–P-promoted surface exhibits the greatest Si and MeCl conversion.

Prior research showed that Zn promotion led to high selectivity toward DMDCS, but had a low Si and MeCl conversion rate in addition to a low steady state concentration of surface CH_3 [3]. With the addition of P, both the MeCl and Si conversion show significant increases with little loss in selectivity for DMDCS. Prior studies have suggested that the promoter action of Zn leads to an increase of the rate of diffusion of Si through copper making it available for methylchlorosilane product formation [24]. It is reasonable that the presence of P increases the amount of surface CH_3 on the Zn–P-promoted contact mass and the Zn facilitates the availability of active Si for its removal as methylchlorosilane product. Prior research by Lewis and Ward has also suggested that P-promotion enhanced the formation of the Cu_3Si phase (i.e., eta-phase [6]) that is

thought to be an active phase for DMDCS production [25]. This prior research suggested that P-promotion facilitates copper diffusion away from the working surface preventing the formation of copper rich phases such as Cu_5Si and free copper. Such a promoter action by P may be the reason for our experimental observation that P-promoted contact masses showed no significant induction period for the production of DMDCS. In contrast, the Zn–Sn-promoted contact mass shows a ~3 h induction period until its selectivity for DMDCS reaches a maximum, suggesting that in the absence of P, the formation of the Cu_3Si phase is kinetically hindered.

The triply promoted catalyst shows the highest Si and MeCl conversion for 6 h of reaction. Of all the catalyst formulations this promoted contact mass shows a behavior that is unique relative to any of the other doubly or singly promoted contact mass. As already elaborated on above, the low surface CH_3 concentration while the MeCl conversion is as high as 44% suggests that the Sn and P facilitate the deposition of surface CH_3 from MeCl, and the Zn (perhaps cooperatively with P) effectively provides available surface silicon so that the production rate of methylchlorosilanes is not limited by silicon availability.

Over the course of the DS, the selectivity for DMDCS decreases below that of the doubly promoted catalyst. We suspect that this is a result of the change in the composition of the triply promoted catalyst over time where the surface becomes more copper rich. This is an interesting point, since as mentioned above P has been shown in prior research to prevent the formation of the copper rich contact mass that is deemed detrimental to the production of DMDCS [6]. Under our experimental conditions, however, it seems as though as the DS reaction proceeds the ability to form the Cu_3Si

phase on the triply promoted contact mass becomes compromised. The increase in the concentration of CH_3 surface species bound to the Cu component may interfere in the alloying between Cu and Si, hindering the formation of active Cu_3Si phases during the DS. Unfortunately, whether the formation of the copper rich surface is due to a decrease in Si diffusion to the surface or to a decreasing ability of P to increase Cu diffusion over time cannot be ascertained from our experimental studies.

We close by adding that while we believe that are arguments given above are consistent with our experimental observations, there are likely subtle changes in the structure of the active phase and / or active sites with P promotion (or any of the promoters) that will not be detectable by in situ infrared spectroscopy. Future experiments are required to investigate possible structural changes of the copper–silicon phases with and without promoter. Such studies would advance our understanding of the promoter effects on the DS and would complement the experimental observations detailed in this chapter.

4.5 SUMMARY

Contact masses associated with the synthesis of methylchlorosilanes from MeCl promoted with Zn–Sn, Zn–P, Sn–P, and Zn–Sn–P have been investigated with in situ infrared spectroscopy and flow reactor studies. Each of the doubly promoted catalysts shows a high selectivity for DMDCS after 3 h of reaction with MeCl. The selectivity of a P-singly promoted catalyst has its highest selectivity for DCMS, and the addition of Zn or Sn shifts the selectivity toward DMDCS. Of the doubly promoted systems, the presence of Zn–P leads to the highest Si and MeCl conversion.

The triply promoted catalyst shows a Si and MeCl conversion that is significantly greater than the Zn–P contact mass, but after 6 h or reaction its MeCl becomes similar to

the doubly promoted Zn–P catalyst. The triply promoted catalyst also shows a decrease in selectivity for DMDCS from 65% at 0.5 h reaction time to 29% at 5.75 h reaction time. Experimental observations suggest that the drop in MeCl conversion and selectivity is due to the rapid depletion of Si from the outer-most surface. The reaction rate of this contact mass is then limited by the diffusion kinetics of silicon through a copper rich surface. In situ infrared spectroscopy suggests that surface CH_3 shows appreciable binding to the copper component of the contact mass in contrast to the other catalyst formulations where only surface CH_3 on silicon is observed. This result is consistent with a depletion of silicon from the triply promoted surface making the surface effectively more rich in copper.

References

[1] Rochow, E.G., *Journal of the American Chemical Society* 67 (1945) 963–965.

[2] Frank, T.C., Kester, K.B., Falconer, J.L., *Journal of Catalysis* 91 (1985)

[3] Gordon, A.D., Hinch, B.J., Strongin, D.R., *Journal of Catalysis* 266 (2009) 291-298

[4] Kim, J.P., Rethwisch, D.G., *Journal of Catalysis* 134 (1992)

[5] Lewis, L.N., *Chemistry of Organic Silicon Compounds* 2 (1998) 1581–1597.

[6] Lewis, L.N., Ward, W.J., *Industrial and Engineering Chemistry Research* 41 (2002)

[7] Ehrich, H., Born, D., Richter, K., Richter-Mendau, J., Lieske, H., *Applied Organometallic Chemistry* 11 (1997)

[8] Wessel, T.J., Rethwisch, D.G., *Reaction Kinetics and Catalysis Letters* 58 (1996)

[9] Voorhoeve, R.J.H. (1967) *Organohalosilanes: Precursors of Silicones Elsevier*, Amsterdam

[10] Gasper-Galvin, L.D., Rethwisch, D.G., Sevenich, D.M., Friedrich, H.B., *Studies in Organic Chemistry* (Amsterdam) 49 (1993) 279–297.

[11] Floquet, N., Yilmaz, S. Falconer, J.L., *Journal of Catalysis* 148 (1994)

[12] Gheyas, S.I., Strable, B.L., Strongin, D.R., Wright, A.P., *Surface Science* 474 (2001)

[13] Zhang, X.V., Strongin, D.R., Goncharova, L.V., Ermakov, A.V., Hinch, B.J., *Journal of Physical Chemistry B* 108 (2004)

[14] Han, J., Gheyas, S.I., Wang, Y., Strongin, D.R., Hinch, B.J., Wright, A.P., *Langmuir* 16 (2000)

[15] Han, J., Gheyas, S.I., Wang, Y., Strongin, D.R., Graham, A.P., Hinch, B.J.,

Wright, A.P., *Journal of Physical Chemistry B* 104 (2000)

[16] Han, J., Gheyas, S.I., Strongin, D.R., Hinch, D.R., Wright, A.P., *Catalysis Letters* 68 (2000)

[17] Luo, W., Wang, G., Wang, J., *Chemical Engineering Communications* 193 (2006)

[18] Lewis, K.M., Kanner, B., *Catalyzed Direct Reactions of Silicon*, Elsevier, Amsterdam, 1993.

[19] Colaianni, M.L., Chen, P.J., Gutleben, H., Yates Jr., J.T., *Chemical Physics Letters* 191 (1992)

[20] Kong, M.J., Lee, S.S., Lyubovitsky, J., Bent, S.F., *Chemical Physics Letters* 263 (1996)

[21] Zhai, R.S., Chan, Y.L., Chuang, P., Hsu, C.K., Mukherjee, M., Chuang, T.J., Klauser, R. *Langmuir* 20 (2004)

[22] Michalak, D.J., Amy, S.R., Esteve, A., Chabal, Y.J. *Journal of Physical Chemistry C* 112 (2008)

[23] Stolt, L., Charai, A., D'Heurle, F.M., Fryer, P.M., Harper, J.M.E., *Journal of Vacuum Science & Technology A: Vacuum, Surfaces and Films* 9 (1991)

[24] Potochnik, S.J., Falconer, J.L., *Journal of Catalysis* 147 (1994)

[25] Levin, L., Atzmon, Z., Katsman, A., Werber, T., *Materials Chemistry and Physics* 40 (1995)

CHAPTER 5

REDUCTION OF NITRITE AND NITRATE TO AMMONIA ON NANO-FeS_m UNDER ALKALINE CONDITIONS

5.1 OVERVIEW

The ability to produce fixed nitrogen is often cited as a critical juncture in prebiotic molecular development given that ammonia is required for the production of amino acids and other biological molecules. It has been proposed that ammonia formation, and other reactions may have been promoted by FeS in hydrothermal vent-like environments that may have existed at the interface of the acidic Hadean ocean and more alkaline subsurface water within the Hadean crust. These environments may have provided both the reducing power, as well as the surface necessary for the production of many of the raw prebiotic materials needed for biological systems. In this work, we show the possibility of significant ammonia production from oxidized nitrogen bearing compounds in basic aqueous solution that may have played a key role the formation of ammonia during the Hadean. Results from geochemical batch reactions in situ attenuated total reflection- Fourier transform infrared spectroscopy experiments will be presented that shed light on the mechanistic details associated with ammonia formation from nitrite and nitrate on the FeS surface.

5.2 INTRODUCTION

By definition, ammonia production was integral for the formation amino acids and proteins on the Hadean Earth if these molecules existed then just as they do today. During the Hadean Eon, Fe^{2+} - bearing iron sulfide mineral surfaces likely existed in and around aqueous environments and may have served as a substrate for ammonia

formation. This scenario provides a possible bridge between the iron-sulfur clusters observed within many present day enzymes (such as active sites present in nitrogenase and hydrogenase) and the mineral surfaces on which they may have evolved.

It has been hypothesized previously that the levels of ferrous iron (Fe^{2+}), sulfate (SO_4^{2-}), nitrite (NO_2^-) and nitrate (NO_3^-) in the early ocean were significant and relevant in the context of prebiotic chemistry [1-3]. Previous investigations have suggested that the reduction of nitrite and nitrate to NH_3 / NH_4^+ by aqueous Fe^{2+} may have been a key reaction for the fixation of nitrogen in prebiotic chemical environments [1,4]. Subsequent work also demonstrated that the ferrous iron bearing sulfide, FeS could facilitate the transformation of nitrite to ammonia [5]. Additional work in this area has shown that significant amounts of ammonia can be generated using a variety of Fe based surfaces including $Fe^0_{(s)}$ [6], $Fe^{2+}_{(aq)}$ [1], pyrite [7], pyrrhotite [8], basalt [8], and Fe_3O_4 [8]. Despite the myriad of previous work on this system there has been little molecular-level insight offered by prior studies that explains the mechanistic pathways associated with the reduction of nitrite and nitrate. Furthermore, previous work has examined this chemistry at slightly acidic conditions, even though alkaline environments may have existed during the Hadean [9-12].

In this chapter, research is presented that investigated nitrite and nitrate reduction to ammonia under reducing alkaline conditions, simulating the sub-hydrothermal vent environments in which Russell has proposed to have existed on early Earth. Specifically, Russell proposed that an FeS “protomembrane” existed in hydrothermal vent environments that acted as a cell membrane-like partition between the alkaline crust environment and the acidic Hadean ocean. This chapter investigates chemistry in an

alkaline FeS chemical environment (associated with Russell's theories) and examines the ability of this alkaline environment to support ammonia production from the reduction of nitrite and nitrate. Specifically, the current investigation investigated both the kinetics and surface bound intermediates associated with the reduction of nitrite and nitrate to ammonia at 22 ^{o}C, 70 ^{o}C and 120 ^{o}C. Research presented here will show, using geochemical kinetic batch reactions in parallel with in situ ATR-FTIR experiments that increasing the temperature to 120 ^{o}C results in an enhancement of the kinetics of ammonia formation from both nitrite and nitrate on FeS. Results from ATR-FTIR spectra are presented and provide molecular-level insight into the mechanistic details associated with FeS surface based reduction of nitrite and nitrate. Finally, interpretation of these results and the significance that both reactions have with regard to mineral based organic synthesis and the origin of life on Earth will be presented.

5.3 EXPERIMENTAL METHODS

5.3.1 NANO-FeS_m AND REAGENT PREPARATION

Nanosized iron sulfide (FeS) for this study was prepared by the aqueous reaction of ferrous iron (Fe^{2+}) with sulfide (S^{2-}) [13, 14]. In brief, 1M solutions of $FeSO_4$ and $Na_2S.9H_2O$ (ACS reagent grade, used without further purification) were prepared at room temperature with freshly drawn Ar-sparged, O_2-free deionized water (18.2 MΩ) inside an anaerobic glovebox (95% N_2 / 5% H_2). The Fe^{2+} containing solution was then injected into the sulfide solution, resulting in the rapid precipitation of FeS. The resulting black precipitate was centrifuged down, the supernatant was discarded and replaced with 1 mM $Na_2S.9H_2O$ solution. This "washing" process was repeated three times and was designed to remove residual SO_4^{2-}, Na^+ and unreacted Fe^{2+}. The particle loading was determined

using a Pyrex® Guy-Lussac bottle and confirmed by desiccating an aliquot of known volume / weight of the slurry under anaerobic conditions. The FeS slurry was stored in the glovebox (anaerobic environment) with constant O_2 monitoring (Coy Laboratory Products) and used as necessary in batch experiments. The slurry was stored in a protective 1 mM Na_2S solution in order to prevent any oxidation of the FeS due to long term storage. Stock nitrite and nitrate solutions were prepared by dissolving reagent-grade $NaNO_2$ or KNO_3 in Ar-purged, O_2-free deionized (DI) water (18.2 MΩ). Deionized water (18.2MΩ) used for making solutions was obtained from a nanopure water treatment system and bubbled with high purity argon gas for 2 h to remove any dissolved gases. All samples were prepared under anaerobic conditions in a glove box in an atmosphere of 95% argon / 5% H_2.

For the ATR-FTIR experiments, freshly precipitated FeS was generated within the glove bag which was equipped with an O_2 monitor (< 0.1 ppm). The FeS was generated using the same methodology as described above, after which 2 mL of the FeS slurry was combined with 2 mL of 10 mM nitrite or nitrate stock solutions yielding 5 mM solution, in nitrite or nitrate, and FeS particle loadings of 7.5 g / L. These slurries were produced and injected into the ATR or batch reactor (ATR or batch) cell immediately prior to the start of the experimental run.

5.3.2 BATCH EXPERIMENTS

Nitrite / FeS or nitrate / FeS slurry was loaded into 6 mL PEEK and Teflon® - lined stainless steel reactors in an anaerobic atmosphere. Loaded and sealed reactors were then placed in a temperature controlled oven on an orbital shaker and agitated at ~150 rpm. Experiments were conducted at room temperature (22 ºC), 70 ºC, and 120 ºC.

Individual reactors were withdrawn at desired time intervals, filtered using a 10,000 and 3500 Dalton filter and either immediately analyzed or frozen until analysis. Background levels and production of NH_4^+ were evaluated in a series of blank experiments at 70 ºC and 120 ºC to assess any reactivity of the reaction vessel and / or thermal degradation, as well as release of ammonia from the FeS used in the experiment.

5.4 ANALYTICAL METHODOLOGY

5.4.1 BATCH REACTION MEASUREMENTS

Nitrate and nitrite were analyzed on a Dionex DX500 ion chromatograph with a 4 mm IonPac® AS4A-SC anion column and a 1.7 / 1.8 mM $NaHCO_3$ / Na_2CO_3 eluent, respectively. Concentrations were calculated from a linear 4-point calibration curve with R^2 values above 0.99. Ammonium was analyzed using an adapted fluorescence method [15] on a Barnstead Quantech FM109515 fluorometer with 360 nm and 420 nm narrow band excitation and emission filters, respectively. Samples and standards with individual volumes of 175 µL were pipetted into polypropylene vials with 3 mL of working reagent and incubated in the dark for 24 - 48 h. Ammonium concentrations were calculated from a linear 9-point calibration curve with R^2 values above 0.99.

5.4.2 ATR-FTIR EXPERIMENTS

Two different ATR accessories were utilized, depending on the reaction temperature used for a particular experiment. The 22 ^oC and 70 ^oC experiments were conducted in a multibounce ATR accessory (Pike Technologies) with a Ge element, whereas the 120 ^oC experiments utilized a diamond single bounce ATR accessory (Specac) which was pressurized with 50 bar of ultra-high-purity argon to elevate the boiling point of H_2O. The accessories were individually mounted on a Nicolet Magna 750

FTIR spectrometer equipped with a liquid N_2 cooled MCTA detector. The Ge and diamond multibounce units were used to collect single beam spectra with a resolution of 4 cm^{-1} (2 min / spectrum). In either case, a spectrum was taken as soon as the reaction cell reached the desired experimental temperature (time 0) and this spectrum was used as a reference spectrum for all subsequent single-beam spectra.

5.5 RESULTS

The results section of this chapter will be divided into three sections. The first section will characterize the FeS phase used in this study. The second and third sections will describe results obtained from geochemical batch reactions and in situ ATR-FTIR results, respectively, on FeS in 5 mM nitrite or nitrate slurry at reaction temperatures of 22 ^oC, 70 ^oC and 120 ^oC.

5.5.1 BATCH REACTION RESULTS

Results from aqueous geochemical batch reaction studies are shown in Figures 5.1-5.3. Ammonia production resulting from FeS reacting with 5 mM nitrite (top) and nitrate (bottom) at 22 ^oC, 70 ^oC and 120 ^oC as a function of reaction time is shown in Figure 5.1. The concentration of ammonia generated by the 120 ^oC / FeS / nitrite system after 5 h of reaction time is more than 200 μmole/kg, while the 70 ^oC / FeS / nitrite and 22 ^oC / FeS / nitrite experiments generated 14 μmole/kg and ~3 μmole / kg ammonia, repectively. The latter amount associated with the 22 ^oC reaction temperature is equivalent to background levels generated in blank experiments where no nitrite is present. After 30 h nearly 1200 μmole / kg ammonia is generated by the 120 ^oC / FeS / nitrite and lower yields are generated in the 70 ^oC / FeS / nitrite system (85 μmole/kg) and 22 ^oC / FeS / nitrite system (~5 μmole / kg).

Figure 5.1 (bottom) shows ammonia production associated with FeS reacting with 5 mM nitrate at reaction temperatures of 22 ^{o}C, 70 ^{o}C and 120 ^{o}C. There is a substantial decrease in the amount of ammonia that forms from nitrate when compared to nitrite in the presence of FeS. The 22 ^{o}C / nitrate / FeS and 70 ^{o}C / FeS / nitrate experiments yielded ~ 3 μmole / kg and ~5 μmole / kg ammonia after 30 h of reaction time, respectively, while the 120 ^{o}C/FeS/nitrate experiment yielded ~30 μmole / kg of ammonia after 30 h (compared to 1200 μmole / kg when nitrite is the reactant). Figure 5.2 exhibits the aqueous nitrite concentration as a function of time resulting from the reaction of FeS with 5 mM nitrite at 22 ^{o}C (a), 70 ^{o}C (b) and 120 ^{o}C (c). All these data are associated with the same experimental runs as the ammonia measurements that were presented in Figure 5.1.

Based on Figure 5.2 the 120 ^{o}C / FeS / nitrite experiment shows less nitrite remaining (1.2 mmole / kg) than that of the 70 ^{o}C / FeS / nitrite experiment (3.5 mmole/kg) after 30 h. The 22 ^{o}C / FeS / nitrite experiments shows little change in nitrite concentration over the course of the experiment. There is little evidence of nitrate observed in solution in the nitrite experiments. Overall, the trend of nitrite consumption increasing with temperature is consistent with the yield of ammonia showing increasing with reaction temperature.

Figure 5.3 shows the nitrate concentration as a function of time for the 22 ^{o}C, 70 ^{o}C and 120 ^{o}C FeS / nitrate experiments. There is no discernable change in the nitrate concentration for any of the reactions. This experimental observation is not unexpected considering that the ammonia yield from the reaction of nitrate in the presence of FeS was limited at any of the reaction temperatures investigated in this study.

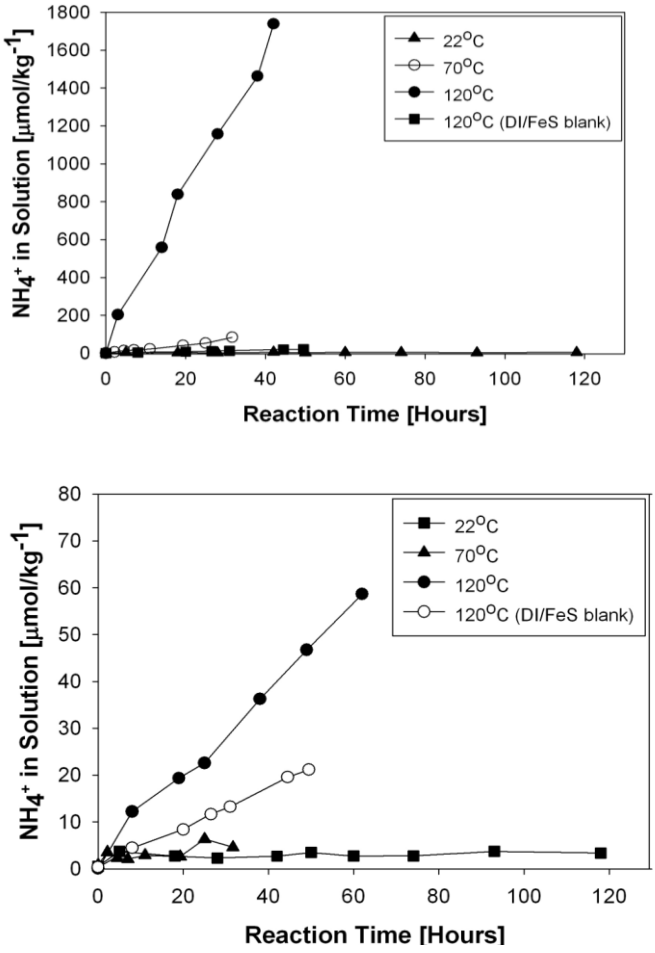

Figure 5.1: Ammonia yields resulting from nitrite and nitrate reduction on FeS_m as a function of time at 22 °C, 70 °C, and 120 °C. Top*:* The results of batch reaction measurements of ammonia generated by FeS and 5 mM nitrite at 22 °C (▲), 70 °C (○), and 120 °C (●) as a function of reaction time are shown. The 120 °C blank is shown for comparison (■). Bottom*:* The results of batch reaction measurements of ammonia generated by FeS and 5 mM nitrate at 22 °C (■), 70 °C (▲), and 120 °C (●) as a function of reaction time are shown. The 120 °C blank is shown for comparison (○).

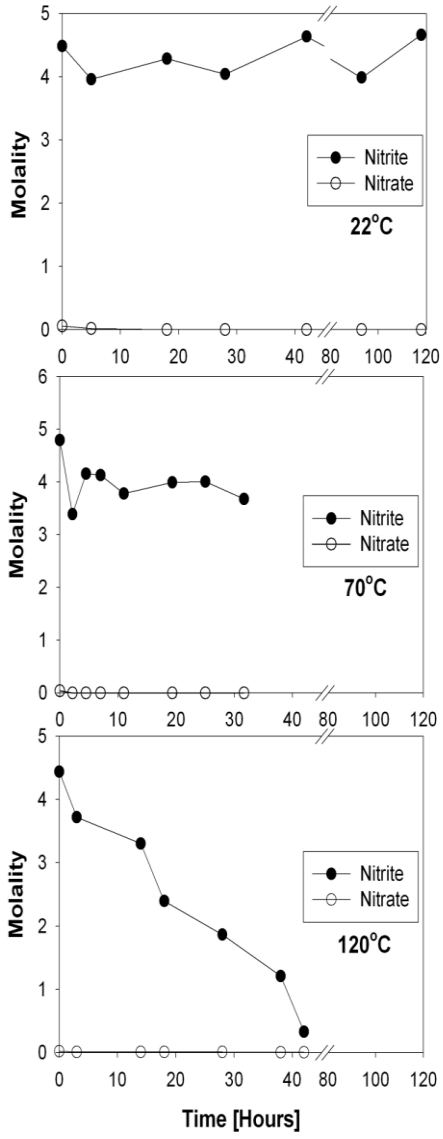

Figure 5.2: The nitrite (●) and nitrate (○) concentrations obtained from geochemical batch reaction measurements as a function of time conducted at 22 ^{o}C (top), 70 ^{o}C (middle) and 120 ^{o}C (bottom).

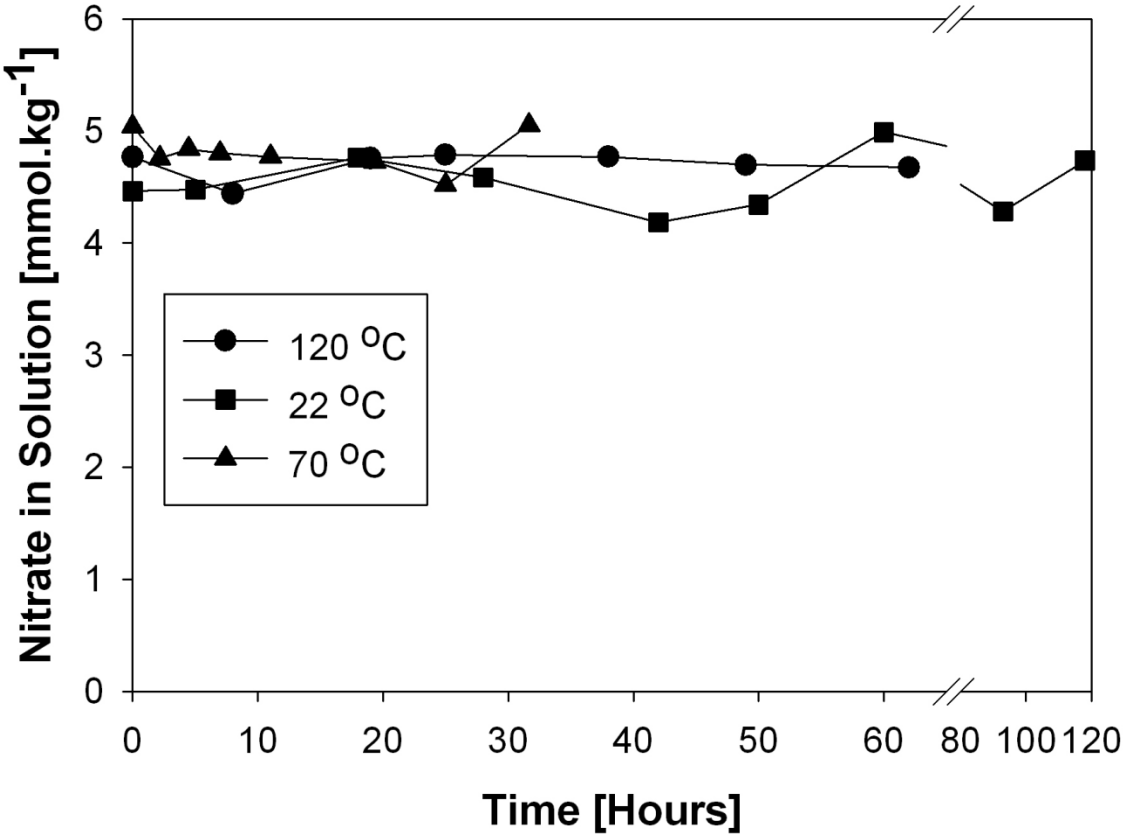

Figure 5.3: The results of batch reaction measurements starting with nitrate at 22 ^{o}C (■), 70 ^{o}C (▲), and 120 ^{o}C (●) as a function of reaction time.

5.5.2 ATR-FTIR RESULTS

Vibrational mode assignments in this chapter are made both in view of prior work on other iron-sulfur surfaces and on the basis of ammonia yields observed in geochemical batch reaction measurements discussed in the previous section [7, 16].

5.5.2.1 FeS EXPOSED TO 5 mM NITRITE AT 22 ^{o}C

Figure 5.4 (a-e) shows ATR FTIR spectra associated with freshly precipitated FeS that was exposed to 5 mM nitrite at a temperature of 22 ^{o}C after 5, 30, 60, 120, 180 minutes of reaction time. The two modes centered at 1747 cm^{-1} and 1777 cm^{-1} are assigned to the υ_{as} $(NO)_2$ and υ_{s} $(NO)_2$ modes, respectively, of the dinitrosyl group adsorbed on FeS. Initially, only the mode at 1747 cm^{-1} is observed, however, after two h the second mode at 1777 cm^{-1} is observed.

5.5.2.2 FeS EXPOSED TO 5 mM NITRITE AT 70 ^{o}C

Figure 5.5 (a-e) shows ATR-FTIR spectra associated with FeS that was exposed to 5 mM nitrite at 70 ^{o}C for 5, 30, 60, 120, 180 minutes. The N-O stretching region exhibits three distinct NO stretching modes at 1777 cm^{-1}, 1747 cm^{-1} and 1715 cm^{-1} that are assigned to the $\upsilon_s(NO)_2$ and $\upsilon_{as}(NO)_2$ of the dinitrosyl group on FeS and the υ(NO) stretch of a nitrosyl group on FeS, respectively. All three surface bound N-O modes show gains in intensity over the course of the three hour run, although there are changes in the relative intensities of these modes. Specifically, spectra observed after 5 minutes (a) and 30 minutes (b) show an increasingly intensity of the band at 1715 cm^{-1}. At longer times, however, the bands at 1777 cm^{-1} and 1747 cm^{-1} show a greater growth in spectral intensity over the band at 1715 cm^{-1}. Additional modes are observed at 1488 cm^{-1} and

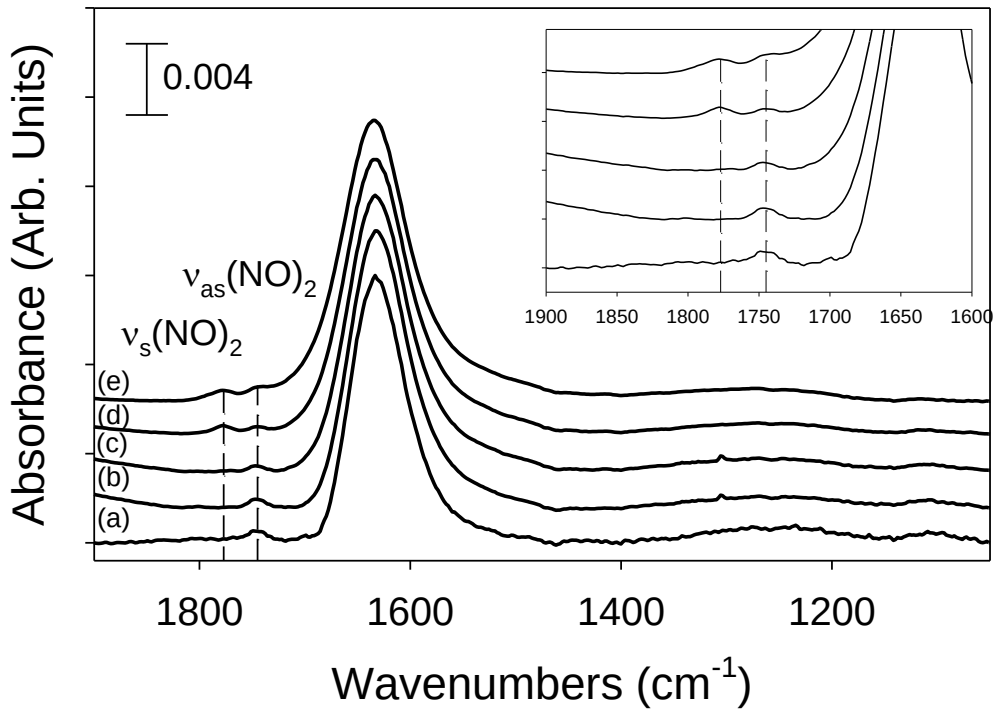

Figure 5.4: In situ ATR-FTIR spectra of FeS exposed to 5 mM nitrite at 22 ^{o}C as a function of time ((a) 5 minutes, (b) 30 minutes, (c) 60 minutes, (d) 120 minutes, and (e) 180 minutes). Note that spectra are offset for clarity.

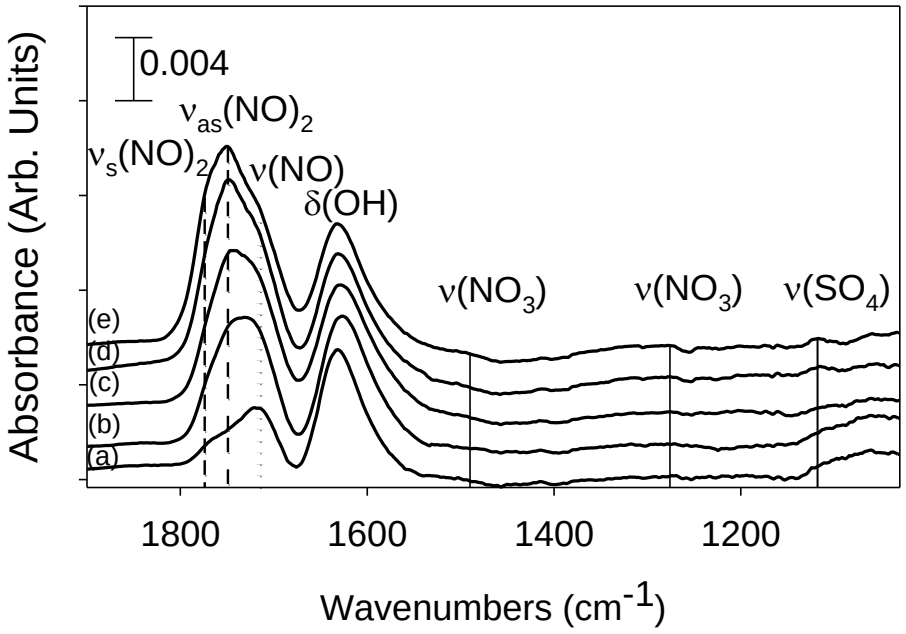

Figure 5.5: In situ ATR-FTIR spectra of FeS exposed to 5 mM nitrite at 70 ^{o}C as a function of time ((a) 5 minutes, (b) 10 minutes, (c) 30 minutes, (d) 120 minutes, and (e) 180 minutes). Note that spectra are offset for clarity.

1270 cm^{-1} that are attributed to adsorbed nitrate species. These modes show little growth over the 180 minute run. Another weak mode is observed at 1120 cm^{-1} and is attributed to sorbed sulfate on the FeS surface. This mode shows small increases in intensity over the course of the experiment.

5.5.2.3 FeS EXPOSED TO 5 mM NITRITE AT 120 ^{o}C

Figure 5.6 exhibits ATR-FTIR spectra of FeS exposed to 5 mM nitrite after 30, 60 and 180 minutes of reaction time 120 ^{o}C. A broadened υ(NO) mode appears at 1806 cm^{-1} after 30 minutes and grows in intensity over 180 minutes of reaction time. Consistent with the appearance of the N-O stretch are modes positioned at 1225 cm^{-1}, 1155 cm^{-1} and 1105 cm^{-1} that we assign to the S-O vibrations associated with sulfate adsorbed on FeS. Two pairs of modes are observed at 1407 cm^{-1} / 1270 cm^{-1} and 1512 cm^{-1} / 1309 cm^{-1} which are attributed to the $\upsilon_{as}(NO_2)$ / $\upsilon_{s}(NO_2)$ modes of surface bound nitrite and the $\upsilon(NO_3)$ pair of nitrate species on the FeS surface, respectively.

5.5.2.4 FeS EXPOSED TO 5 mM NITRATE AT 70 ^{o}C AND 120 ^{o}C

Figure 5.7 (a-d) exhibits ATR-FTIR spectra of FeS exposed to 5 mM nitrate after 30, 60, 120 and 180 minutes at 70 ^{o}C. A low intensity features centered at 1747 cm^{-1} is observed which only exhibits a small increase in intensity over the 180 minute experimental run. This low, broad mode is assigned to the $\upsilon(NO)_{as}$ of a dinitrosyl species bound to FeS.

Figure 5.8 shows ATR-FTIR spectra associated with FeS that was exposed to 5 mM nitrate for 30 and 180 minutes of reaction time at 120 ^{o}C. The υ(NO) mode of N-O bound to the FeS surface is observed at 1758 cm^{-1}, that shows an increase in intensity over the 180 minute run. A pair of modes due to FeS bound nitrite species are observed at

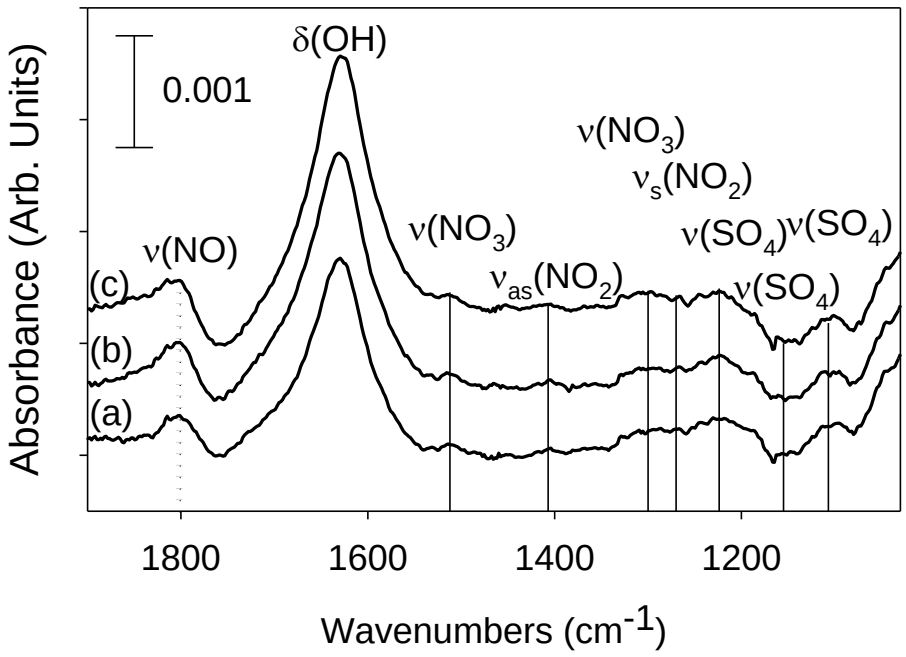

Figure 5.6: In situ ATR-FTIR spectra of FeS exposed to 5 mM nitrite at 120 ^{o}C as a function of time ((a) 15 minutes, (b) 30 minutes and (c) 180 minutes). Note that spectra are offset for clarity.

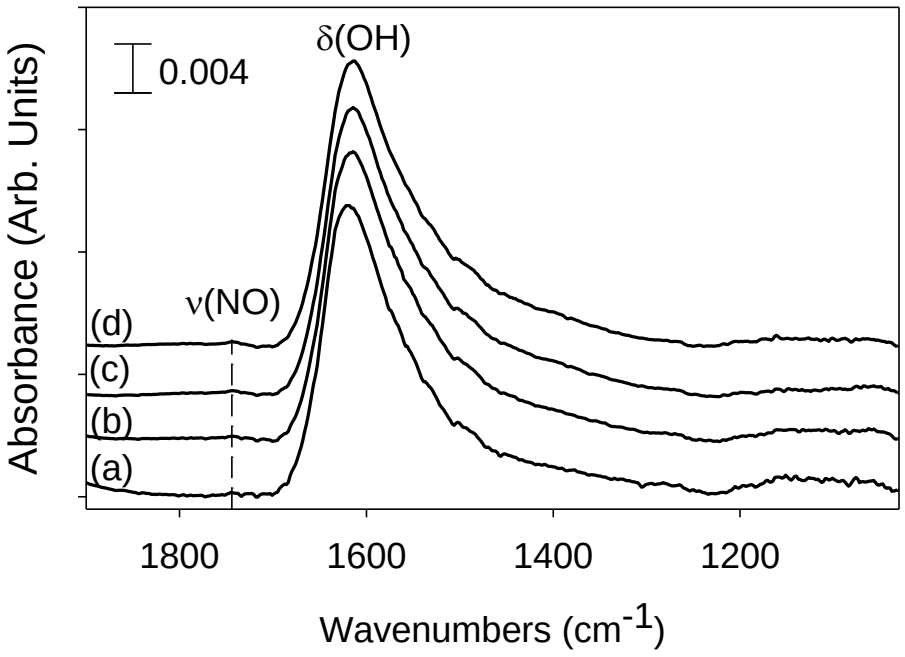

Figure 5.7: In situ ATR-FTIR spectra of FeS exposed to 5 mM nitrate at 70 ^{o}C as a function of time (30 minutes (a), 60 minutes (b), 120 minutes(c), and 180 minutes(d)). Note that spectra are offset for clarity.

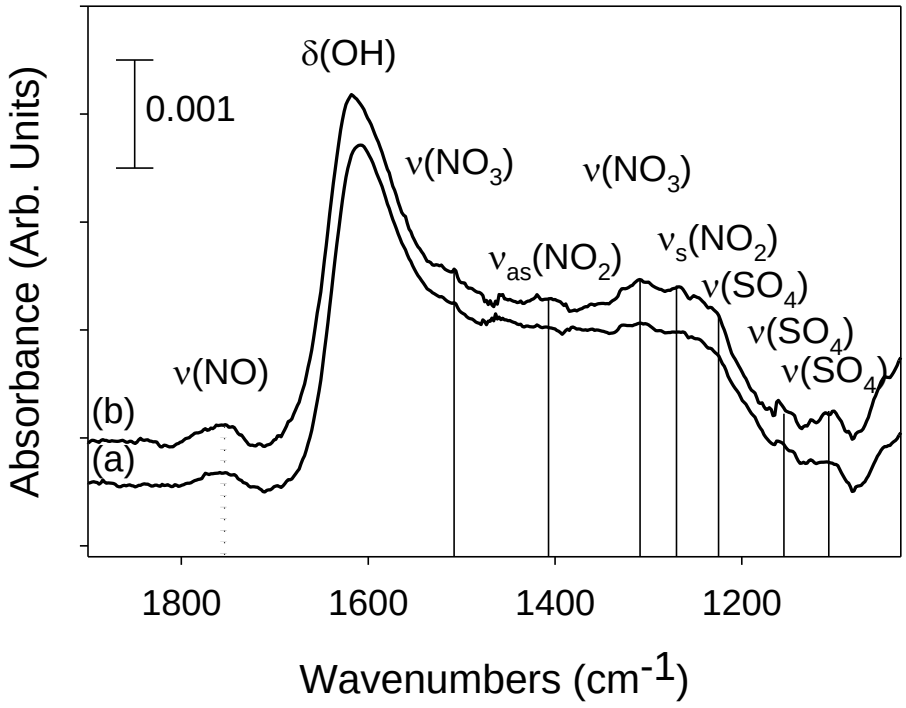

Figure 5.8: In situ ATR-FTIR spectra of FeS exposed to 5 mM nitrate at 120 ^{o}C as a function of time ((a) 30 minutes and (b) 180 minutes are shown). Note that spectra are offset for clarity.

1407 cm^{-1} / 1270 cm^{-1} and a second pair of modes attributed to nitrate coordinated to the FeS surface are observed at 1510 cm^{-1} / 1309 cm^{-1}. Additional modes are also observed at 1225 cm^{-1}, 1155 cm^{-1} and 1105 cm^{-1} which are attributed to adsorbed sulfate.

5.6 DISCUSSION

There are three main aspects of this investigation that warrant further discussion. First, the reduction of nitrite on FeS in alkaline conditions will be discussed, which will highlight the temperature dependence of the reaction. Specifically, the temperature dependence of the reaction in terms of the surface species observed on FeS and the resulting implications for the mechanism of ammonia production will be outlined. Second, the kinetically hindered reduction of nitrate, such that ammonia production is only achieved at 120 ^{o}C, will be described and compared to the 70 ^{o}C experiment which does not produce ammonia. Third, results from this investigation will be viewed in terms of prior work.

5.6.1 TEMPERATURE DEPENDENT AMMONIA PRODUCTION FROM NITRITE AND FeS

The reduction of nitrite on FeS results in significant ammonia production at 70 ^{o}C and 120 ^{o}C, while at a reaction temperature of 22 ^{o}C, insignificant amounts of ammonia are produced. ATR-FTIR spectra support these observations taken from the geochemical batch reactions. The 22 ^{o}C / FeS / nitrite experiment shows low intensity modes observed at 1742 cm^{-1} (υ_{as} $(NO)_2$) and 1777 cm^{-1} ($\upsilon_s(NO)_2$) that are associated with dinitrosyl species. The mode at 1777 cm^{-1} is present after two h of reaction time. We believe that the reason for the absence of the $\upsilon_s(NO)_2$ until two h of reaction time can be explained by changes in the NO-Fe-NO angle on the FeS surface with increasing reaction time. As this

particular angle of the dinitrosyl complex approaches 180°, the integral peak area of the $\upsilon_s(NO)_2$ is greatly decreased relative to the $\upsilon_{as}(NO)_2$, based on infrared surface selection rule arguments [16, 17]. It is noted that after 2 h, the relative intensity of these bands are similar to those observed in the 70 °C nitrite, which we suspect is due to the NO-Fe-NO angle becoming more acute as reaction time proceeds. The change in the angle may result to accommodate the increasing coverage of NO adsorbate as the reaction proceeds. The absence of modes attributable to adsorbed nitrite and the overall low intensity of the dinitrosyl species on the FeS surface at 22°C is consistent with the geochemical batch experiment results that show little ammonia production at this temperature (Figure 5.4 and Figure 5.1, top).

At a reaction temperature of 70 °C there is a rather remarkable increase in surface bound NO modes on FeS compared to the 22 °C / FeS / nitrite experiment. At the same time, significant ammonia production is experimentally observed (Figure 5.1, top) in parallel with a concurrent loss of nitrite from solution (Figure 5.2, middle). In addition to the same dinitrosyl modes observed in the 22 °C experiments at 1742 cm^{-1} ($\upsilon_{as}(NO)_2$) and 1777 cm^{-1} ($\upsilon_s(NO)_2$), a third NO vibrational mode, the υ(NO) of (mono)nitrosyl, is observed at 1710 cm^{-1} and this mode becomes apparent within 5 minutes of the beginning of the reaction.

A reaction temperature of 120 °C for the FeS / nitrate system exhibits the greatest ammonia production of any experiment in this chapter (Figure 5.1, top). Increasing the temperature to 120 °C increases the ammonia yields greatly over the 70 °C case (1.2 mM vs 0.04 mM after 30 h of reaction time). Based on the change in rate with temperature, the activation energy for ammonia production on FeS from nitrite is estimated to be

roughly 15 kcal / mole. This activation energy barrier is significantly lower than the activation barrier associated with the homogeneous reduction of nitrite by ferrous iron. For example, an estimation of the activation barrier associated with the reduction of nitrite by aqueous $Fe^{2+}_{(aq)}$ that was investigated previously by Summers et al. [1] yields a value of 38.1 kcal / mole (based on measured rates between 0^oC and 40^o C). Hence, the FeS surface provides a lower reaction barrier pathway for the production of ammonia than does the homogeneous reaction.

In addition to the more significant ammonia yields observed in the 120 ^oC case, the ATR-FTIR spectra show changes from the 70 ^oC case as well. Perhaps the most important aspect of the spectra is the single υ(NO) mode at 1806 cm^{-1} that we attribute to NO bound on an Fe^{3+} site. The position of this NO vibrational mode suggests that the backbonding mechanism typically associated with the binding of NO on other electron rich iron sulfides is no longer the primary bonding mode. Instead, the electron deficient Fe^{3+} site coordinates to the 5σ antibonding orbital electrons of NO. This bonding configuration results in a single mononitrosyl species, with an υ(NO) mode at 1806 cm^{-1} which is blueshifted relative to the υ(NO) in the 70 ^oC / FeS/nitrite experiment (1710 cm^{-1}). Based on our results, we propose that ammonia formation can be represented by the composite equations 1 and 2.

$$FeS + 5H_2O + 9NO_2^- \rightarrow Fe^{3+} + SO_4^{2-} + 9NO + 10\ OH^- \qquad (5.1)$$

$$16\ H_2O + 9\ NO + 5FeS \rightarrow 9NH_3 + 5\ Fe^{3+} + 5\ SO_4^{2-} + 5OH^- \qquad (5.2)$$

Additional pairs of modes are observed at 1512 / 1309 cm^{-1} and 1408 / 1270 cm^{-1} and are attributed to surface bound nitrate and nitrite adsorbate. The assignment of modes in this region is dubious at best, considering that there is significant overlap of modes

associated with nitrite and nitrate in multiple binding configurations (e.g., monodentate and bidentate geometries) on multiple binding sites [16].

Modes observed at 1512 / 1309 cm^{-1} are assigned to $\upsilon(NO_3)$ of adsorbed nitrate (nitrato). We surmise that the bonding geometry is either monodentate or bidentate based on the splitting of the υ_3 mode of aqueous nitrite caused by the adsorption to the FeS surface. The latter pair of modes observed at 1408 / 1270 cm^{-1} are assigned to the nitro bonding configuration of nitrite. Based on the observed positions, it is possible that these modes correspond to monodentate nitrito species as well, however, based on prior investigations it was determined that the nitro configuration was likely the preferred configuration for ammonia formation [7].

We speculate that the nitro species actively participate in ammonia formation, which proceeds through a surface bound nitrosyl intermediate. The increased rate of nitrite reduction observed throughout the reaction at 120 ^oC and the presence of the 1408 / 1270 cm^{-1} pair suggests that chemistry is occurring that is unique to a reaction temperature of 120 ^oC. Specifically, a temperature dependent adsorption of nitrite on the FeS surface is observed at 120 ^oC given that there is little evidence for the presence of modes assigned to nitro species (i.e., at 1408 / 1270 cm^{-1}) present in the 70 ^oC spectra, nor the 22 ^oC spectra which adds support to this temperature dependant adsorption (activation) of nitrite.

Similarly, the $\upsilon(NO)$ mode displays a similar dependence on temperature. ATR-FTIR spectra show little mode intensity ascribed to N-O stretching modes 22 ^oC. Increasing the reaction temperature to 70 ^oC, however, results in a dramatic increase in intensity, which suggests that there is also a temperature dependent nitrite to nitrosyl

conversion. We suspect that this surface bound NO is a relevant surface intermediate in the production of ammonia.

Though it is difficult to ascertain the binding configurations of both the nitrite and nitrate adsorbate observed in the 120 ^{o}C experiments, there is evidence of a disproportionation reaction mechanism associated the conversion of $2NO_2^- \rightarrow NO + NO_3^- + e^-$ observed on the FeS surface resulting in modes associated with nitrate at 1510 / 1309 cm^{-1} and the υ(NO) at 1806 cm^{-1}. Unfortunately, it is not entirely clear how much of this disproportionation reaction results in the surface bound NO species. It is mentioned that N_2 production is a likely reaction channel, based on prior investigations on pyrite [7].

Equations 5.1 and 5.2 suggest that sulfate is generated as a product in all three reaction schemes. We suspect that the majority of sulfate product partitions to solution, given that we experimentally observe relatively low intensity vibrational modes on FeS at 1225, 1155, and 1105 cm^{-1}, that can be attributed to surface bound sulfate [7, 18, 19]

5.6.2 ACTIVATION OF NITRATE AT 120 ^{o}C

Prior studies have showed that the conversion of nitrate to ammonia is kinetically hindered on pyrite, FeS, and in the presence of $Fe^{2+}_{(aq)}$ at temperatures near 25 ^{o}C [1, 5, 7]. Pyrite was shown, however, to facilitate ammonia from nitrate at a reaction temperature of 120 ^{o}C. The prior investigation of the FeS_2 / nitrate system agrees well with the 120 ^{o}C / FeS / nitrate system that shows a small, but significant amount of ammonia production. Perhaps the most distinct feature of the FeS / nitrate experiment is that at 120 ^{o}C, the υ(NO) mode becomes observable on FeS. We interpret this experimental observation to indicating that reduction of nitrate has occurred at this elevated temperature, resulting in the partial reduction of nitrate to surface bound NO on

FeS (Figure 5.8). This υ(NO) mode is not observed when FeS is exposed to nitrate at a reaction temperature of 22 ^{o}C and although this mode is present at 70 ^{o}C, the low intensity suggests that activation of nitrate has not occurred. We propose that that the pathway to this NO species likely proceeds through surface bound nitrate and nitrite intermediates, based on modes at 1510 / 1309 cm^{-1} and 1407 / 1270 cm^{-1} that we attribute to surface bound nitrate (nitrato) and nitrite (nitro), respectively, in the 120 ^{o}C / FeS / nitrate system. Calculations published in an earlier investigation [7] gives some insight into why nitrate is more difficult to reduce than nitrite and would presumably need higher temperatures to activate. Interestingly, calculations suggest that while nitrite binds to iron via its nitrogen atom (i.e. nitro), nitrate adopts a bonding configuration that has its oxygen atoms binding to the iron component of FeS. The result of these binding configurations is that the N-O stretching frequency associated with nitrite is red-shifted upon adsorption while the N-O stretching frequency associated with nitrate is blue-shifted upon adsorption. In short, the N-O bonds of nitrate become stronger bound to FeS compared to the aqueous species while the N-O bonds of nitrite become weaker on FeS when compared to the aqueous species. These bond strength arguments and the absence of binding via the nitrogen atom of nitrate to FeS are consistent with the experimental observation that nitrate is more difficult to reduce than nitrate.

Additional vibrational modes associated with adsorbed sulfate are observed at 1225, 1155 and 1105 cm^{-1} when FeS is exposed to nitrate at 120^{o}C. Prior work on FeS_2 surfaces has shown that, pyrite (FeS_2), in oxic conditions demonstrates modes in a similar energy range, where electron withdrawal from the sulfur component is followed by the nucleophilic attack of water to form sulfate [18]. In our circumstance we suspect that at

least a fraction of the sulfate product is due to the transfer of electrons from the sulfur component of FeS. These electrons likely go on to reduce a fraction of the adsorbed nitrate to nitrite and then to NO species and such a scenario would be consistent with the following composite reactions:

$$2FeS + 9NO_3^- + H_2O \rightarrow 2Fe^{3+} + 9NO_2^- + 2SO_4^{2-} + 2OH^- \quad (5.3)$$

$$FeS + 5H_2O + 9NO_2^- \rightarrow Fe^{3+} + SO_4^{2-} + 9NO + 10\ OH^- \quad (5.4)$$

5.6.3 SIGNIFICANCE OF RESULTS IN VIEW OF PRIOR WORK

Ammonia production via nitrite and nitrate reduction on pyrite (FeS_2) has been investigated previously in our laboratory using a methodology that was similar to that used in the present study [7]. Nitrite and nitrate reduction has also been studied previously on FeS [4, 5] and pyrrhotite [8]. These prior investigations of ammonia formation have been carried out on the iron sulfides at neutral or acidic pH conditions [5]. In the context of prebiotic chemistry, alkaline conditions on the Hadean may have been more relevant. Russsell and coworkers, for example, have postulated that hydrothermal vents served as natural incubators for prebiotic chemistry. Within these vent systems, a precipitated FeS phase served as a barrier between the acidic Hadean ocean with the alkaline fluids which were rising from within the Earth [9-11]. Therefore, the investigation presented in this chapter is relevant to ammonia formation within the alkaline boundary of the "Russellian" type hydrothermal vent system.

It has been proposed that over the course of about 10^6 years that μM concentrations of nitrogen oxides could have existed within the Hadean Oceans [20]. Research presented here shows that if a Russellian type environment existed during the

Hadean, the basic conditions proposed would have supported ammonia formation, with the caveat that high enough temperatures were present to drive the reactions on the FeS.

References

[1] Summers, D.P., Chang, S., *Nature*, 365 (1993) 630-632.

[2] Walker, J.C.G., Brimblecombe, P., *Precambrian Research*, 28 (1985) 205-222.

[3] Zohner, A., Broda, E., *Origins of Life and Evolution of the Biosphere*, 9 (1979) 291-298.

[4] Blöchl, E., Keller, M., Wächtershäuser, G., Stetter, K.O., *Proceedings of the National Academy of Sciences* USA, 89 (1992) 8117-8120.

[5] Summers, D., *Origins of Life and Evolution of the Biosphere*, 35 (2005) 299-312.

[6] Smirnov, A., Hausner, D., Laffers, R., Strongin, D., Schoonen, M., *Geochemical Transactions*, 9 (2008) 5.

[7] Singireddy, S., Gordon, A.D., Smirnov, A., Vance, M.A., Szilagyi, R.K., Schoonen, M.A., Strongin, D.R., *Astrobiology*, (Submitted).

[8] Brandes, J.A., Boctor, N.Z., Cody, G.D., Cooper, B.A., Hazen, R.M., Yoder, H.S., Jr., *Nature*, 395 (1998) 365-367.

[9] Russell, M.J., Hall, A.J., Cairns-Smith, A.G., Braterman, P.S., *Nature* 336 (1988) 117.

[10] Russell, M.J., Hall, A.J., Turner, D., *Terra Nova*, 1 (1989) 238-241.

[11] Russell, M.J., Daniel, R.M., Hall, A.J., *Terra Nova*, 5 (1993) 343-347.

[12] Macleod, G., McKeown, C., Hall, A.J., Russell, M.J., *Origins of Life and Evolution of the Biosphere*, 24 (1994) 19-41.

[13] Rickard, D., *Stockholm Cont. Geology*, 20 (1969) 67-95.

[14] Michel, F.M., Antao, S.M., Chupas, P.J., Lee, P.L., Parise, J.B., Schoonen, M.A.A., *Chemistry of Materials*, accepted (2005).

[15] Amornthammarong, N., Zhang, J.-Z., *Analytical Chemistry*, 80 (2008) 1019-1026.

[16] Hadjiivanov, K.I., *Catalysis Reviews*, 42 (2000) 71-144.

[17] Braterman, P.S., *Metal Carbonyl Spectra*, Academic Press, London, 1975.

[18] Usher, C.R., Cleveland, C.A., Strongin, D.R., Schoonen, M.A.A., *Environment Science & Technology*, 38 (2004) 5604-5606.

[19] Usher, C.R., Paul, K.W., Narayansamy, J., Kubicki, J.D., Sparks, D.L., Schoonen, M.A.A., Strongin, D.R., *Environmental Science & Technology*, 39 (2005) 7576-7584.

[20] Ducluzeau, A.L., van Lis, R., Duval, S., Schoepp-Cothenet, B., Russell, M.J., Nitschke, W., *Trends in Biochemical Sciences*, 34 (2009) 9-15.

CHAPTER 6

NITRATE AND NITRITE REDUCTION ON Mo-S-PYRITE

6.1 OVERVIEW

Recent work regarding nitrite and nitrate reduction has exhibited the direct participation of pyrite in redox chemistry associated with ammonia formation [1]. In this chapter, tetrathiomolybdate exposed pyrite has been utilized to determine if surface modifications of pyrite are capable of enhancing prebiotically relevant reactions such as the reduction of nitrite and nitrate to ammonia. The application of tetrathiomolybdate to the pyrite surface has direct implications for Origin of Life biogeochemistry, since it has been hypothesized that molybdenum sulfides were present in hydrothermal vent systems on the Hadean and may have played a role in prebiotic chemistry, specifically the development of the active sites of various enzymes such as nitrogenase as well as xanthine oxidase, sulfite oxidase, DMSO reductase, CO dehydrogenase, and molybdopterin enzyme families [2, 3].

Toward the goal of understanding the effect of tetrathiomolybdate on pyrite facilitated reactions, nitrite and nitrate reduction reactions will be conducted on Mo-S-pyrite and pyrite from which ammonia yields will be quantified and compared. In situ attenuated total reflection-Fourier transform infrared spectroscopy will be utilized to monitor the relevant surface intermediates on the Mo-S-pyrite surface associated with nitrite and nitrate reduction which will yield mechanistic details of these reactions. Results from solid state analyses of the Mo-S-pyrite surface using x-ray photoelectron spectroscopy and x-ray fluorescence spectroscopy will also be presented which allow Mo concentration and Mo oxidation state changes to be observed as the reactions proceed.

6.2 INTRODUCTION

The development of the dinitrogen reducing enzyme nitrogenase is thought to be a landmark jump in molecular evolution. The active site of one of the more well studies dinitrogen reducing enzyme, Mo-nitrogenase, consists of an FeS (2 x 2) cluster combined with a molybdenum atom which forms the Mo-Fe-S cubane structure. Despite the wealth of structural information available in the literature, little is known about the mechanisms involved in the evolution of this enzyme from raw materials available on early earth [2].

It has been hypothesized in previous work that ppm amounts of ferrous iron, sulfate, nitrite and nitrate may have been present in the Hadean Ocean and likely on or near hydrothermal vent systems [4-6]. According to prior studies by Summers, interactions of aqueous ferrous iron, nitrite and nitrate ions in solution may have resulted in the formation of μM amounts of ammonia in the Hadean Ocean [7].

Subsequent work also demonstrated that FeS could drive the reduction of nitrite to ammonia [4, 8]. Recently, in situ ATR-FTIR spectroscopy has been utilized to investigate nitrite and nitrate reduction on pyrite and FeS_m nanoparticles which allowed mechanistic details associated with these reactions to be elucidated [1, 8, 9]. Other investigations in this area have yielded batch reaction data using various Fe based surfaces including $Fe^{o}_{(s)}$ [10], pyrrhotite [11], basalt [11] and Fe_3O_4 [11]. Though these surfaces offer some similarities to the Fe-S motifs found in nitrogenase active sites, little effort has been made in decorating mineral surfaces with biologically relevant adsorbates which were also relevant in the context of prebiotic chemistry, to understand what, if any, effect the resulting structure may have on reactions of prebiotic importance.

Building on prior research on nitrite and nitrate reduction on FeS detailed in Chapter 5, this chapter will bring forward investigations that describe the enhancement of nitrite and nitrate reduction kinetics induced by a Mo-modified pyrite surface [1]. Results from geochemical batch reactions will be used to examine ammonia production resulting from the reduction of nitrite and nitrate on the modified pyrite surface. Data obtained from in situ attenuated total reflection-Fourier transform infrared (ATR-FTIR) spectroscopy experiments has been utilized to identify surface intermediates that result from nitrite and nitrate reduction reactions on the modified pyrite surface. Additional results from ex situ solid phase analysis of post reaction solids by x-ray photoelectron spectroscopy (XPS) and x-ray fluorescence (XRF) spectroscopy will also be presented that will yield information regarding both the concentration of Mo and oxidation state of Mo on the pyrite surface as a function of reaction time. Experimental results will be discussed in view of prior work, with an emphasis on the effect of temperature on nitrite and nitrate reduction reaction and the mechanistic implications associated with reactions at 25 ^{o}C, 70 ^{o}C and 120 ^{o}C.

6.3 EXPERIMENTAL METHODS

6.3.1 PREPARATION OF Mo-S-PYRITE

Natural pyrite from Huanzala, Peru (Ward's Natural Science) was optically examined for impurities, ground in an agate ball mill to a size fraction below 60 µm and acid-washed in dilute O_2-free HCl solution. After drying, the samples were stored in a humidity controlled glovebox with N_2 / H_2 atmosphere. The surface area, determined by N_2-BET was 0.613 m^2g^{-1}. For a detailed procedure, consult reference [1]**.** tetrathiomolybdate sorbed pyrite (Mo-S-pyrite) was produced by adapting the procedure

of Helz and coworkers [12]. In brief, dry, acid-washed pyrite was exposed repeatedly to a 100 μM solution of diammonium tetrathiomolybdate ($(NH_4)_2MoS_4$), acidified to pH 4 with dilute HCl until the surface reached saturation with respect to tetrathiomolybdate. The sorption was rapid and marked by the disappearance of characteristic red color. The saturation point was first determined visually when no further color change was observed, and subsequently confirmed with UV-Vis spectroscopy of pre- and post-sorption solution. After the sorption, the tetrathiomolybdate exposed pyrite was washed multiple times with O_2-free deionized water to remove residual ammonium from the solution. Every 3-5 washing cycles, the ammonium content of the effluent was checked with UV-Vis spectroscopy (HACH Salicylate Method, #10023) until stable readings of less than 4 μM were achieved. After drying, MoS_4-pyrite was used in experiments without further modification. The presence of Mo was determined from the presence of Mo $K\alpha_1$ peak in the XRF spectrum. N_2-BET determined surface area of Mo-S-pyrite was 0.508 m^2g^{-1} (a 17.13% reduction in specific surface area, due to the washing process).

6.3.2 EXPERIMENTAL CONSIDERATIONS

Solutions were prepared by dissolving reagent-grade $NaNO_2$ and KNO_3 in Ar-purged, O_2-free deionized water. Dry pyrite and Mo-S-pyrite were weighed out in ambient atmosphere, placed in the 6 mL PEEK and Teflon®-lined stainless steel reactors and immediately transferred into the N_2 / H_2 glovebox. In all instances, the exposure to O_2 was very short, usually less than 5 minutes. In the glovebox, the reacting solution was introduced and the reactors closed. Mineral loading was maintained at 21 g / L in all experiments. Loaded reactors were then placed in a temperature controlled oven on an orbital shaker and agitated at ~150 rpm. Experiments were conducted at 25 ºC, 70 ºC, and

120 ºC. The pH of the solution was not buffered during these reactions and the initial and final solution pH was recorded as indicators for proton source to ammonia formation. Individual samples were withdrawn at desired time intervals, cooled and transferred into the N_2 / H_2 glovebox for disassembly. After filtration (0.22 µm PVDF), the solids were dried in the glovebox; the liquids were frozen until further analysis.

To better elucidate the effect of surface modification on nitrite and nitrate reduction, each experiment utilizing Mo-S-pyrite at 25 ^{o}C, 70 ^{o}C and 120 °C was replicated with unmodified, clean pyrite.

6.3.3 ANALYTICAL CONSIDERATIONS

Nitrate, nitrite and sulfate were analyzed on a Dionex DX500 ion chromatograph with a 4 mm IonPac® AS4A-SC anion column and a 1.7 / 1.8 mM $NaHCO_3$ / Na_2CO_3 eluent, respectively. Concentrations were calculated from a linear 4-point calibration curve with R^2 values above 0.99. Ferrous and total iron in solution were analyzed at 562 nm (method 8147) using a HACH DR / 4000 spectrophotometer after an incubation with ferrozine and ferrozine / 30 molal ascorbic acid, respectively. Ammonium was analyzed using an adapted fluorescence method [13] on a Barnstead Quantech FM109515 fluorometer with 360 nm and 420 nm narrow band excitation and emission filters, respectively. Samples and standards with individual volumes of 175 µL were pipetted into polypropylene vials with 3 mL of working reagent and incubated in the dark for 24 - 48 hours. Ammonium concentrations were calculated from a linear 9-point calibration curve with R^2 values above 0.99.

6.3.4 ATR-FTIR METHODOLOGY

Two ATR accessories were utilized in this work. The 25 ^{o}C and 70 ^{o}C ATR-FTIR experiments utilized a Germanium (Ge) multibounce ATR accessory (Pike Technologies). The 120 ^{o}C experiments utilized a diamond single bounce ATR accessory (Specac) which was pressurized with 50 bar ultrahigh purity argon to elevate the boiling point of H_2O. Each accessory was coupled with a Nicolet Magna 750 FTIR spectrometer with a liquid N_2 cooled mercury cadmium telluride A (MCTA) detector. The Ge multibounce unit was set to record single beam spectra as an average of 100 scans with a resolution of 4 cm^{-1}. An initial single-beam spectrum was recorded as soon as the cell reached the desired reaction temperature (t=0 h) which was used as a background for the subsequent single-beam spectra. For the 25 ^{o}C spectra, a single beam spectrum was recorded as soon as the cell was placed into the spectrometer (~30 seconds after loading). The single bounce diamond ATR was setup to record single beam spectra as an average of 100 scans with a resolution of 4 cm^{-1}. A background spectrum was taken as soon as cell was stabilized at 120 ^{o}C, after which a reference spectrum is recorded and used as a reference for subsequent spectra.

6.3.5 ANALYSIS OF SOLIDS

Mo-S-pyrite solids obtained from geochemical batch reactions were immediately placed under a stream of dry N_2 / H_2 gas and allowed to dry. After drying they were transferred into labeled samples tubes and stored in the same atmosphere until needed.

Standardless Wavelength Dispersive X-Ray Fluorescence Analysis (henceforth XRF) was conducted on a Bruker AXS S4 Pioneer spectrometer using a Rh X-ray source.

Loose sample powders (approximately 0.2 grams) were loaded into nylon sample holders with a 4 µm ultralene bottom and analyzed under UHP Helium atmosphere. Appropriate matrix corrections and the evaluation of results were performed using the SPECTRA™ software suite.

X-ray photoelectron spectroscopy was performed using an unchromatized Mg Ka x-ray source (1253.6 eV) excitation source and a hemispherical energy analyzer biased at pass energy of 50 eV. The vacuum chamber has a base pressure of 10^{-10} torr. All energies were referenced to the sample Fermi level. The spectrometer was calibrated using FeS_2 (pyrite), $(NH_4)_2MoS_4$ and MoS_2 standards.

Each sample was prepared for analysis in a glove bag modified to fit onto the introduction port of the vacuum chamber which was monitored for any observable oxygen contamination. Samples were mounted inside of this glovebag when the O_2 monitor read below the detection limit (< 0.1 ppm).

6.4 RESULTS

Results from experiments conducted using Mo-S-pyrite slurries that were exposed to solutions containing 5 mM nitrite or nitrate will now be described. Specifically, results from batch geochemical experiments will demonstrate ammonia yields (normalized to mineral surface area) and each reaction's corresponding nitrate and / or nitrite concentrations as a function of reaction time at 25 ^{o}C, 70 ^{o}C and 120 ^{o}C in the presence of Mo-S-pyrite and compared to equivalent experiments conducted using unmodified pyrite. Additionally, results obtained in situ from ATR-FTIR spectroscopy of Mo-S-pyrite reacting with nitrite and nitrate will be presented to demonstrate the presence of the NO intermediate associated with nitrite or nitrate reduction on Mo-S-pyrite which will be

compared to that of the pyrite surface observed in prior investigations [1]. Finally, XPS and XRF analysis of the post-reaction Mo-S-pyrite at 25 ^{o}C, 70 ^{o}C and 120 ^{o}C will allow changes in Mo oxidation state and Mo concentration to be investigations as a function of reaction time.

6.5 GEOCHEMICAL BATCH REACTION RESULTS

6.5.1 NITRITE Mo-S-PYRITE EXPERIMENTS

Ammonia, nitrite and nitrate concentrations that result from nitrate and nitrate reduction at 25 ^{o}C on Mo-S-pyrite, 70 ^{o}C on Mo-S-pyrite and pyrite 120 ^{o}C on Mo-S-pyrite and pyrite will be presented below. Results from batch reactions with both Mo-S-pyrite and pyrite blank experiments in which these materials were exposed to O_2- free DI water are also included for comparison. Ammonia concentrations resulting from these blank experiments as well as the experimental data are all normalized to particle surface area, however, nitrite and nitrate concentrations presented in this Chapter are presented not normalized to surface area.

Figure 6.1 shows ammonia formation in batch experiments from 5 mM nitrite on Mo-S-pyrite at 25 ^{o}C, 70 ^{o}C and 120 ^{o}C. Reaction of nitrite with Mo-S-pyrite at 25 ^{o}C resulted in ammonia yields that reached a value of 33.5 μmol / kg after 43.5 h. The corresponding Mo-S-pyrite DI water blank experiment yielded 13.4 μmol / kg ammonia after 43 h. At a temperature of 70 ^{o}C, Mo-S-pyrite reacted with 5 mM nitrite to produce 54.5 μmol / kg after 17.5 h and increased to 66.6 μmol / kg ammonia after 66 h. The same experiment conducted with pyrite instead of Mo-S-pyrite resulted in 41.1 μmol / kg after 56.25 h. The Mo-S-pyrite / DI water and pyrite / DI water control experiments conducted at 70 ^{o}C resulted in 33.5 μmol / kg and 24.4 μmol / kg ammonia

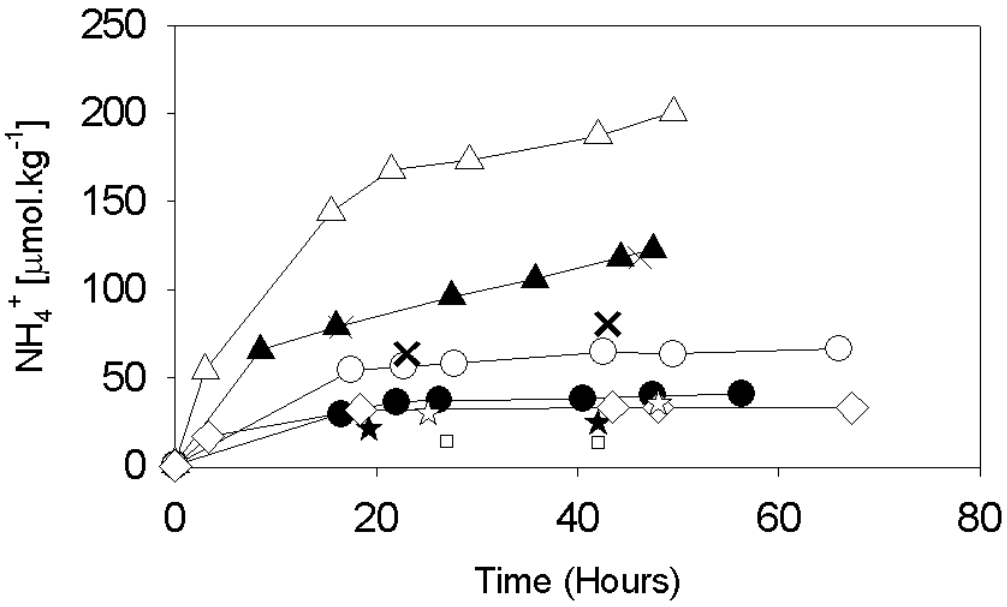

Figure 6.1: The results of batch reaction measurements of ammonia generated by the reaction of 5 mM nitrite and Mo-S-pyrite at 25 ^{o}C (◊), 70 ^{o}C (○) and 120 ^{o}C (Δ) and pyrite at 70 ^{o}C (●) and 120 ^{o}C (▲) as a function of reaction time. Ammonia concentrations from blank experiments are shown as single data points for Mo-S-pyrite / DI water / 25 ^{o}C (□), 70 ^{o}C (✯) and 120 ^{o}C (×) and pyrite / DI water / 70 ^{o}C (★) and 120 ^{o}C (✕). Note this data is normalized to mineral surface area.

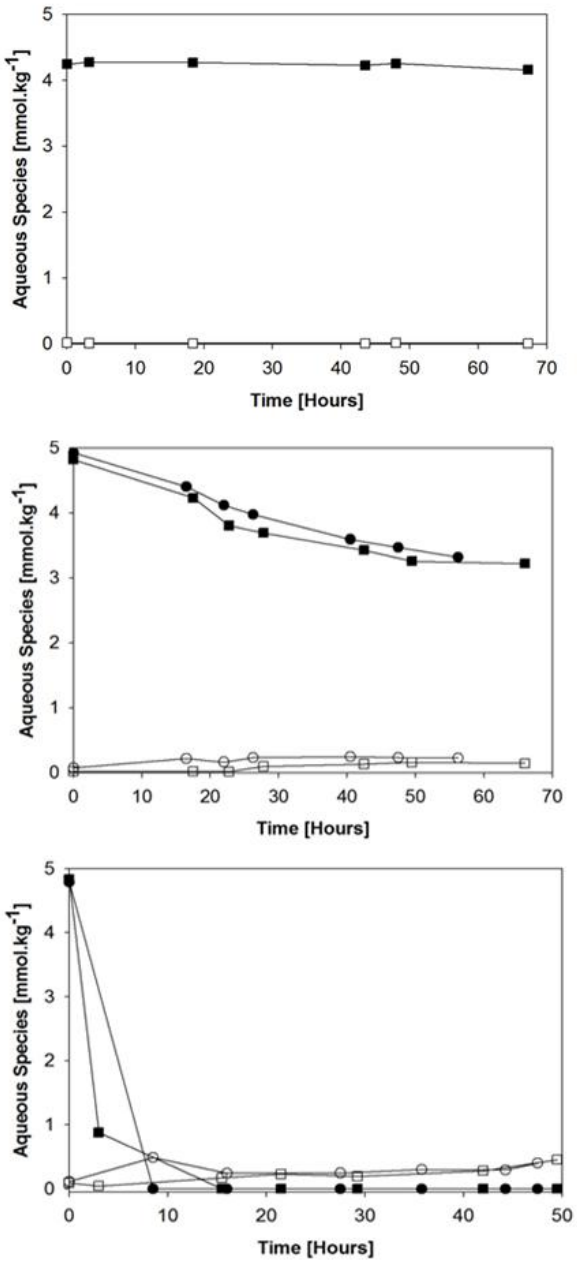

Figure 6.2: Nitrite and nitrate concentrations as a function of time for reactions of 5 mM nitrite (closed shapes) and nitrate (open shapes) with Mo-S-pyrite at 25 ^{o}C (top [■]), 70 ^{o}C (middle [●,○]) and 120 ^{o}C [bottom (●,○)] and pyrite at 70 ^{o}C (middle [■,□]) and 120 ^{o}C (bottom [●,○]). Note that this data is not normalized to surface area.

after 48 and 42 h, respectively.

The reduction of nitrite on Mo-S-pyrite and pyrite at 120 ^{o}C produced roughly 173.15 μmol / kg and 96.07 μmol / kg ammonia, after 29.25 h and 27.5 h, respectively. These yields increased to 200.4 μmol / kg and 122.8 μmol / kg after 49.5 and 47.5 h, repectively. Mo-S-pyrite / DI water and pyrite / DI water control experiments at 120 ^{o}C yielded 118.0 μmol / kg and 80.7 μmol / kg ammonia after 46.25 h and 43 h, respectively.

Nitrite concentrations are shown in Figure 6.2 as a function of time which result from the reaction of 5 mM nitrite / pyrite and 5 mM nitrite / Mo-S-pyrite experiments at 25 ^{o}C (top), 70 ^{o}C (middle) and 120 ^{o}C (bottom). At 25 ^{o}C, the concentration of nitrite decreased slightly (< 0.5 mmol / kg) over the course of the run when exposed to Mo-S-pyrite. At 70 ^{o}C, exposure of 5 mM nitrite to Mo-S-pyrite and pyrite results in ~3.5 mmol / kg nitrite, a decrease of ~1.5 mmol / kg, for both of the experiments after 24 h. Slightly less nitrite is observed in the Mo-S-pyrite case. After 48 h, nitrite concentrations observed were just over 3 mmol / kg for these experiments. These experiments generated less than 500 μmol / kg nitrate concentrations over the course of the runs.

Reaction of 5 mM nitrite / pyrite and 5 mM nitrite / Mo-S-pyrite at 120 ^{o}C results in a substantial decrease in nitrite at 120 ^{o}C during the first 10 h of reaction in which nitrite concentrations drop nearly to zero. A slight increase in nitrate is observed during these reactions which remain below 1 mmol / kg.

6.5.2 NITRATE Mo-S-PYRITE EXPERIMENTS

Figure 6.3 shows batch kinetic data associated with ammonia formation from reactions of 5 mM nitrate / Mo-S-pyrite at 25 ^{o}C, 70 ^{o}C and 120 ^{o}C and 5 mM nitrate /

pyrite at 70 ^{o}C and 120 ^{o}C. The 25 ^{o}C Mo-S-pyrite experiments resulted in 23.9 μmol / kg ammonia after 49.75 h of reaction time. At a temperature of 70 ^{o}C, the Mo-S- pyrite and pyrite produced 50.1 μmol / kg and 31.1μmol / kg, after 52 h and 75.25 h of reaction time. At a temperature of 120 ^{o}C, the Mo-S-pyrite and pyrite produced 136.3 μmol / kg and 121.4 μmol / kg ammonia, after 63.5 and 52.6 h of reaction time, respectively. The same control experiments were used in both the sets of experiments presented in Figures 6.1 and 6.3; results from the control experiments described in section 6.5.1.

Figure 6.4 shows nitrate concentrations as a function of time obtained from reaction of Mo-S-pyrite with 5 mM nitrate at 70 ^{o}C and 120 ^{o}C. At 70 ^{o}C there is no observable decrease in nitrate relative to the pyrite and Mo-S-pyrite experiments starting concentrations of nitrate. However at 120 ^{o}C, there is a decrease of 0.250 mmol / kg and 0.100 mmol / kg nitrate in the Mo-S-pyrite and pyrite experiments, respectively.

6.6 ATR-FTIR RESULTS

Results obtained in situ from ATR-FTIR experiments are presented in the spectral range of 1900 and 1550 cm^{-1}. It is mentioned that all ATR-FTIR datasets presented in this contribution show the δ(OH) mode originating from molecular water at ~1633 cm^{-1}.

6.6.1 ATR-FTIR RESULTS OF NITRITE REDUCTION ON Mo-S-PYRITE AT 25 ^{o}C, 70 ^{o}C AND 120 ^{o}C

Figure 6.5 (a-e) shows ATR-FTIR spectra obtained in situ associated with the reaction of 5 mM nitrite and Mo-S-pyrite at 25 ^{o}C after reaction times of 5, 10, 30, 120 and 180 minutes. Two overlapping modes centered at approximately 1770 and 1750 cm^{-1} are observed. The 1770 cm^{-1} mode is observed after only 5 minutes and grows in

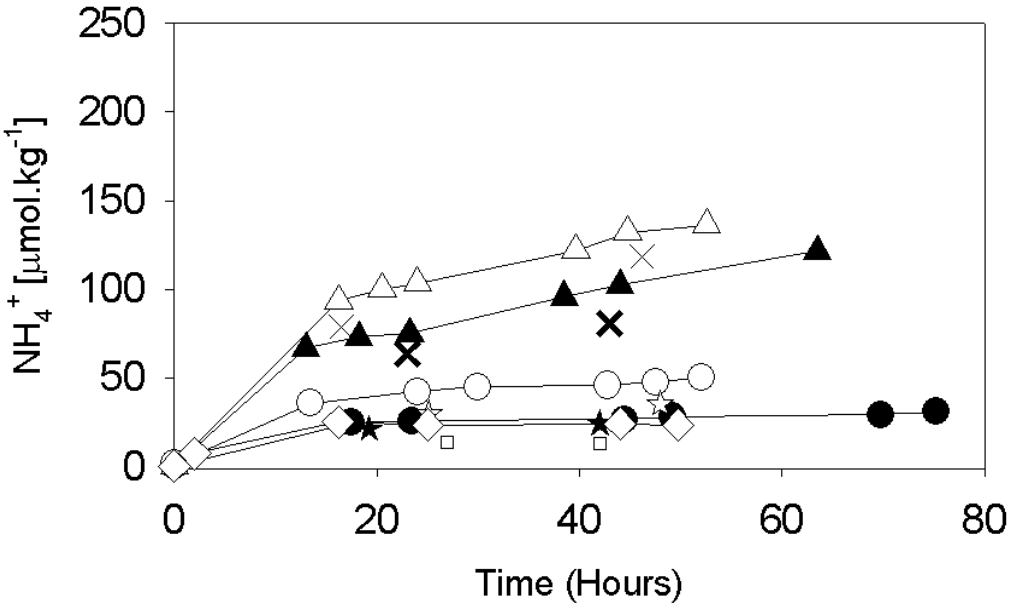

Figure 6.3: The results of batch reaction measurements of ammonia generated by the reaction of 5 mM nitrate and Mo-S-pyrite at 25 ^{o}C (◊) 70 ^{o}C (○) and 120 ^{o}C (Δ) and pyrite at 70 ^{o}C (●) and 120 ^{o}C (▲) as a function of reaction time. Ammonia concentrations obtained from blank experiments are shown for the Mo-S-pyrite / DI water at 25 ^{o}C (□), 70 ^{o}C (✯) and 120 ^{o}C (×) and pyrite / DI water at 70 ^{o}C (★) and 120 ^{o}C (✕) experiments after 24 and 48 h. Note these data are normalized to mineral surface area.

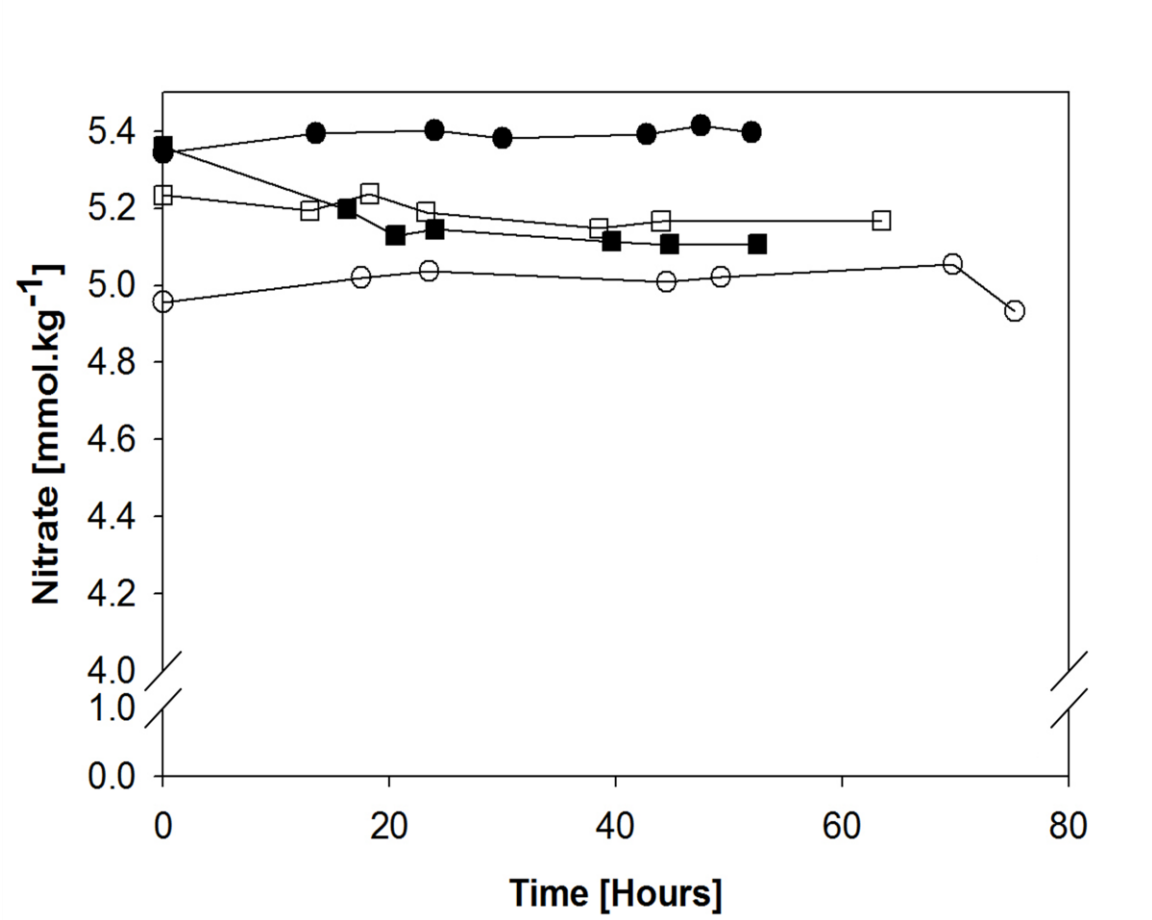

Figure 6.4: The results of batch reaction measurements of nitrate in reactions of 5 mM nitrate and Mo-S-pyrite (●) and pyrite (○) at 70 ^{o}C and Mo-S-pyrite (■) and pyrite (□) at 120 ^{o}C.

intensity over the course of the experimental run. This mode is tentatively assigned to mononitrosyl on Mo^{4+}. The mode positioned at 1750 cm^{-1} grows in over more rapidly at a later period in the reaction and is assigned to mononitrosyl species on Fe^{2+}. Figure 6.6 shows ATR-FTIR spectra associated with the Mo-S-pyrite / nitrite experiment at 70 ^{o}C at reaction times of 5, 10, 30, 120 and 180 minutes (a-e). Modes observed at 1790 cm^{-1} and 1745 cm^{-1} after 5 and 10 minutes are attributed to the $\upsilon_s(NO)_2$ and $\upsilon_{as}(NO)_2$ of dinitrosyl groups, respectively. These modes increase rapidly for the first 5 minutes of reaction, after which a rapid decline in intensity is observed. This decline continues over the three h run (Figure 6.6, c-e). This specific change in the spectra will be discussed in section 6.8.2.

Figure 6.7 shows ATR-FTIR spectra associated with Mo-S-pyrite / nitrite at a reaction temperature of 120 ^{o}C. These spectra show mode intensity attributed to dinitrosyl groups at 1840 cm^{-1} and 1710 cm^{-1} which are assigned to $\upsilon_s(NO)_2$ and $\upsilon_{as}(NO)_2$ of dinitrosyl on Mo, and a third mode observed at 1750 cm^{-1} , which is assigned to υ(NO) of mononitrosyl on Fe^{2+}. After 5 minutes, these modes show a significant intensity, but these same modes show an intensity decrease over the three hour experimental run. The dinitrosyl groups on Mo are not observed after 5 minutes of reaction.

6.6.2 ATR-FTIR RESULTS OF NITRATE REDUCTION ON Mo-S-PYRITE AT 25 ^{o}C, 70 ^{o}C AND 120 ^{o}C

Figure 6.8 (top) shows ATR-FTIR spectra associated with the Mo-S-pyrite / nitrate system at a reaction temperature of 70 ^{o}C. The only feature that is readily observed in the spectrum is the δ(OH) of water observed at 1633 cm^{-1}. Figure 6.8 (bottom) shows ATR-FTIR spectra obtained from the Mo-S-pyrite / nitrate /120 ^{o}C experiment after 30,

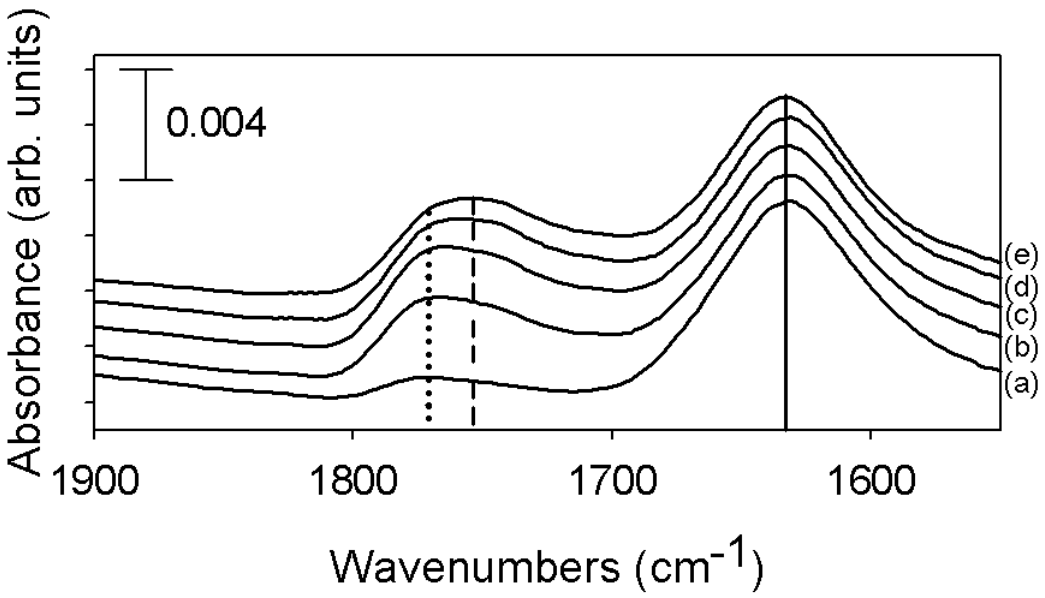

Figure 6.5: In situ ATR-FTIR spectra of Mo-S-pyrite exposed to 5 mM nitrite at 25 ^{o}C as a function of time. In situ ATR-FTIR spectra of Mo-S-pyrite exposed to 5 mM nitrite at 25 ^{o}C for (a) 5 minutes, (b) 10 minutes, (c) 30 minutes, (d) 120 minutes, and (e) 180 minutes are shown. Note that spectra are offset for clarity.

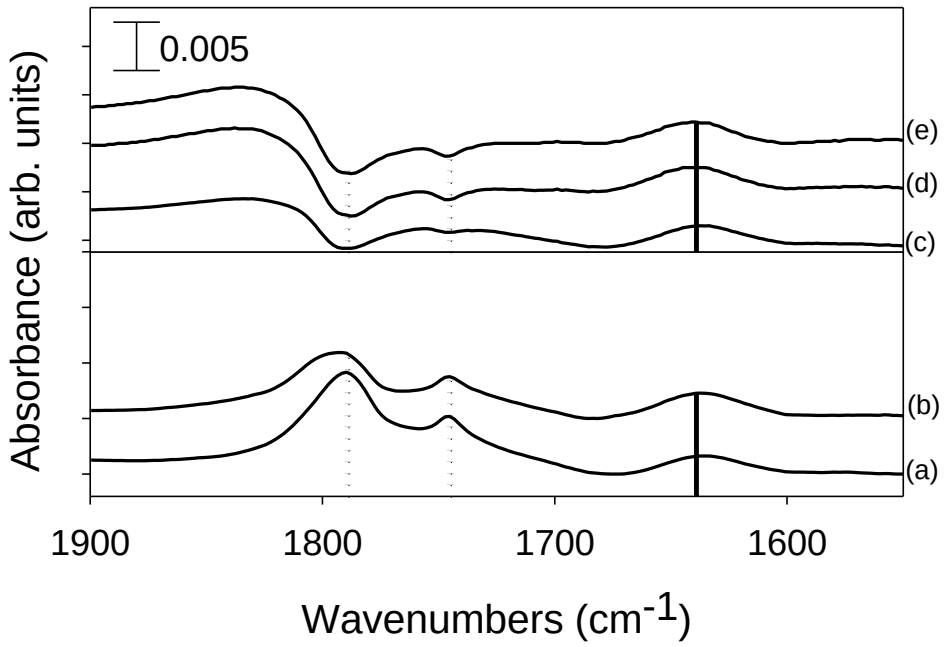

Figure 6.6: In situ ATR-FTIR spectra of Mo-S-pyrite exposed to 5 mM nitrite at 70 ^{o}C as a function of time. In situ ATR-FTIR spectra of Mo-S-pyrite exposed to 5 mM nitrite at 70 ^{o}C for (a) 5 minutes, (b) 10 minutes, (c) 30 minutes, (d) 120 minutes and (e) 180 minutes are shown. Note that spectra are offset for clarity.

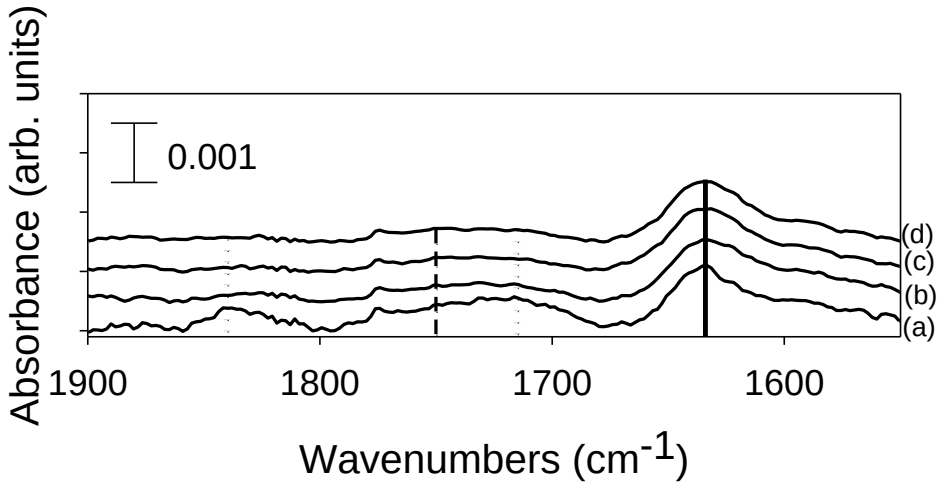

Figure 6.7: In situ ATR-FTIR spectra of Mo-S-Pyrite exposed to 5 mM nitrite at 120 ^{o}C as a function of time. In situ ATR-FTIR spectra of Mo-S-pyrite exposed to 5 mM nitrate at 120 ^{o}C (a) 5 minutes, (b) 60 minutes, (c) 120 minutes and (d) 180 minutes are shown. Note that spectra are offset for clarity.

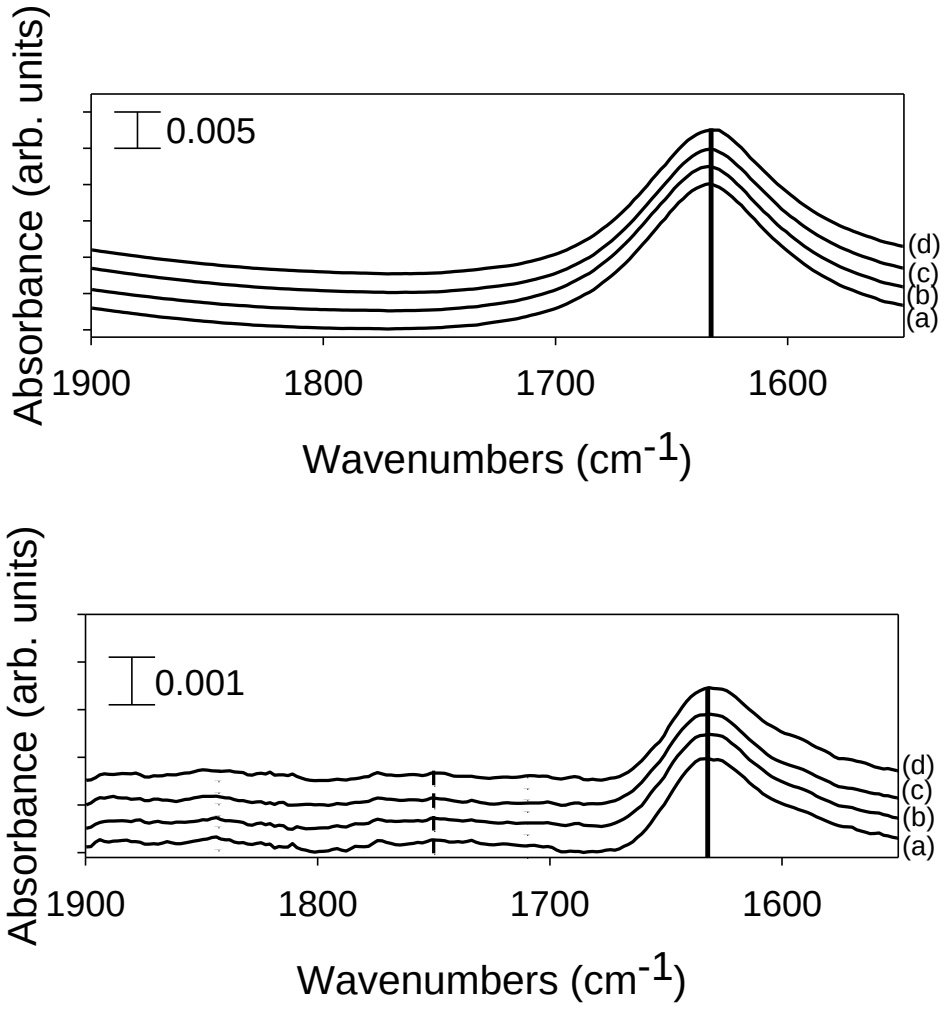

Figure 6.8: In situ ATR-FTIR spectra of Mo-S-pyrite exposed to 5 mM nitrate at 70 and 120 ^{o}C as a function of time. (top) In situ ATR-FTIR spectra of Mo-S-pyrite exposed to 5 mM nitrate at 70 ^{o}C for (a) 5 minutes, (b) 30 minutes, (c) 60 minutes, (d) 120 minutes and (e) 180 minutes are shown. (bottom) In situ ATR-FTIR spectra of Mo-S-pyrite exposed to 5 mM nitrate at 120 ^{o}C for (a) 30 minutes, (b) 60 minutes, (c) 120 minutes and (d) 180 minutes are shown. Note that spectra are offset for clarity.

60, 120 and 180 minutes. Three broad maxima all attributed to υ(NO) at 1835 (dotted line), 1750 (dashed line) and 1710 cm^{-1} (dotted line) are observed after 5 minutes and show little change in intensity over the three hour run.

6.7 SOLID STATE ANALYSIS RESULTS

6.7.1 X-RAY FLUORESCENCE SPECTROSCOPY

Figure 6.9 shows the wt % Mo that remains on the Mo-S-pyrite surface as a function of reaction time at 70 ^{o}C and 120 ^{o}C for Mo-S-pyrite exposed to DI water, nitrite, and nitrate as determined by XRF spectroscopy. The initial Mo content of the Mo-S-pyrite material was determined to be 496 ppm, which is the average of 18 individual Mo-S-pyrite samples. Reactions with O_2 free DI water at 25 ^{o}C, 70 ^{o}C and 120 ^{o}C produced a general trend which shows little discernable change in the Mo concentration over time. Exposure to nitrite at the same temperatures yielded, in general, a decreasing trend of surface Mo with increasing reaction time.

6.7.2 X-RAY PHOTOELECTRON SPECTROSCOPY

Figure 6.10 shows the results of XPS spectra of Mo-S-Py exposed to O_2 free deionized water at 25 ^{o}C (top), 70 ^{o}C (middle) and 120 ^{o}C (bottom) from 240 to 215 eV. After 2 h and 66 h of reaction time at 25 ^{o}C, peaks attributed to Mo $3d_{3/2}$ and Mo $3d_{5/2}$ core levels are observed at 232.8 and 229.4 eV, respectively, and are denoted by dotted lines. The S 2s core level is observed at 227.4 eV and is marked with a solid line. At a reaction temperature of 70 ^{o}C, Mo 3d spectral intensity is still present even after 97 hours of reaction time. Additional intensity can be observed at 232.8 eV and ~236 eV which

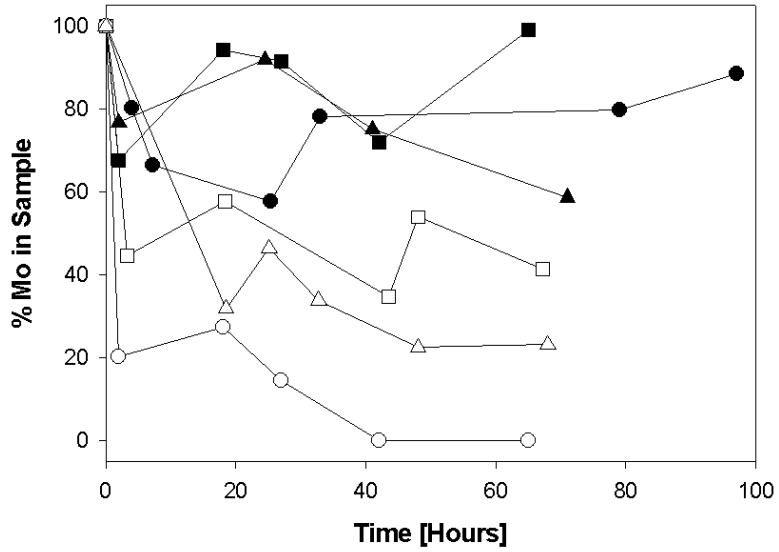

Figure 6.9: Mo content of Mo-S-pyrite exposed to O_2 free DI water at 25 ^{o}C (■), 70 ^{o}C (▲) and 120 ^{o}C (•) and nitrite at 25 ^{o}C (□), 70 ^{o}C (○) and 120 ^{o}C (△) obtained from XRF analysis as a function of reaction time. The starting concentration of Mo on Mo-S-pyrite was 496 ppm.

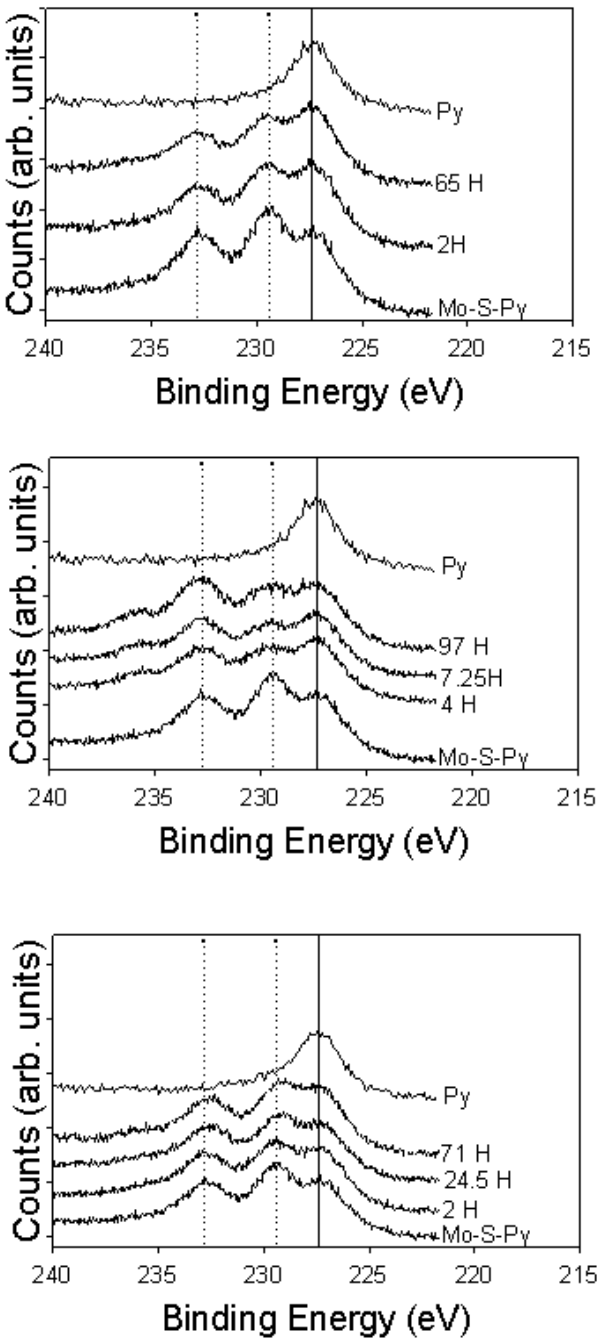

Figure 6.10: XPS spectra of Mo-S-pyrite exposed to deionized / deoxygenated water at 25 ^{o}C (top), 70 ^{o}C (middle) and 120 ^{o}C (bottom) as a function of time. The spectra marked "Mo-S-py" and "py" refer to tetrathiomolybdate exposed pyrite and pristine pyrite, respectively.

increases in intensity as the reaction proceeds. At 120 ^{o}C, the Mo 3d pair associated with the reacted surface is similar to Mo-S-pyrite before reaction although there is a small shift to higher binding energies as the reaction proceeds. At all three temperature ranges, the Mo 3d features are still evident at the end of each respective run.

Figure 6.11 shows XPS spectra of Mo-S-pyrite exposed to 5 mM nitrite after 3.5, 16.5 and 66 hours at 25 ^{o}C. The S 2s core level is observed at 227.4 eV and is ubiquitous in all the spectra presented. The Mo $3d_{3/2}$ and Mo $3d_{5/2}$, usually observed at 232.8 and 229.4 eV show substantially less intensity than those observed in Mo-S-pyrite prior to reaction. XPS spectra of Mo-S-pyrite exposed to 5 mM nitrate as a function of exposure time at 25 ^{o}C are shown in Figure 6.12. After 2 h of nitrate exposure, there is a slight shift in the Mo 3d bands (~0.6 eV) to higher binding energies. There is little variation in the Mo 3d intensity relative to that of the S 2S peak.

A zoomed view of the energy range between 237 and 228 eV of Mo-S-pyrite exposed to nitrite at 25 ^{o}C (top) and 70 ^{o}C (bottom) is shown in Figure 6.12. At 25 ^{o}C, intensity is observed at 232.8 eV after 66 hours of exposure time. Exposure of Mo-S-pyrite to nitrite at 70 ^{o}C resulted in the appearance of intensity in the same energy window, however, after 66 hours, this feature is no longer observed.

6.8 DISCUSSION

6.8.1 STABILITY OF Mo-S-PYRITE SURFACE IN O_2 FREE DI WATER, NITRITE AND NITRATE AS A FUNCTION OF TEMPERATURE

Temperature has been shown to play a key role in accelerating prebiotically relevant chemical reactions (i.e. nitrite and nitrate reduction) on iron sulfide surfaces [9] [1]. Given that molybdenum sulfur compounds have been hypothesized to exist in

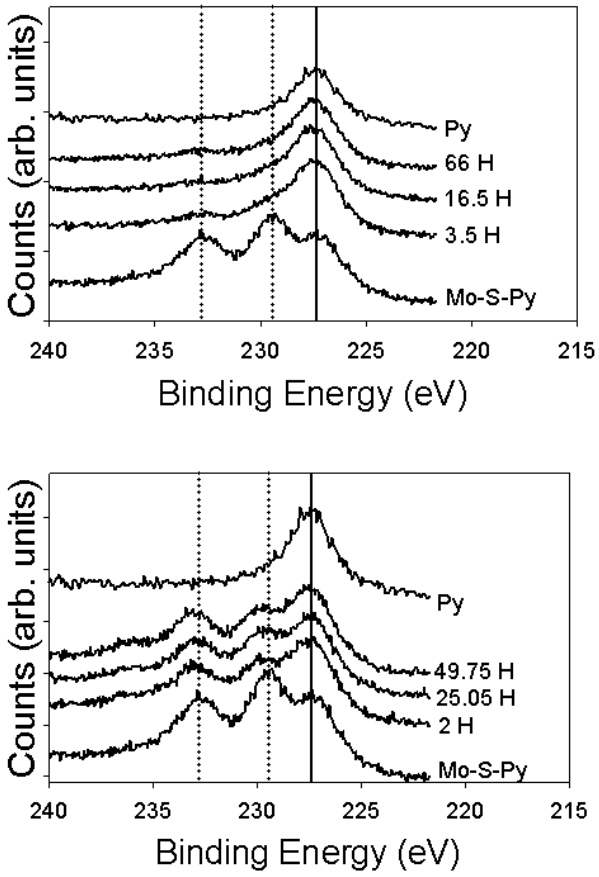

Figure 6.11: XPS spectra of Mo-S-pyrite exposed to 5 mM nitrite (top) and nitrate (bottom) as a function of time at 25 ^{o}C. The spectra marked "Mo-S-py" and "py" refer to tetrathiomolybdate exposed pyrite and pristine pyrite, respectively.

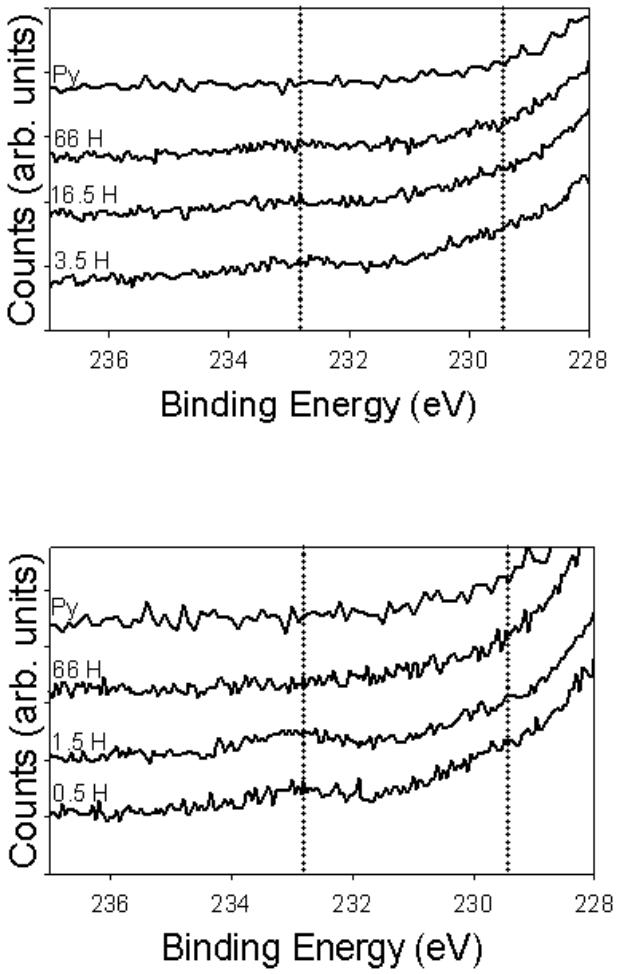

Figure 6.12: XPS spectra of Mo-S-pyrite exposed to 5 mM nitrite at 25 ^{o}C (top) and 70 ^{o}C (bottom) as a function of time. The spectra marked "py" refers to pristine pyrite.

prebiotic scenarios that were both rich in iron sulfides material and elevated in temperature, it was necessary to determine what role temperature may have played in the chemistry of these compounds, in prebiotic reaction scenarios [3].

XPS was used to characterize the Mo-doped pyrite (Mo-S-pyrite) surface before and after reaction with nitrite and nitrate. Exposure of pyrite to tetrathiomolybdate yielded a Mo $3d_{5/2}$ peak at 232.8 eV, which is consistent with the presence of Mo^{4+} and is shifted 3.2 eV to lower binding energy than that associated with Mo in the molecular parent compound diammonium tetrathiomolybdate (236.7 and 233.6 eV respectively) [14]. We take from this result that the Mo is reduced upon adsorption on the pyrite surface. While the Mo 3d binding energies of Mo-S-pyrite observed are similar to the Mo 3d levels of MoS_2, this compound is ruled out by 1) spectra of MoS_2 reference compounds and 2) by prior investigations which concluded that MoS_2 does not form from diammonium tetrathiomolybdate at temperatures below 300 ^oC [15].

In order to establish the stability of Mo on the pyrite surface, experiments conducted with Mo-S-pyrite (in O_2 free DI water) at 25 ^oC, 70 ^oC, and 120 ^oC. The results of these experiments are shown in Figure 6.10 (top, middle, bottom, respectively). At 25 ^oC, there is little deviation in binding energy after O_2 free DI water exposure on the spectra from the Mo-S-pyrite. However, at 70 ^oC, two new features become apparent at 236.3 and 233.2 eV which are consistent with the Mo $3d_{5/2}$ and $3d_{3/2}$ levels of Mo^{6+}. Prior literature has suggested that these features can be assigned to MoO_3 however it may be just as likely a mixed MoS_xO_y species [16, 17]. At 120 ^oC, the Mo 3d levels show more broadening then at lower temperatures. Specifically, features at 229.1 and 232.4 increase in intensity over the 71 h run and are attributed to the Mo $3d_{5/2}$ and $3d_{3/2}$ of Mo^{4+}. We

suspect that the increased temperature induces some minor oxidation reactions, resulting in the formation of MoO_2. Despite the small variations in oxidation state change among the three temperatures tested, these experiments show that Mo remains bound on the Mo-S-pyrite surface.

In order to further understand the role of temperature in the Mo desorption process, Mo-S-pyrite was exposed to nitrite 25 ^{o}C and 70 ^{o}C (Figure 6.12, top and bottom, respectively). Results from the nitrite / 70 ^{o}C experiment indicate that much of the Mo desorbs almost completely within 30 minutes of reaction time. Consistent with the rapid growth and subsequent loss of dinitrosyl modes observed in the ATR-FTIR experiments, it appears as though these processes are coupled. Further indications of this relationship is a small feature that grows in at ~233 eV between 0.5 and 1.5 hours which is attributed to oxidized Mo. Alternatively, at 25 ^{o}C, this feature is observed throughout the reaction. Based on the data presented, there is likely a temperature dependent component of the observed Mo oxidation, however, more investigation is required to prove this hypothesis.

6.8.2 EFFECT OF Mo-S-PYRITE ON THE KINETICS AND MECHANISM OF NITRITE AND NITRATE REDUCTION

The role of iron sulfides in nitrate and nitrite reduction has been investigated extensively; however, the modification of iron sulfide surfaces with prebiotically relevant chemical species and the effect of these species on prebiotically relevant reaction chemistry has not been characterized. Therefore, experiments were conducted to determine if modification of the pyrite surface with tetrathiomolybdate would result in enhanced rates of ammonia formation from nitrite and nitrate. It must be noted there is

significant concentrations of ammonia observed that originate in natural pyrite in this study and in previous studies [1]. A series of blank experiments were conducted in which DI water, nitrite solution, nitrate solution and pH 2 acid washing solution were added to the reactors and run as separate blank experiments to rule out any ammonia contamination in these solutions, or resulting from these solutions' interactions with the reactor walls. Based on the results of these experiments, it was determined that natural pyrite inherently contains μmole / kg levels of ammonia within it. The origin of this ammonia is not fully understood at this point, however.

An example of the enhancement of nitrite and nitrate (respectively) reduction kinetics can observed in Figures 6.1 and 6.3 which demonstrates a trend that the Mo-S-pyrite enhances yields of ammonia at 70 ^{o}C and 120 ^{o}C. Analysis of ammonia resulting from the reactions of pyrite / nitrite and pyrite / nitrate at 25 ^{o}C was not available, thus no comparison to Mo-S-pyrite can be made at this point. A closer analysis of the ammonia data reveals that nitrite reduction in the presence of Mo-S-pyrite leads to increased ammonia yields relative to pyrite without surface Mo present. Linear fits of the ammonia produced between 0 and 19 h of reaction, 19 h and data points that include surface Mo, and data points that do not include surface Mo through the end of the experimental run of pyrite / nitrite and Mo-S-pyrite / nitrite reactions at 25 ^{o}C, 70 ^{o}C and 120 ^{o}C is summarized in Table 6.1.

XRF data indicates that Mo is observed on all nitrite exposed Mo-S-pyrite surfaces throughout the experimental runs, except in the case of the 70 ^{o}C run in the last data points taken at 49.5 and 66 h. The rate of ammonia formation within this time frame is 1.7 x 10^{-7} mols. L^{-1}. h^{-1} which agrees well with the rate of ammonia formation on the

pyrite surface over the 19 h through end of the reaction time period (1.3×10^{-7} mols. L^{-1}. h^{-1}). Thus the Mo-S-pyrite surface which no longer has detectable levels of Mo on the surface, generates ammonia at a similar rate to that of the pyrite surface. The effect of the surface Mo on ammonia formation rates from nitrite / pyrite over the 19 h through end of reaction time period (1.3×10^{-7} mols. L^{-1}. h^{-1}), are compared to that of the 19 h through the time in which Mo is observed on the surface (4.3×10^{-7} mols. L^{-1}. h^{-1}), which results in a factor of 3.3 higher rate of ammonia formation in the Mo-S-pyrite case. Comparison of the ammonia formation rates between 0 and 19 h in the same experiments results in a factor of 2.2 times greater ammonia formation in the Mo-S-pyrite case. These results clearly indicate that the presence of Mo on the surface leads to increased rates of ammonia formation.

At 120 ^{o}C, Mo-S-pyrite and pyrite generate ammonia between 0 and 19 h of reaction at rates of 4.9×10^{-6} mols. L^{-1}. h^{-1} and 8.6×10^{-6} mols. L^{-1}. h^{-1}, respectively. Between 19 h and the end of each reaction, these rates become very nearly equivalent. This effect can be explained by both the lack nitrite observed during this period and that the blank experiments show similar rates of ammonia being leached from the surfaces. Experiments conducted with pyrite at 25 ^{o}C were not available for comparison.

In situ ATR-FTIR experiments were conducted to further explore the mechanism of nitrite reduction. Surface intermediates associated with nitrite reduction on Mo-S-pyrite at 70 ^{o}C will first be characterized and then compared to the same reaction at 25 ^{o}C and 120 ^{o}C. Scans taken 5 minutes after starting the reaction shows $\nu_s(NO)_2$ and $\nu_{as}(NO)_2$ dinitrosyl modes, observed at 1790 and 1750 cm^{-1}, which are the direct result of the

Table 6.1: Rates of ammonia formation from reactions of nitrite with Mo-S-pyrite and pyrite at 25 ^{o}C, 70 ^{o}C and 120 ^{o}C. Note that these rates are separated into rates observed between 0-19 h and those between 19 h and end of the reaction.

Temperature (^{o}C)	Reaction	Rate (mols L^{-1} h^{-1})		
		0 - 19 h	19 h - 0 surface Mo	0 surface Mo - end of reaction
25	nitrite/pyrite	-	-	-
25	DI/pyrite	-	-	-
25	nitrite/Mo-S-pyrite	1.5×10^{-6}	-1.5×10^{-8}	-
25	DI/ Mo-S-pyrite	5.7×10^{-7}	-1.8×10^{-9}	-
70	nitrite/pyrite	1.4×10^{-6}	1.3×10^{-7}	-
70	DI/pyrite	1.1×10^{-6}	1.1×10^{-7}	-
70	nitrite/Mo-S-pyrite	3.1×10^{-6}	4.3×10^{-7}	1.7×10^{-7}
70	DI/ Mo-S-pyrite	1.4×10^{-6}	2.2×10^{-7}	-
120	nitrite/pyrite	4.9×10^{-6}	1.3×10^{-6}	-
120	DI/pyrite	3.4×10^{-7}	8.6×10^{-7}	-
120	nitrite/Mo-S-pyrite	8.6×10^{-6}	1.1×10^{-6}	-
120	DI/ Mo-S-pyrite	5.0×10^{-6}	1.3×10^{-6}	-

Table 6.2: Summary of NO vibrational modes observed in this work compared to those from prior literature.

Site	υ{NO)	$\upsilon_s(NO)_2$	$\upsilon_{as}(NO)_2$	Surface	Reference
Mo^{4+}	-	1855	1756	MoS_2	[18]
Mo^{4+}	-	1858	1755	MoS_2	[18]
Mo^{4+}	-	1806	1702	M_xO_y / SBA-15	[19]
Mo^{4+}	-	1820	1710	MoO_3 / γ-Al_2O_3	[20]
Mo^{4+}	-	1810	1710	Mo / Al_2O_3	[21]
Mo^{4+}	-	1820	1710	MoO_3 / Al_2O_3	[23]
Mo^{4+}	-	1780	1680	Sulfided MoO_3 / Al_2O_3	[23]
Fe^{2+}	1742	-	-	FeS_2	[1]
Fe^{2+}	-	1795	1775	FeS_2	[1]
Fe^{2+}	-	1742	1702	FeS_2	[1]
Mo^{4+}	-	1790	1750	Mo-S-pyrite	This work
Fe^{2+}	1750	1770	1740	Mo-S-pyrite	This work

reduction of nitrite. Based on prior investigations on nitrite reduction on pyrite, the dominant binding mode observed of NO on pyrite was mononitrosyl, which showed an increase in intensity over the course of the three hour experiment [1]. Both the binding and intensity changes observed in this prior work are distinctly different from the increase of mode intensity attributed to the dinitrosyl bonding configuration which is observed over the first 5 minutes of the reaction on the modified pyrite surface. After 10 minutes into the reaction, these dinitrosyl modes show a sharp decrease in intensity that is most apparent an hour into the reaction. There is little change in the mode intensities between the first and third hours of reaction, indicating that the role of the surface is most important in the beginning of the reaction. It is not readily apparent whether the dinitrosyl modes associated with the Mo-S-pyrite surface are bound to Mo or Fe. We, however, favor a binding configuration that has, at least in part, NO bound to Mo based on a comparison of our vibrational modes to those obtained for dinitrosyl groups associated with Mo that have been observed in prior investigations [18-22]. NO vibrational modes on Mo and on Fe^{2+} are compared in Table 6.2. Though the cited investigations are mostly gas phase adsorption type infrared measurements, they all show that dinitrosyl modes are observed ubiquitously on Mo sites.

Nitrite reduction on Mo-S-pyrite at 25 ^{o}C results in a steady increase in mode intensity centered at ~1750 cm^{-1}. It is, however, difficult to make definitive assignments due to the number of possible binding configurations of NO on Mo and the lack of spectral resolution of these modes that are likely contained within this broadened region. Nevertheless, NO bound to Fe^{2+} is likely to be the mode responsible for intensity centered at ~1750 cm^{-1} based on DFT calculations and ATR-FTIR assignments from

investigations of nitrite and nitrate reduction on pyrite [1]. We speculate that mononitrosyl groups on Mo sites may be responsible for much of the broadening and overlap of this region, although we do not have definitive evidence in support of this statement. At a reaction temperature of 120 ^{o}C, low intensity NO modes are observed, with a maximum observed at 1750 cm^{-1} and these modes are attributed to NO bound to an Fe^{2+} surface site. Two modes positioned at 1835 and 1715 cm^{-1}, are tentatively attributed to dinitrosyl groups on oxidized Mo, possibly Mo^{5+}, which are assigned based on prior investigations [24]. Similar to prior work, little surface coverage of NO is observed at 120 ^{o}C [1]. Similarly, there is little NO observed in the reaction of nitrate and Mo-S-pyrite at 70 ^{o}C or 120 ^{o}C. [1]. Two possible explanation for this observation is that the NO sites are turned over quickly or since NO is relatively insoluble in aqueous solution that there is a kinetic effect which results in a buildup of NO in the gas phase. We suspect that the latter explanation is the least likely of the two since the 70 ^{o}C experiment results in copious amounts of NO observed on the surface, whereas, the 120 ^{o}C experiments shows little NO. ATR-FTIR results of nitrite reduction at 70 ^{o}C show a dramatic increase followed by an equally dramatic decrease of dinitrosyl modes observed over the 3 h run. This same behavior was not observed at 120 ^{o}C, however, we suspect that at 120 ^{o}C, the lesser amount of NO observed in the ATR-FTIR is due to a higher turnover rate due to the increased temperature.

Additional characterization of the Mo-S-pyrite surface after exposure to nitrite and nitrate by XPS was carried out in order to understand what role chemical speciation may play in the Mo desorption mechanism at reaction temperatures of 25 ^{o}C and 70 ^{o}C. At both temperatures, much of the peak intensity attributed to Mo is lost from the surface

prior to the first XPS data point. In the 25 ^{o}C case, XPS data suggests oxides of Mo (~233 eV) can be observed throughout the reaction, however, at 70 ^{o}C, little Mo related intensity can be detected after 16 h. We speculate that this feature is an oxidized Mo product which was either the result of oxidation in solution followed by reprecipitation onto the pyrite surface, a surface based oxidation event or a combination of both processes.

Molybdenum is known to be mobile within aerobic environments and immobilized in anaerobic and sulfidic environments [12, 14, 25]. Although the chemistry associated with Mo-sulfides and O_2 is very well characterized, the chemistry associated with surface based prebiotically relevant reactions, such as nitrite and nitrate reduction, on the Mo-S-pyrite surface is largely unknown.

Experiments were conducted in which Mo-S-pyrite was exposed to 5 mM nitrite (Figure 6.11, top) and nitrate (Figure 6.11, bottom) at 25 ^{o}C. As a control, Mo-S-pyrite was also exposed to O_2 free DI water (Figure 6.10, top). The results indicate that nitrate and deoxygenated water experiments result in little change in the surface content of Mo spectra after > 60 h of exposure at room temperature. Exposure to nitrite, however, resulted in a dramatic decrease in the amount of surface Mo as evidenced by the decrease in the Mo 3d spectral intensity after reaction. Based on the intensity of the Mo $3d_{3/2}$ peaks, there is roughly 65% of the Mo retained on the Mo-S-pyrite surface after exposure to DI water at room temperature, similar to that observed in the nitrate case (80%). However, the nitrite exposure results in less than 15 % of the intensity of the $Mo3d_{3/2}$ retained by then end of the reaction. This data is interpreted in view of prior investigations of similar experiments which determined that molybdate and

tetrathiomolybdate are bound reversibly and irreversibly, respectively, on pyrite [12] and that Mo only partitions into solution as an oxidized species. Thus, it is inferred that Mo desorption from the pyrite surface is preceded by an oxidation event [12, 25]. Furthermore, it can be said with certainty that nitrogen oxides may have played a key role in mobilizing Mo [26, 3]. Specifically, nitrite reduction of Mo-S-pyrite would help to mobilize Mo through oxidation. Interestingly, there is a much lesser effect from nitrate reduction (to ammonia) on Mo mobilization which is likely due to higher activation barrier that nitrate reduction exhibits [1, 9].

6.8.3 RESULTS IN VIEW OF PRIOR WORK

Prior investigation of nitrite and nitrate reduction on iron-sulfur mineral surfaces has focused on the effect of temperature on the reaction, and in some cases, the relevant mechanistic details as well [1, 7-9]. Similarly, it has been suggested that molybdenum-sulfur compounds may have played a key role in enzyme active site evolution within the early earth [3]. Though much of the information regarding the role of Mo was elucidated from prior literature in oxic and anoxic environments [12, 14, 25], there is has been little work accomplished in the prebiotic context, specifically within reactions with nitrogen oxides which have been proposed as key source of fixed nitrogen [26].

Investigation into nitrite and nitrate reduction in the presence of iron sulfides was first conducted by Summers in 2005 [8]. However, there still exists a significant gap of understanding between modern day enzyme active site structure and composition of iron sulfur mineral structure. Specifically little progress has been made on modifying the mineral surface to more closely resemble structural motifs observed in enzymes. The approach taken in this chapter attempts to close this gap by modifying the iron sulfide

(pyrite) surface with tetrathiomolybdate and testing the effects of the resulting mineral, Mo-S-pyrite, on nitrite and nitrate reduction reactions. Based on our results it is clear that the presence of ~ppm amounts of Mo on the pyrite surface in fact enhances ammonia formation amounts by a fact of ~1.8 at 70 ^{o}C and 120 ^{o}C. Furthermore, the reduction of nitrate, a reaction which Summers stated was "irreproducible" and was found in more recent work to be kinetically hindered [1, 8, 9], in fact resulted in significant consistent ammonia formation in the presence of Mo-S-pyrite. Thus the results presented here suggests that ~ppm amounts of Mo on the pyrite surface may have significantly increased concentrations of ammonia on early Earth resulting from nitrate and nitrite reduction on iron sulfur surfaces, since the presence of Mo increased yields from not only nitrite, but also from nitrate. Thus, the 70 μmolar levels of ammonia that Summers postulated to have existed in the Hadean Oceans may be a somewhat conservative estimate, given that contributions to ammonia formation resulting from dopants such as tetrathiomolybdate increase ammonia formation rates on pyrite by as much as a factor of ~1.8 [7].

It must be mentioned that we cannot exclude that Mo^{4+} solution phase species may reduce nitrite (or nitrate), independent of the presence of pyrite. More investigation is required to understand the role of Mo solution phase species on nitrite and nitrate reduction.

6.9 CONCLUSIONS

This investigation represents a key step in the transfer of mineral based prebiotic molecular systems to more biologically relevant structures capable of increasing rates of reactions that are of prebiotic importance by means other than temperature. The addition

of the Mo to the pyrite surface results in an increase in ammonia formation over pyrite alone.

References

[1] Singireddy, S., Gordon, A.D., Smirnov, A., Vance, M.A., Szilagyi, R.K., Schoonen, M.A., Strongin, D.R., *Astrobiology*, (Submitted).

[2] Bertini, I., Gray, H.B., Stiefel, E.I., Selverstone-Valentine, J., *Biological Inorganic Chemistry: Structure and Reactivity*, University Science Books, Sausalito, California, 2007.

[3] Nitschke, W., Russell, M., *Journal of Molecular Evolution*, 69 (2009) 481-496.

[4] Summers, D.P., *Origins of Life and Evolution of the Biosphere*, 29 (1999) 33-46.

[5] Walker, J.C.G., Brimblecombe, P., *Precambrian Research*, 28 (1985) 205-222.

[6] Zohner, A., Broda, E., *Origins of Life and Evolution of the Biosphere*, 9 (1979) 291-298.

[7] Summers, D.P., Chang, S., *Nature*, 365 (1993) 630-632.

[8] Summers, D.P., *Origins of Life and Evolution of the Biosphere*, 35 (2005) 299-312.

[9] Gordon, A.D., Smirnov, A., Shumlas, S., Singireddy, S., DeCesare, M., Schoonen, M.A.A., Strongin, D.R., Manuscript in Preparation, (2011).

[10] Smirnov, A., Hausner, D., Laffers, R., Strongin, D., Schoonen, M., *Geochemical Transactions*, 9 (2008) 5.

[11] Brandes, J.A., Boctor, N.Z., Cody, G.D., Cooper, B.A., Hazen, R.M., Yoder, H.S., Jr., *Nature*, 395 (1998) 365-367.

[12] Bostick, B.C., Fendorf, S., Helz, G.R., *Environmental Science and Technology*, 37 (2003) 285-291.

[13] Amornthammarong, N., Zhang, J.-Z., *Analytical Chemistry*, 80 (2008) 1019-1026.

[14] Helz, G.R., Miller, C.V., Charnock, J.M., Mosselmans, J.F.W., Patrick, R.A.D., Garner, C.D., Vaughan, D.J., *Geochimica et Cosmochimica Acta*, 60 (1996) 3631-3642.

[15] Arutyunyan, L.A., *Geochemistry International*, (1966) 479-485.

[16] Galtayries, A., Wisniewski, S., Grimblot, J., *Journal of Electron Spectroscopy and Related Phenomena*, 87 (1997) 31-44.

[17] Moulder, J.F., Stickle, W.F., Sobol, P.E., *Handbook of X Ray Photoelectron Spectroscopy*, Perkin Elmer, Eden Prairie, Mn, 1992.

[18] Maugé, F., Lamotte, J., Nesterenko, N.S., Manoilova, O., Tsyganenko, A.A., *Catalysis Today*, 70 (2001) 271-284.

[19] Thielemann, J., Kröhnert, J., Hess, C., *Journal of Physical Chemistry C*, 114 (2010) 17092-17098.

[20] Millman, W.S., Hall, W.K., *Journal of Physical Chemistry C* 83,3, (1979) 427-428.

[21] Peri, J.B., *Journal of Physical Chemistry*, 86 (1982) 1615-1622.

[22] Fu, Y., Zhao, F., *Catalysis Lette*rs, 12 (1992) 117-125.

[23] Okamoto, Y., Oh-Hiraki, K., Imanaka, T., Teranishi, S., *Journal of Catalysis*, 71 (1981) 99-110.

[24] Iizuka, T., Itoh, M., Hattori, H., Tanabe, K., *Journal of the Chemical Society, Faraday Transactions 1: Physical Chemistry in Condensed Phases*, 78 (1982) 501-508.

[25] Erickson, B.E., Helz, G.R., *Geochimica et Cosmochimica Acta*, 64 (2000) 1149-1158.

[26] Ducluzeau, A.-L., van Lis, R., Duval, S., Schoepp-Cothenet, B., Russell, M.J., Nitschke, W., *Trends in Biochemical Sciences*, 34 (2009) 9-15.

CHAPTER 7

SUMMARY

Chemical reactions on promoted copper-silicon surfaces, iron sulfide surfaces and modified pyrite surfaces have been investigated using in situ ATR-FTIR spectroscopy in conjunction with other characterization techniques. More specifically, results of investigations pertaining to the effects of single and multiple promotion on the Direct Synthesis of methylchlorosilanes as well as mechanistic details of nitrite and nitrate reduction on iron-sulfur based surfaces have been presented. Using in situ attenuated total reflection-Fourier transform infrared spectroscopy as well as other various ex situ analytical methodologies and mechanistic details associated with reactions that occur on the various surfaces have been elucidated. These mechanistic details have proven elusive in prior surface based investigations due to the inhospitable conditions in which the reactions take place.

7.1 EFFECTS OF INDIVIDUAL PROMOTERS ON THE DIRECT SYNTHESIS OF METHYLCHLOROSILANES

Results of the investigation of single promotion of copper-silicon surfaces for the purposes of methylchlorosilane production have been presented. The results indicate promotion of these surfaces with tin and phosphorus led to a greater methyl fraction sustained on the surface of the working catalytic surface. Despite the increase of methyl groups these promoters induced, tin seemed to promote the production of dichlorodimethylsilane nearly exclusively, while phosphorus induced cleavage of the C-H bond leading to production of the undesirable silane, dichloromethylsilane. Promotion with zinc led to an increase in selectivity of dichlorodimethylsilane relative to the

unpromoted copper-silicon surface. MeCl and silicon conversions of the promoter surface decreased in the order tin > phosphorus > zinc > unpromoted.

7.2 EFFECTS OF MULTIPLE PROMOTION OF THE DIRECT SYNTHESIS CONTACT MASS WITH P, Zn, AND Sn ON THE SYNTHESIS OF METHYLCHLOROSILANES

An investigation of the synergistic effects associated with the combinations of tin, zinc and phosphorus promoters were also investigated. The main result that can be ascertained from this investigation is that the case of the triple promoted contact mass results in an enrichment of Cu at the surface and promoted a binding site of methyl to copper as indicated by in situ ATR-FTIR experiments. The triple promoted contact mass also shows the greatest MeCl and Si conversions out of any of combination of tin, phosphorus and zinc. Over the course of the reaction, the triple promoted starts at among the highest dichlorodimethylsilane selectivities and by the end of the run is among the lowest. Among the notable synergistic effects observed is the dichlorodimethylsilane selectivity observed most significantly in the zinc / tin and zinc / phosphorus promoted contact masses.

7.3 NITRITE AND NITRATE REDUCTION ON NANO-FeS SURFACES

The goal of this work is to investigate the possibility that enzyme evolution may have begun on the early earth, specifically on FeS based surfaces. Specifically the reduction of nitrite and nitrate were investigated on these surfaces as a function of temperature. It was found that the reduction of nitrate was severely hindered kinetically and only proceeded at 120 ^{o}C. Nitrite reduction, on the other hand, proceeded rather quickly at 70 ^{o}C and even more rapidly at 120 ^{o}C. Results from ATR-FTIR experiments

indicate that a surface bound NO intermediate is observed during the reduction, which seems to be indicator of ammonia formation.

7.4 NITRITE AND NITRATE REDUCTION ON Mo-S-PYRITE

In order to bridge the gap between the mineral based geochemical and biochemical world, experiments were conducted in which a biologically relevant Mo based cubane was added to the pyrite surface. Nitrite and nitrate reduction experiments were conducted at room temperature, 70 ^{o}C and 120 ^{o}C and subsequent analysis of ammonia, nitrite and nitrate were also made. Additional analyses of the Mo-S-pyrite surface were also conducted using ex situ XRF and XPS solid state analyses. Based on ammonia yields, tetrathiomolybdate treatment of pyrite resulted in increase in ammonia formation over pyrite alone. In situ ATR-FTIR results indicate an NO intermediate is observed during this reaction, as is the case with pyrite. The NO binding occurs as a dinitrosyl group which is much different than the case of pyrite which is mononitrosyl. XRF and XPS results indicate that while some of the Mo does not remain in the surface as the reaction proceeds at 70 ^{o}C and 120 ^{o}C, significant amounts of Mo still remains on the surface

REFERENCES CITED

Agarwala, J. P. and Falconer, J. L., *International Journal of Chemical Kinetics*, 19 (1987) 519-37.

Amores, J. G., Escribano, V. S., Ramis, G. and Busca, G., *Applied Catalysis B: Environmental*, 13 (1997) 45-58.

Amornthammarong, N. and Zhang, J. Z., *Analytical Chemistry*, 80 (2008) 1019-1026.

Arutyunyan, L. A., *Geochemistry International*, (1966) 479-485.

Blöchl, E., Keller, M., Wächtershäuser, G. and Stetter, K. O., *Proceedings of the National Academy of Sciences* USA, 89 (1992) 8117-8120.

Bostick, B. C., Fendorf, S. and Helz, G. R., *Environmental Science and Technology*, 37 (2003) 285-291.

Brandes, J. A., Boctor, N. Z., Cody, G. D., Cooper, B. A., Hazen, R. M. and Yoder, H. S., Jr., *Nature*, 395 (1998) 365-367.

Braterman, P. S., *Metal Carbonyl Spectra*, Academic Press, London, 1975.

Chupas, P. J., Qui, X., Hanson, J. C., Lee, P. L., Grey, C. P. and Billinge, S. J. L., *Journal of Applied Crystallography*, 36 (2003) 1342-1347.

Cohen, J. B., *Ultramicroscopy*, 34 (1990) 41-46.

Colaianni, M. L., Chen, P. J., Gutleben, H. and Yates, J. T., Jr., *Chemical Physics Letters*, 191 (1992) 561-8.

Corn, S. H., Falconer, J. L. and Czanderna, A. W., *Journal of Vacuum Science & Technology, A: Vacuum, Surfaces, and Films*, 6 (1988) 1012-16.

Cottrell, T. L., *The Strengths of Chemical Bonds*, Butterworths, London, 1958.

Ducluzeau, A.-L., van Lis, R., Duval, S., Schoepp-Cothenet, B., Russell, M. J. and Nitschke, W., *Trends in Biochemical Sciences*, 34 (2009) 9-15.

Ehrich, H., Born, D., Richter-Mendau, J. and Lieske, H., *Applied Organometallic Chemistry*, 12 (1998) 257-264.

Ehrich, H., Born, D., Richter, K., Richter-Mendau, J. and Lieske, H., *Applied Organometallic Chemistry*, 11 (1997) 237-247.

Erickson, B. E. and Helz, G. R., *Geochimica et Cosmochimica Acta*, 64 (2000) 1149-1158.

Farrow, C. L., Juhas, P., Liu, J.W., Bryndin, D., Bŏzin, E.S., Bloch, J., Proffen, T.H., and Billinge, S.J.L., *Journal of Physics: Condensed Matter*, 19 (2007) 335219.

Févotte, G., *International Journal of Pharmaceutics*, 241 (2002) 263-278.

Floquet, N., Yilmaz, S. and Falconer, J. L., *Journal of Catalysis*, 148 (1994) 348-68.

Frank, T. C., Kester, K. B. and Falconer, J. L., *Journal of Catalysis*, 95 (1985) 396-405.

Fu, Y. and Zhao, F., *Catalysis Letters*, 12 (1992) 117-125.

Galtayries, A., Wisniewski, S. and Grimblot, J., *Journal of Electron Spectroscopy and Related Phenomena*, 87 (1997) 31-44.

Gasper-Galvin, L. D., Rethwisch, D. G., Sevenich, D. M. and Friedrich, H. B., *Studies in Organic Chemistry* (Amsterdam), 49 (1993) 279-97.

Gasper-Galvin, L. D., Sevenich, D. M., Friedrich, H. B. and Rethwisch, D. G., *Journal of Catalysis*, 128 (1991) 468-78.

Gheyas, S. I., Strable, B. L., Strongin, D. R. and Wright, A. P., *Surface Science*, 474 (2001) 129-138.

Giggenbach, W. F., *Geochimica Cosmochimica Acta*, 44 (1980) 2021-2032.

Giggenbach, W. F., The origin and evolution of fluids in magmatic-hydrothermal systems, in: H. L. Barnes (Ed.) *Geochemistry of Hydrothermal Ore Deposits*, John Wiley & Sons, Inc., New York, 1997, pp. 737-795.

Glass, J. A., Jr., Wovchko, E. A. and Yates, J. T., Jr., *Surface Science*, 338 (1995) 125-37.

Goldstein, J., Newbury, D., Joy, D., Lyman, C., Echlin, P., Lifshin, E., Sawyer, L. and Michael, J., *Scanning Electron Microscopy and X-Ray Microanalysis, Third ed.*, Plenum Publishers, New York, 2003.

Gordon, A., Hinch, B. and Strongin, D., *Catalysis Letters*, 133 (2009) 14-22.

Gordon, A. D., Hinch, B. J. and Strongin, D. R., *Journal of Catalysis*, 266 (2009) 291-298.

Gordon, A. D., Smirnov, A., Shumlas, S., Singireddy, S., DeCesare, M., Schoonen, M. A. A. and Strongin, D. R., Manuscript in Preparation, (2011).

Gregor, C. B., Garrels, R. M., McKenzie, F. T. and Maynard, J. B., *Chemical Cycles in the Evolution of the Earth*, Wiley, New York, 1988.

Grotzinger, J. P. and Kasting, J. F., *Catalysis Letters*, 101 (1993) 235-243.

Guinier, A., X-*ray Diffraction in Crystals, Imperfect Crystals, and Amorphous Bodies*, Dover, New York, 1994.

Hadjiivanov, K. I., *Catalysis Reviews*, 42 (2000) 71-144.

Hall, B. D., Zanchet, D. and Ugarte, D., *Journal of Applied Crystallography*, 33 (2000) 1335-1341.

Halm, R. L., Zapp, R. H. and Streu, R. D., *Reduced formation of methyltrichlorosilane in the Rochow process in the presence of hydrogen*, in, (Dow Corning Corp., USA). Application: US, 1990, pp. 7

Hammersley, A. P., Svenson, S. O., Hanfland, M. and Hauserman, D., *High Pressure Research*, 14 (1996) 235-248.

Han, J., Gheyas, S. I., Strongin, D. R., Hinch, B. J. and Wright, A. P., *Catalysis Letters*, 68 (2000) 147-152.

Han, J., Gheyas, S. I., Wang, Y., Strongin, D. R., Graham, A. P., Hinch, B. J. and Wright, A. P., *Journal of Physical Chemistry B*, 104 (2000) 3078-3084.

Han, J., Gheyas, S. I., Wang, Y., Strongin, D. R., Hinch, B. J. and Wright, A. P., *Langmuir*, 16 (2000) 6541-6545.

Harrick, N. J., *Internal Reflection Spectroscopy, 2nd ed*., John Wiley and Sons, New York, 1979.

Harris, D. C., *Quantitative Chemical Analysis, 6th ed.*, W.H. Freeman and Company, New York, 1982.

Helz, G. R., Miller, C. V., Charnock, J. M., Mosselmans, J. F. W., Pattrick, R. A. D., Garner, C. D. and Vaughan, D. J., *Geochimica et Cosmochimica Acta*, 60 (1996) 3631-3642.

Howard, J. B. and Rees, D. C., *Chemical Reviews*, 96 (1996) 2965-2982.

Ingo, A., Steinhoff, B., Lellinger, D., *Measurement Science and Technology*, 21 (2010) 062001.

Kasting, J. F., *Precambrian Research*, 34 (1987) 205-229.

Kim, J. P. and Rethwisch, D. G., *Journal of Catalysis*, 134 (1992) 168-78.

Kip, B. J., Berghmans, T., Palmen, P., van der Pol, A., Huys, M., Hartwig, H., Scheepers, M. and Wienke, D., *Vibrational Spectroscopy*, 24 (2000) 75-92.

Koguma, K., Ikeda, M., Ota, N., Matsuda, K. and Kaneta, M., *Journal of Vacuum Science & Technology A: Vacuum, Surfaces, and Films*, 25 (2007) 324-329.

Kolasinski, K., Surface Science, John Wiley and Sons, Ltd., Chicester, 2008.

Kong, M. J., Lee, S. S., Lyubovitsky, J. and Bent, S. F., *Chemical Physics Letters* 263 (1996) 1-7.

Lennie, A. R., Redfern, S. A. T., Schofield, P. F. and Vaughan, D. J., Synthesis and Rietveld crystal structure refinement of mackinawite, tetragonal FeS, in: *Mineralogical Magazine*, 1995, pp. 677 (8 pages).

Leventis, H. C., King, S. P., Sudlow, A., Hill, M. S., Molloy, K. C. and Haque, S. A., *Nano Letters*, 10 1253-1258.

Levin, L., Atzmon, Z., Katsman, A. and Werber, T., *Materials Chemistry and Physics*, 40 (1995) 56-61.

Lewis, K. M. and Kanner, B., *Catalyzed Direct Reactions of Silicon*, El Sevier, Amsterdam, 1993.

Lewis, L. N., *Chemistry of Organic Silicon Compounds, 2* (1998) 1581-1597.

Lewis, L. N. and Ward, W. J., *Industrial & Engineering Chemistry Research*, 41 (2002) 397-402.

Lieske, H., Fichtner, H., Grohmann, I., Selenina, M., Walkow, W., Zimmermann, R., Characterization of Rochow Contact Masses by Catalytic Results, XRD, Chemisorption and XPS, in: *Silicon for the Chemical Industry, [Int. Conf.]*, 1992

Lieske, H., Kretzschmar, U. and Zimmermann, R., Action of promoters in Rochow contact masses, in: *Silicon for the Chemical Industry, [Int. Conf.]*, 1994

Luo, W., Wang, G. and Wang, J., *Chemical Engineering Communications*, 193 (2006) 754-763.

Macleod, G., McKeown, C., Hall, A. J. and Russell, M. J., *Origins of Life and Evolution of the Biosphere*, 24 (1994) 19-41.

Mancinelli, R. L. and McKay, C. P., *Origins of Life and Evolution of the Biosphere*, 18 (1988) 311-325.

Mattioli, G. S. and Wood, B. J., *Nature*, 322 (1986) 626-628.

Maugé, F., Lamotte, J., Nesterenko, N. S., Manoilova, O. and Tsyganenko, A. A., *Catalysis Today*, 70 (2001) 271-284.

Michalak, D. J., Amy, S. R., Esteve, A. and Chabal, Y. J., *Journal of Physical Chemistry C*, 112 (2008) 11907-11919.

Michel, F.M., Antao, S.M., Chupas, P.J., Lee, P.L., Parise, J.B., Schoonen, M.A.A., *Chemistry of Materials*, accepted (2005).

Miller, S. L., *Science*, 117 (1953) 528-529.

Millman, W.S., Hall, W.K., *Journal of Physical Chemistry C* 83,3, (1979) 427-428.

Moulder, J. F., Stickle, W. F. and Sobol, P. E., *Handbook of X-Ray Photoelectron Spectroscopy*, Perkin Elmer, Eden Prairie, Mn, 1992.

Nitschke, W. and Russell, M., *Journal of Molecular Evolution*, 69 (2009) 481-496.

Ohfuji, H. and Rickard, D., *Earth and Planetary Science Letters*, 241 (2006) 227-233.

Okamoto, Y., Maezawa, A. and Imanaka, T., *Journal of Catalysis*, 120 (1989) 29-45.

Okamoto, Y., Oh-Hiraki, K., Imanaka, T. and Teranishi, S., *Journal of Catalysis*, 71 (1981) 99-110.

Peri, J. B., *Journal of Physical Chemistry*, 86 (1982) 1615-1622.

Potochnik, S. J. and Falconer, J. L., *Journal of Catalysis*, 147 (1994) 101-6.

Qiu, X., Thompson, J. W. and Billenge, S. J. L., *Journal of Applied Crystallography*, 37 (2004) 678.

Ramis, G., Yi, L. and Busca, G., *Catalysis Today*, 28 (1996) 373-380.

Rethwisch, D. G., Olakangil, J. F., Wood, L. H., Miller, D. C. and Wineland, J. D., *Silicon for the Chemical Industry VI, [Conference]*, Loen, Norway, (2002)

Rochow, E. G., *Journal of the American Chemical Society*, 67 (1945) 963-5.

Rouxel, O., Shanks, W. C., Bach, W. and Edwards, K. J., *Chemical Geology*, 252 (2008) 214-227.

Russell, M. J., Daniel, R. M. and Hall, A. J., *Terra Nova*, 5 (1993) 343-347.

Russell, M. J., Hall, A. J., Cairns-Smith, A. G. and Braterman, P. S., *Nature*, 336 (1988) 117.

Russell, M. J., Hall, A. J. and Martin, W., *Geobiology*, 8 355-371.

Russell, M. J., Hall, A. J. and Turner, D., *Terra Nova*, 1 (1989) 238-241.

Schoonen, M. A. A. and Xu, Y., *Astrobiology*, 1 (2001) 133-140.

Schopf, J. W. ed., *Earth's Earliest Biosphere*, Princeton University Press, 1983.

Seyferth, D., *Organometallics*, 20 (2001) 4978-4992.

Singireddy, S., Gordon, A. D., Smirnov, A., Vance, M. A., Szilagyi, R. K., Schoonen, M. A. and Strongin, D. R., *Astrobiology*, (Submitted).

Smirnov, A., Hausner, D., Laffers, R., Strongin, D. and Schoonen, M., *Geochemical Transactions*, 9 (2008) 5.

Smirnov, A., Schoonen, M. A. A., Tosca, N. J., Chidambaram, D., Halada, G. and Luptak, B., Abiotic formation and fate of ammonium in the Hadean Ocean, in: *NAI General Meeting*, Boulder, CO, 2005.

Stolt, L., Charai, A., D'Heurle, F. M., Fryer, P. M. and Harper, J. M. E., *Journal of Vacuum Science & Technology A: Vacuum, Surfaces, and Films*, 9 (1991) 1501-1505.

Stribling, R. and Miller, S. L., *Origins of Life and Evolution of the Biosphere*, 17 (1987) 261-273.

Summers, D.P., *Origins of Life and Evolution of the Biosphere*, 35 (2005) 299-312.

Summers, D. P., *Origins of Life and Evolution of the Biosphere*, 29 (1999) 33-46.

Summers, D. P. and Chang, S., *Nature*, 365 (1993) 630-632.

Thielemann, J., Kröhnert, J. and Hess, C., *Journal of Physical Chemistry C*, 114 (2010) 17092-17098.

Usher, C. R., Cleveland, C. A., Strongin, D. R. and Schoonen, M. A. A., *Environment Science & Technology*, 38 (2004) 5604-5606.

Usher, C. R., Paul, K. W., Narayansamy, J., Kubicki, J. D., Sparks, D. L., Schoonen, M. A. A. and Strongin, D. R., *Environmental Science & Technology*, 39 (2005) 7576-7584.

Voorhoeve, R. J. H., *Organohalosilanes: Precursors of Silicones*, 1967.

Voorhoeve, R. J. H., Lips, J. A. and Vlugter, J. C., *Journal of Catalysis*, 3 (1964) 414-425.

Wächtershäuser, G., *Systematic and Applied Microbiology*, 52 (1988) 452-484.

Wächtershäuser, G., *Systematic and Applied Microbiology*, 10 (1988) 207-210.

Wächtershäuser, G., *Origins of Life and Evolution of the Biosphere*, 20 (1990) 173-176.

Wächtershäuser, G., *Proceedings of the National Academy of Sciences* USA, 87 (1990) 200-204.

Wächtershäuser, G., *Progress in Biophysics and Molecular Biology*, 58 (1992) 85-201.

Walker, J. C. G. and Brimblecombe, P., *Precambrian Research*, 28 (1985) 205-222.

Ward, W. J., Ritzer, A., Carroll, K. M. and Flock, J. W., *Journal of Catalysis*, 100 (1986) 240-9.

Wessel, T. J. and Rethwisch, D. G., *Journal of Catalysis*, 161 (1996) 861-866.

Wolthers, M., Van der Gaast, S. J. and Rickard, D., *American Mineralogist*, 88 (2003) 2007-2015.

Zhai, R.-S., Chan, Y. L., Chuang, P., Hsu, C.-K., Mukherjee, M., Chuang, T. J. and Klauser, R., *Langmuir*, 20 (2004) 3623-3631.

Zhang, X. V., Strongin, D. R., Goncharova, L. V., Ermakov, A. V. and Hinch, B. J., *Journal of Physical Chemistry B*, 108 (2004) 16213-16219.

Zohner, A. and Broda, E., *Origins of Life and Evolution of the Biosphere*, 9 (1979) 291-298.

APPENDICES

APPENDIX A

DINITROGEN REDUCTION ON NANO-FeS_m

INTRODUCTION

It has been suggested that ammonia formation was a key step in the prebiotic synthesis of amino acids. However, the predominant form of nitrogen during this prebiotic time period on Earth was thought to be dinitrogen. Thus, the formation of ammonia through dinitrogen reduction has been investigated in prior batch reaction experiments specifically using conditions to mimic hydrothermal vent chemistry, which was the type of conditions thought to most likely to harbor early prebiotic chemistry[1].

This kinetics of dinitrogen reduction reaction has been investigated in detail by Schoonen et al, and the results of which suggest a surface based reaction on FeS nanoparticles [1]. Therefore, in order to confirm the conclusions Schoonen reached in his hypothesis, attenuated total reflection-Fourier transform infrared spectroscopy was utilized to observe surface intermediate associated with nitrogen reduction on the FeS surface.

EXPERIMENTAL METHODOLOGY

ATR METHODLOGY

In this investigation, an ATR-FTIR cell or composed of diamond set in a tungsten carbide puck (Specac) and a reactor "dome" that allows for gas pressurization was utilized to simulate the high pressure (50 bar) and high temperature (120 ^{o}C) conditions of the hydrothermal environment. The reactor dome was modified in two ways; a "spacer" was designed and added to the cell to increase the volume of the cell to ~150 μL and heating tape was used to heat the top of the cell to the same temperature as the

bottom to minimize any issues with sample migration (presumably through diffusion) over the course of the experiments.

This ATR accessory was mounted in the Nicolet Magna 750 FTIR spectrometer which is equipped with an LN_2 cooled MCTA detector. Single beam spectra were recorded as an average of 500 scans with a resolution of 4 cm^{-1}, each spectra taking of about 5 minutes. A background spectrum was recorded once the temperature stabilized at 120 ^{o}C. This background was to be used as our starting point in each respective experiment (time 0). This approach is taken since the kinetics of the N_2 reduction reaction are extremely slow.

SOLUTION PREPARATION

All experimental preparation was conducted in anoxia in an argon purged glove bag. All solutions were purged with argon for 1-2 hours to remove any dissolved oxygen. Freshly precipitated FeS was prepared in the argon filled glove bag using previously established methods [1].

10 mM sodium sulfide solutions were prepared using O_2 free DI water. The pH was adjusted to pH 6.5, (The pH will have a tendency to increase due to the formation of H_2S gas) Using a modified flask (capped) with septa ports to adjust pH will help prevent this pH increase from occurring.

CREATING THE SLURRY

A small amount of FeS material was added to the pH 6.5 Na_2S solution creating a slurry. The loadings for the 120 ^{o}C, 10 mM Na_2S pH 6.5 argon control experiments was 0.02 g FeS / ml and the dinitrogen experiment was .022 g FeS / mL.

LOADING THE SLURRY

All loading is done in the glove box in anoxia. The spacer is placed on the ATR puck, and ~150 μL slurry is added slowly, taking care to make sure the slurry is spread uniformly over the puck and that no bubbles are present. The dome is then carefully placed on top of the spacer, and fastened into place. Any spillage of the slurry necessitates a new sample. Making sure the valves are completely closed, the setup is taken from the glove box to the spectrometer and fastened into place. The N_2 / Ar line is evacuated and a small flow of N_2 / Ar is used to evacuate air exposed portions of the line as they are reattached. The pressure is then slowly adjusted to 725 psi (~50 bar).

RESULTS AND DISCUSSION

This appendix serves as a follow up study of work batch reactor studies performed by Schoonen and Xu, which investigates the synthesis of ammonia from dinitrogen at ~50 bar and 120 ^{o}C [1].

ATR spectra resulting from N_2 reduction experiment conducted at 120 ^{o}C and complimentary argon control experiments are demonstrated in Figure A.1 (top and bottom) between 1350 and 800 cm^{-1}. It is clear that the N_2 experiments show greater mode intensity at positions unique to the N_2 experiment that are not observed in the argon control experiment. These modes are thought to be related to ammonia formation, likely oxidized sulfur and / or hydrazine intermediates. Specifically, modes at 1259 cm^{-1} and 1202 cm^{-1} are attributed to the N=N stretch, and an NH scissoring mode of a hydrazine like species adsorbed on the FeS surface. A second set of possibilities is that one or more of these modes can be attributed to deformation modes of NH_3. We discount this possibility on the basis of control experiments with FeS and ammonium chloride which did not show modes in this region. Therefore, these assignments are similar to those made

for hydrazine-like intermediates observed on various other surfaces [2, 3]. In addition, the NH deformation of NH_3 may also be observed as a small shoulder at ~1215 cm^{-1}, although this mode is mostly covered by the NH rock of the hydrazine-like intermediate. It is important to note that other modes due to NH species would be observed as a broad band of modes between 1450 cm^{-1} and 1350 cm^{-1}, though the low concentration of these modes make assigning them problematic.

In addition to the ammonia modes observed in the FeS 120 ^{o}C experiment, there are observed due to various oxidized sulfide species centered at 1144, 1103, 1056, 1024, 880 and 839 cm^{-1} that are present in the 120 ^{o}C argon and 70 ^{o}C N_2 spectrum as well. Though these modes are observed and correspond to oxidized sulfur species, presumably through the splitting of water (i.e. Fenton chemistry), a theoretical approach similar to that of oxidation on pyrite (FeS_2) surfaces may shed light on the exact sources of these modes [4, 5]. Due to the extremely low intensity of the modes in this work, spectral defects such as the feature observed at 1306 cm^{-1} are observed. These defects are not thought to interfere with the trends presented in the data. The 70 ^{o}C FeS N_2 experiment, shown in Figure A.2, shows little growth of modes attributed to ammonia. Though common vibrational assignments can be observed with the experiments at 120 ^{o}C, these are likely residual oxidation possibly from slight O_2 contamination.

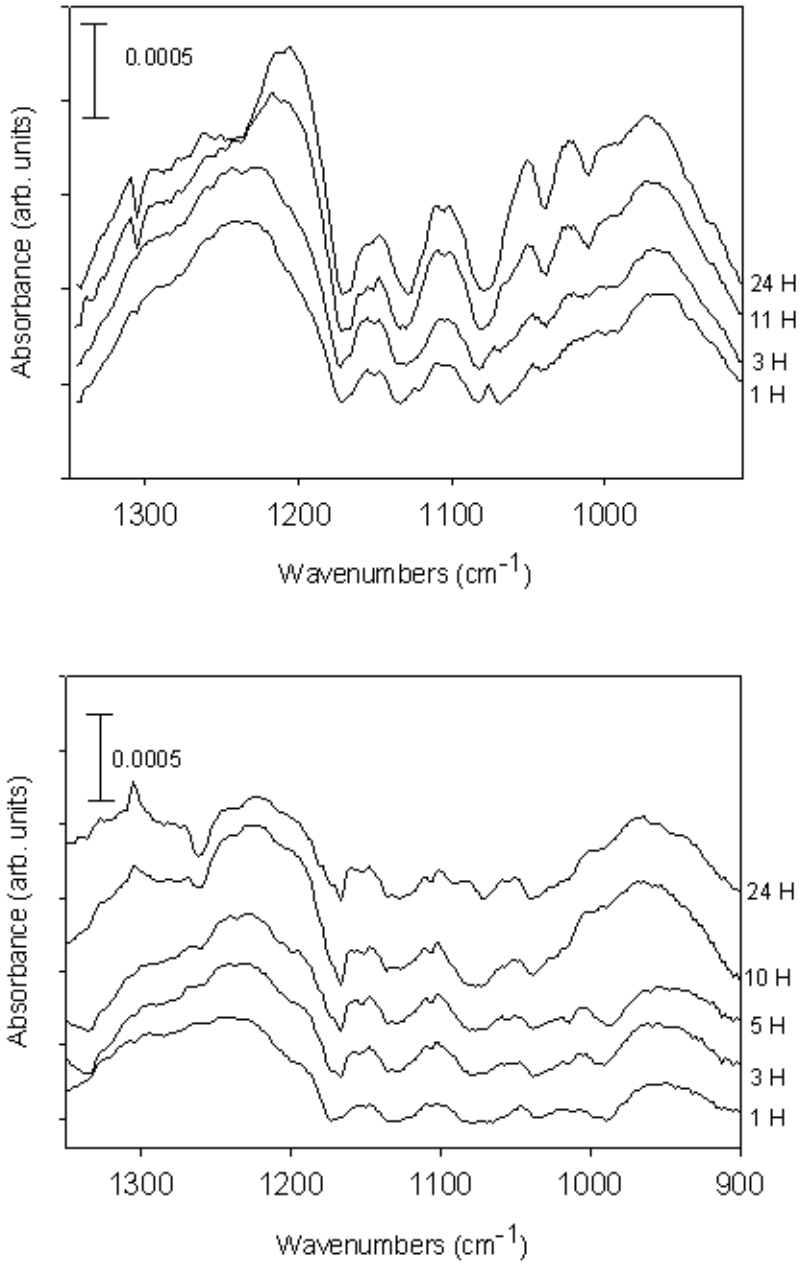

Figure A.1: ATR-FTIR spectra associated with N_2 / FeS / 120 ^{o}C (top) and argon / FeS / 120 ^{o}C (bottom) experiments as a function of time. Note that spectra are offset for clarity.

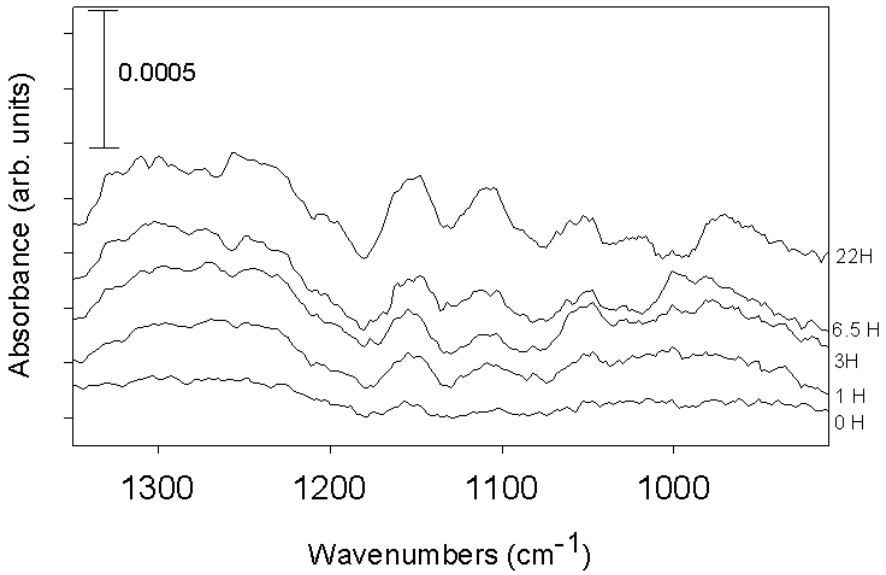

Figure A.2: ATR-FTIR spectra associated with the N_2 / FeS / 70 ^{o}C experiment as a function of time. Note that spectra are offset for clarity.

References

[1] Schoonen, M.A.A., Xu, Y., *Astrobiology*, 1 (2001) 133-140.

[2] Ramis, G., Yi, L., Busca, G., *Catalysis Today*, 28 (1996) 373-380.

[3] Amores, J.G., Escribano, V.S., Ramis, G., Busca, G., *Applied Catalysis B: Environmental*, 13 (1997) 45-58.

[4] Usher, C.R., Paul, K.W., Narayansamy, J., Kubicki, J.D., Sparks, D.L., Schoonen, M.A.A., Strongin, D.R., *Environmental Science & Technology*, 39 (2005) 7576-7584.

[5] Singireddy, S., Gordon, A.D., Smirnov, A., Vance, M.A., Szilagyi, R.K., Schoonen, M.A., Strongin, D.R., *Astrobiology*, (Submitted).